THESIS

CAVITY RING-DOWN SPECTROSCOPY AND THE RETRIEVAL OF AEROSOL OPTICAL PROPERTIES FROM BIOMASS BURNING DURING FLAME2

Submitted by
Laura E Mack
Department of Atmospheric Science

In partial fulfillment of the requirements
For the Degree of Master of Science
Colorado State University
Fort Collins, Colorado
Fall 2008

ABSTRACT OF THESIS

CAVITY RING-DOWN SPECTROSCOPY AND THE RETRIEVAL OF AEROSOL OPTICAL PROPERTIES FROM BIOMASS BURNING DURING FLAME2

Biomass burning occurs globally through both natural and human initiated fires. Aerosols produced by biomass burning are unique because of the wide range of fuel types and combustion conditions which occur. Aerosols from biomass burning have a wide range of optical properties which can lead to either atmospheric warming or cooling. More measurements of aerosol optical properties from biomass burning will give modelers a better understanding of how these aerosols influence radiative transfer. This work presents measurements of the optical properties of aerosols produced by biomass burning during the Fire Laboratory at Missoula Experiment 2 (FLAME2) study.

Measurements of aerosol extinction, scattering and absorption coefficients, as well as particle size distributions, were made during the FLAME2 study. Extinction measurements were made using an instrument employing cavity ring-down (CRD) spectroscopy, scattering measurements were made using a TSI nephelometer, absorption coefficient measurements were made using a photo-acoustic spectrometer (PAS) and size distributions were measured using the CSU sizing rack consisting of a differential mobility analyzer (DMA) and optical particle counter (OPC). The study was conducted at the U.S. Forest Service Fire Science Lab (FSL) in Missoula, Montana from May 20 - June 6, 2007 and burned 18 separate fuel types.

Optical closure between measurements of extinction, scattering and absorption coefficients was found indicating good agreement between instruments. Measurements of single scattering albedo (SSA) were found to have a strong relationship with elemental carbon mass fraction. FLAME2 SSA values agreed well with literature values and indicated a dependence on combustion conditions rather than fuel type. Using measured size distributions, measurements of extinction, scattering and absorption coefficients and Mie theory, a retrieval of the complex refractive index was developed. The complex refractive index retrieval was limited by measured size distributions for each burn, but values were obtained for six separate fuels. Values of FLAME2 retrieved refractive index were in the same range as values reported in the literature, although the imaginary index of refraction, *k,* was much larger during FLAME2.

A new instrument employing Cavity ring-down spectroscopy was used during FLAME2. Quality control tests were performed on the instrument after the study to check the performance of the instruments. Initial tests demonstrated low particle loss and high accuracy. It was later found that the PMT used by the instrument was contributing noise to the signal and measurements made during FLAME2 required a large correction.

The optical properties calculated in this study can be used, in conjunction with values from literature, to obtain a better estimate of the magnitude of the climate forcing caused by biomass burning aerosols.

Laura Elizabeth Mack
Atmospheric Science Department
Colorado State University
Fort Collins, CO 80523
Fall 2008

ACKNOWLEDGMENTS

This research was supported by the U.S. Department of Energy's Office of Science (BER) through the Western Regional Center of the National Institute for Climatic Change Research, grant number MPC35TA-A4. This work was also funded by the National Park Service contract number H2380040002, task number J2350064155. The FLAME study was supported by the Joint Fire Science Program (JFSP) and the National Park Service.

I would like to thank my advisor, Sonia Kreidenweis for her guidance and support throughout my research and writing process. I would like to thank my committee members, Jeffrey Collett and Azer Yalin for their advice and guidance. Hans Moosmüller and Daniel Obrist of the Desert Research Institute also deserve many thanks for building the CSU cavity ring-down spectrometer as well as providing assistance and answering numerous questions.

TABLE OF CONTENTS

LIST OF FIGURES

LIST OF TABLES

Chapter 1 INTRODUCTION

1.1 Aerosols

Aerosols, a suspension of a fine solid or liquid, are emitted directly into the atmosphere by anthropogenic (e.g. fuel combustion, industrial processes, transportation) and biogenic (e.g. soil, volcanoes, mineral dust) sources or formed indirectly in the atmosphere by gas-to-particle conversion processes [Seinfeld and Pandis, 2006]. Because aerosols are produced by a variety of sources both natural and anthropogenic, they have a global impact.

Aerosols can influence the atmosphere through changes in radiative transfer and visibility impairment as well as cause adverse human health effects. Currently, a lot of research is focused on determining the magnitude of the climate forcing caused by gasses and aerosols; Bond and Bergstrom [2006] define climate forcing as "the change in net radiative flux at the tropopause attributable to a specific component". Climate forcing caused by gasses, i.e. CO_2, is relatively well constrained compared to that caused by aerosols. One reason that climate forcing due to aerosols is difficult to determine is that changes in radiative transfer due to aerosols occur by direct and indirect means and can cause both positive and negative climate forcing (i.e. both warming and cooling of the atmosphere). Aerosols can indirectly affect climate by serving as cloud condensation nuclei (CCN), causing changes in the radiation budget through changes in cloud properties [*Crutzen and Andreae*, 1990]. Directly, aerosols influence the radiation budget by scattering and absorbing solar radiation; scattering aerosols can have a net cooling

effect that might mask some of the heating caused by CO_2 [*Liousse et al*., 1996], while aerosols which strongly absorb incoming radiation may cause heating similar to that of greenhouse gases.

1.2 Biomass burning

Biomass burning is an important source of aerosols because it occurs naturally as lighting ignited forest fires as well as anthropogenically via prescribed burns and agricultural burning. Biomass burning directly influences a large portion of the globe because of local smoke emissions (Figure 1-1) as well as indirectly impacting a larger part of the globe via transport of smoke plumes.

Aerosols produced by biomass burning can contain a large amount of light absorbing carbon (LAC), sometimes referred to as "soot" or "elemental carbon". LAC can strongly absorb incoming radiation, lower the single scattering albedo (SSA) and contribute to a warming of the atmosphere [*Hansen et al.,* 1981]. The amount of LAC produced by biomass burning as well as the specific optical properties of LAC can vary [*Bond and Bergstrom*, 2006], producing varying values of SSA.

Optical properties of aerosols produced by biomass burning are important because of the global impact of these aerosols as well as the wide range of radiative effects, i.e. atmospheric warming or cooling. Obtaining a better estimation of the optical properties is beneficial for a better understanding the climate forcing caused by the aerosols produced. A better understanding of the climate forcing due to biomass burning will help global climate models better predict future trends in global temperature.

1.3 Aerosol interaction with light

The relationship between light and aerosols is complicated and depends on a number of properties of the aerosol (i.e. particle size, refractive index, morphology) as well as the wavelength of the incident light. When electromagnetic waves encounter a particle, electrons in the particle can be excited. This excitation can be reradiated as scattered light or converted to thermal energy by absorption. The magnitude of particle scattering or absorption of electromagnetic waves is dependent on the wavelength of the incident light λ, the size of the particle D_p and the index of refraction of the material

$$m = n + ik \tag{1-1}$$

where n is the real part of the index of refraction and k is the imaginary part of the index of refraction. The size parameter α

$$\alpha = \frac{\pi D_p}{\lambda} \tag{1-2}$$

is a dimensionless parameter which is often used to describe the relationship between the particle size and the wavelength of the incident light.

The amount of energy scattered and absorbed by the particle is proportional to the incident energy and the proportionality constant is called the single-particle scattering or absorption cross section, σ_{scat} and σ_{abs} with units of m^2. Dividing σ_{scat} and σ_{abs} by the cross sectional area of the particle we obtain the dimensionless scattering and absorption efficiencies of the particle, Q_{scat} and Q_{abs}. The total energy which is scattered and absorbed by the particle is called the extinction and is the addition of the scattering and absorption of the particle.

$$\sigma_{ext} = \sigma_{scat} + \sigma_{abs}$$

$$Q_{ext} = Q_{scat} + Q_{abs} \quad \text{1-3}$$

The single scattering albedo (SSA) is defined as

$$\omega = \frac{\sigma_{scat}}{\sigma_{ext}} = \frac{Q_{scat}}{Q_{ext}} \quad \text{1-4}$$

and describes the fraction of total light extinction caused by scattering; the fraction of light extinction caused by absorption is 1-ω.

Mie theory describes the complex interaction of electromagnetic radiation with particles. Using Mie Theory it is possible to calculate the scattering and absorption of light for any spherical particle given the wavelength, index of refraction and particle size [*Bohren and Huffman*, 1983]. When the size parameter is very large, α>>1, Mie theory can be approximated using geometric scattering; when the size parameter is very small, α<<1, Mie theory can be approximated by Rayleigh scattering.

For light scattered by particles, it is also important to describe the direction of the scattered light. The phase function of a particle at a given wavelength describes the angular distribution of the light scattered by a particle.

$$P(\theta, \alpha, m) = \frac{F(\theta,\alpha,m)}{\int_0^{\pi} F(\theta,\alpha,m) sin\theta d\theta} \quad \text{1-5}$$

where $F(\theta,\alpha,m)$ is the light intensity scattered into the direction θ. Two other parameters, the asymmetry parameter g and the hemispheric backscatter ratio b, are useful in determining how much light is scattered in the forward versus the backward directions. For particles in the Rayleigh regime, α<<1 corresponding to D_p < 0.1 μm for visible wavelengths, particles scatter isotropically (the same in all directions) whereas particles in the geometric regime, α>>1, scatter primarily in the forward direction. The phase

function has a large dependence on the assumption of particle shape; for spherical particles, assumed by Mie Theory, phase function is independent of the angle of incidence.

When electromagnetic radiation passes through an atmospheric layer, light extinction occurs through the relationship

$$dF = \mathrm{F}_0 \exp(-b_{ext} dz) \qquad 1\text{-}6$$

where dF is the incremental change in intensity through the layer, F_0 is the incident intensity, dz is the depth of the layer and b_{ext} is the extinction coefficient of the layer. The extinction coefficient b_{ext} has units of m^{-1} but for typical atmospheric levels units of Mm^{-1} are used. Similarly as with extinction cross section and extinction efficiency, we can write b_{ext} as the summation of the scattering coefficient and absorption coefficient.

$$b_{ext} = b_{scat} + b_{abs} \qquad 1\text{-}7$$

Scattering and absorption coefficients can be further broken down into contributions from gasses and particles, b_{sg}, b_{sp}, b_{ag} and b_{ap} where the subscripts indicate absorption a, scattering s, gasses g and particles p. Scattering due to gasses, b_{sg}, is known as Rayleigh scattering and has well understood optical properties.

The extinction, scattering and absorption coefficients of particles are related to the extinction, scattering and absorption cross sections through the relationship

$$b_{ext} = \sigma_{ext} N$$

$$b_{scat} = \sigma_{scat} N$$

$$b_{abs} = \sigma_{abs} N \qquad 1\text{-}8$$

where N is the total particle number concentration of particles at the specified cross section, σ_{ext}, σ_{scat} and σ_{abs}. Because the extinction cross-section is dependent on particle

size, when sampling a distribution of particle sizes, the total extinction coefficient is the sum of the extinction over all measured particle sizes.

$$b_{ext} = \sum b_{ext,i} = \sum \sigma_i N_i \qquad 1\text{-}9$$

1.3.1 Single scattering albedo measurement

Single scattering albedo (SSA) is important in determining the extent that particles in the atmosphere will scatter light versus how much they will absorb light. SSA values less than 0.85 indicate a significant contribution from absorption at 532 nm and would likely contribute to atmospheric warming while SSA values near one indicate the likelihood of atmospheric cooling. Measuring the SSA of aerosols can then help predict the degree that aerosols will cause atmospheric warming or cooling.

Uncertainty in SSA measurements is dependent on uncertainties associated with the extinction, scattering and absorption measurements. If SSA is calculated using measurements of b_{ext} and b_{scat}, the relative uncertainty in SSA is dependent only on the relative uncertainties in extinction and scattering measurements

$$\frac{\Delta\omega}{\omega} = \sqrt{\left(\frac{\Delta b_{ext}}{b_{ext}}\right)^2 + \left(\frac{\Delta b_{scat}}{b_{scat}}\right)^2} \qquad 1\text{-}10$$

where Δb_{ext} and Δb_{scat} are the uncertainties associated with b_{ext} and b_{scat}. Assuming relative uncertainty values of 5% for extinction coefficients (*3.5 Measurement uncertainties*) and 1% for scattering coefficients [*Anderson and Ogren*, 1998], the relative uncertainty in SSA is 5.1%, larger than the individual uncertainties in extinction and scattering.

If SSA is calculated using measurements of scattering and absorption, relative uncertainty in SSA becomes dependent on the magnitude of b_{scat} and b_{abs} as well as the uncertainty in Δb_{scat} and Δb_{abs}

$$\frac{\Delta\omega}{\omega} = \sqrt{\left(\frac{b_{scat}}{b_{scat}+b_{scat}}\Delta b_{abs}\right)^2 + \left(\frac{b_{abs}}{b_{scat}+b_{abs}}\Delta b_{scat}\right)^2} \quad \text{1-11}$$

To determine the impact that scattering and absorption coefficients have on SSA relative uncertainty, values were chosen for Δb_{scat}, Δb_{abs}, b_{scat} and b_{abs} which reflect typical values. Relative uncertainty values of 5% for absorption [*Lewis et al.*, 2008] and 1% for the scattering coefficients [*Anderson and Ogren*, 1998] were assumed. Four values of total extinction coefficient, 25, 50, 75 and 100 Mm^{-1}, were assumed and were chosen to reflect typical atmospheric levels of extinction coefficient [*Watson*, 2002]. Scattering and absorption coefficients were varied to total to the chosen extinction coefficients and to give values of SSA from 0 to 1.

Relative uncertainty in SSA has a maximum value of 1.2% at SSA of 0.5, halfway between that of b_{scat} and b_{scat} (Figure 1-2). Relative uncertainty decreases at low and high values of SSA, where either scattering or absorption dominates. Thus the relative uncertainty in SSA is constantly greater than the uncertainty in either measurement if calculated using b_{ext} and b_{abs}; relative uncertainty is less when SSA is calculated using measured values of b_{scat} and b_{abs} and is smallest when either scattering or absorption dominates and SSA is close to 0 or 1.

1.3.2 Size distribution influence on optical properties of aerosols

Mie Theory predicts that the extinction efficiency of a particle is dependent on the wavelength λ and index of refraction m of the particle and oscillates with size; Q_{ext}

approaches 2 with increasing in particle size. Scattering and absorption efficiencies also oscillate with particle size; the values that Q_{scat} and Q_{abs} asymptotically approach depend on refractive index of the material. More specifically, the relative contributions of scattering and absorption to total extinction are dependent on size parameter, α.

For wavelength λ = 550nm, the extinction, scattering and absorption efficiencies were plotted versus particle size for two values of refractive index (Figure 1-3 and Figure 1-4). At small particle sizes (D_p < 0.1 μm), the total extinction is primarily due to absorption while accumulation mode particles (D_p < 1 μm) have a larger contribution from scattering. In the geometric regime, (size parameter α >>1, here equivalent to D_p > 10 μm), extinction, scattering and absorption coefficients no longer oscillate.

A possible consequence of the size dependence of absorption and scattering is that small particles (D_p < 0.1 μm) which are more likely to be lost through diffusion to sampling tubes during the sampling process are typically more absorbing. This would cause a decrease in the measured absorption signal of the aerosol, yielding a higher SSA.

1.4 Cavity Ring Down

A new instrument which measures the total light extinction of particles was used to measure the optical properties of emissions from biomass burning. Measurements were made during the Fire Laboratory At Missoula Experiment 2 (FLAME2) performed at the Fire Science Laboratory in Missoula Montana. The instrument employs the principal of cavity ring-down spectroscopy to measure the total light scattering and absorption caused by particles and gasses.

Cavity ring-down is an improvement on previous techniques of particle light extinction measurement, by creating long path lengths over which a laser pulse can

decay. The long path lengths are simulated by reflecting a laser pulse between highly reflective mirrors and are desirable because they increase the sensitivity of the measurement making it possible to measure very low values of extinction. Cavity ring-down spectroscopy has been shown to be very sensitive to light extinction and can be used in conjunction with measurements of scattering coefficients, absorption coefficients and size distributions to obtain the SSA and refractive index of aerosols [*Riziq et al.*, 2007].

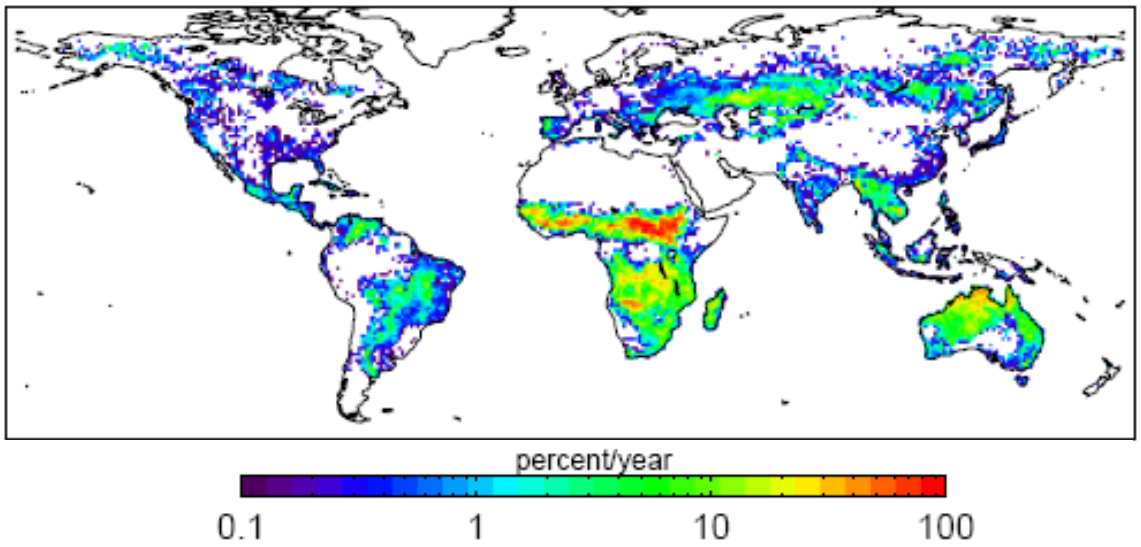

Figure 1-1 *Mean annual fire burned area for 2001-2004 derived from Terra MODIS active fire observations expressed as percent of grid cell burned that year (adapted from [Giglio et al., 2006] figure 11).*

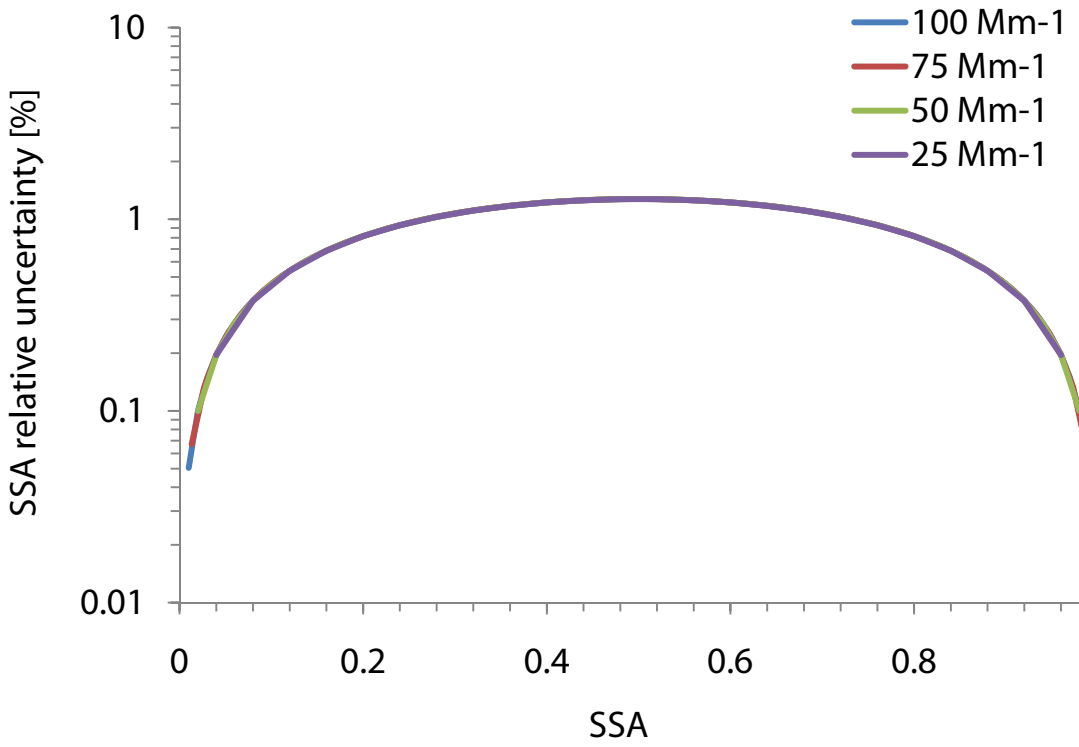

Figure 1-2 *Relative uncertainty in SSA using four different values of total extinction coefficient: 100, 75, 50, 25 Mm-1 and relative uncertainties of b_{scat} and b_{abs} of 5% and 1% respectively. SSA relative uncertainty is maximum for SSA of 0.5 and independent of total extinction.*

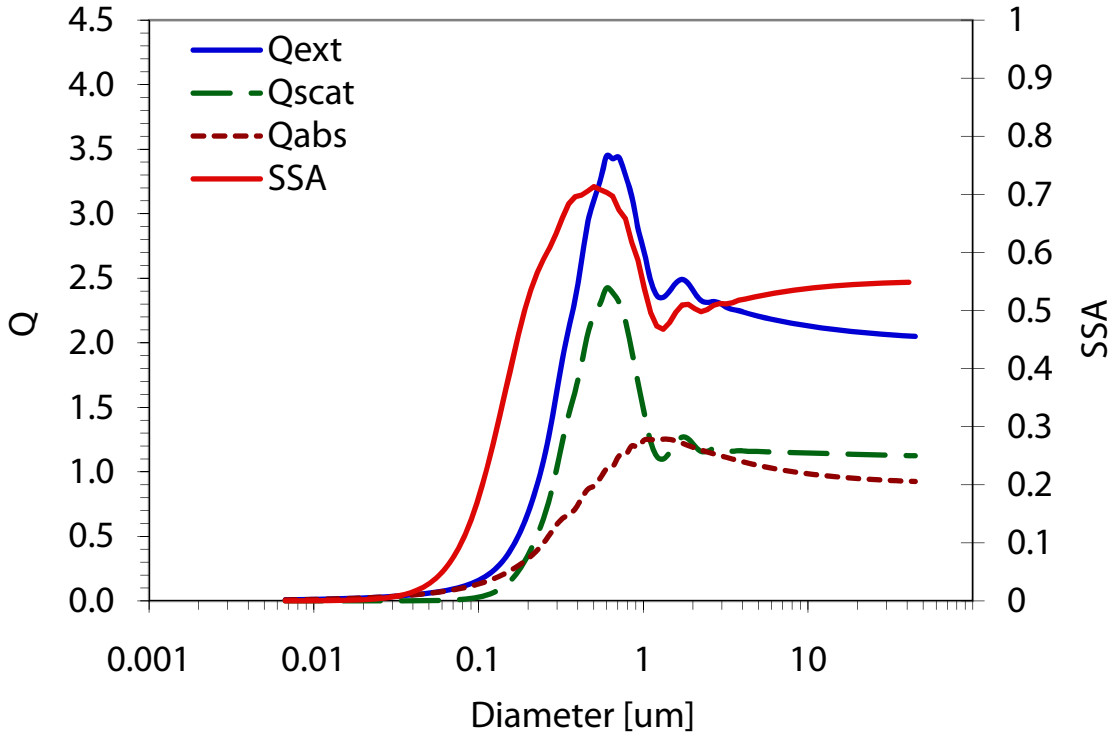

Figure 1-3 *Plot of extinction, scattering and absorption efficiencies versus particle size where λ = 550 nm and m = 1.53+0.1i.*

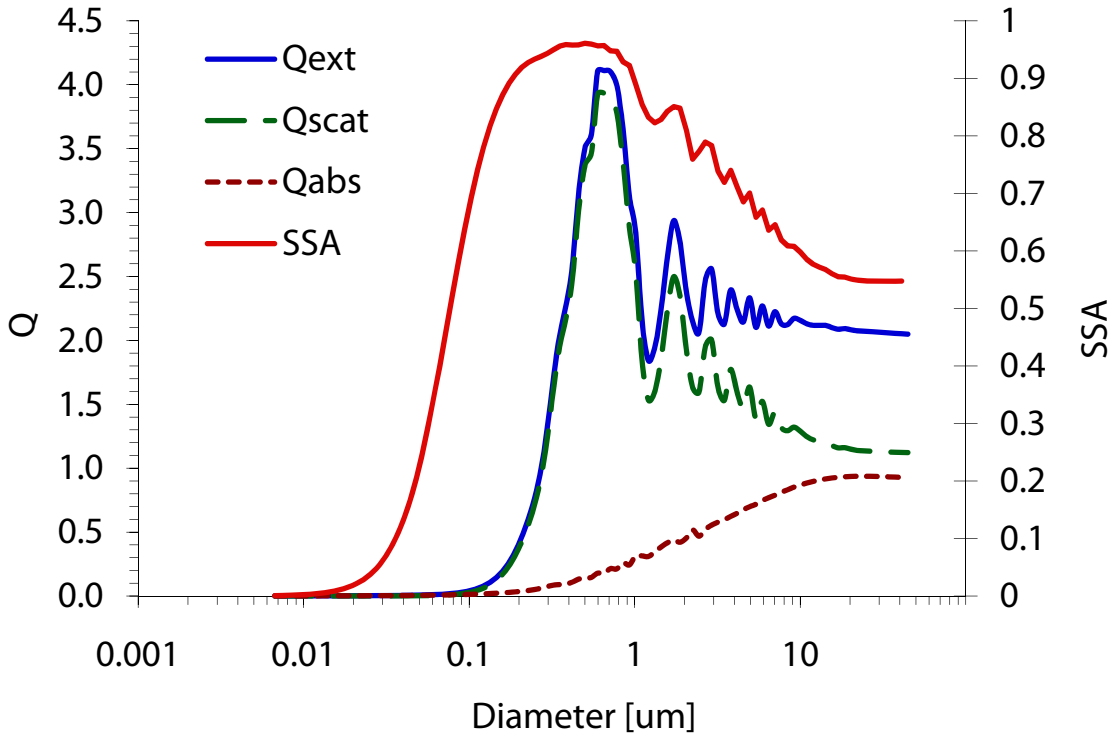

Figure 1-4 *Plot of extinction, scattering and absorption efficiencies versus particle size where λ = 550 nm and m = 1.53+0.01i.*

Chapter 2 CSU CAVITY RING-DOWN SPECTROMETER

2.1 Cavity Ring-down Spectroscopy

Cavity ring-down (CRD) spectroscopy, the measurement of light decay by extinction of light in a high-resonant cavity, was developed in 1988 by O'Keefe and Deacon to measure the absorption spectra and consequently the concentrations of gasses [*Okeefe and Deacon*, 1988]. More recently [*Sappey et al.*, 1998; *Smith and Atkinson*, 2001] CRD spectroscopy has been expanded to aerosol measurements.

Cavity ring-down creates a long path-length over which light can travel by using a beam from a pulsed (or chopped continuous wave) laser in a cavity with high reflectivity mirrors at each end. Each pulse of the laser enters the cavity and is reflected between the two mirrors, the light intensity decaying in time due to absorption and scattering by particles and gasses present between the mirrors. Each time the laser is reflected from the back mirror, a small fraction of light is transmitted through and is detected by a photomultiplier tube (PMT), the signal decay is then analyzed using an oscilloscope. The decay of the intensity of the light pulse can be modeled by Beer's law

$$I = I_0 \exp\left(\frac{-t}{\tau}\right) \qquad 2\text{-}1$$

where I is the measured intensity of the light pulse, I_0 is the incident light intensity, t is time and τ is the characteristic decay time constant, known as the ring-down. An advantage of CRD spectroscopy is that analysis is independent of pulse to pulse variations in the laser intensity. Differences in light intensity that might be present

between laser pulses do not affect analysis because only the decay of the intensity is analyzed, not the magnitude of the intensity.

The exponential time decay of the light pulse is dependent not only on the medium between the mirrors, but also on losses due to the mirrors. When there is no sample between the mirrors, as represented by a vacuum or medium which does not absorb or scatter light at the wavelength of interest, the ring-down for the cavity is

$$\tau_M = \frac{L}{c \ln R} \qquad 2\text{-}2$$

where τ_M is the ring-down of the cavity, L is the distance between the mirrors, c is the speed of light and R is the reflectivity of the mirrors. For CRD spectroscopy systems, R is typically on the order of 0.99 and can be approximated by $\ln R = 1 - R$ [*Berden et al.*, 2000].

$$\tau_M = \frac{L}{c \ln R} = \frac{L}{c(1 - R)} = \frac{1}{c b_M} \qquad 2\text{-}3$$

The observed ring-down, τ_{meas}, becomes more complicated in the presence of a sample in the cavity

$$\tau_{meas} = \frac{L}{c}\left[(b_M L + b_p L_p + b_g L_g\right]^{-1} = \frac{1}{c b_{meas}} \qquad 2\text{-}4$$

where L is the length of the cavity, c is the speed of light, b_M is the extinction due to the mirrors, b_p is the extinction coefficient due to particles, L_p is the length of the cavity the particles occupy, b_g is the extinction coefficient due to gasses, L_g is the length of the cavity the gasses occupy, and b_{meas} is the total measured extinction coefficient.

When using CRD spectroscopy to measure the extinction of light due to aerosols, a small purge flow of clean (zero) air or gas is needed to keep aerosols from depositing

on the mirror surfaces [*Smith and Atkinson*, 2001]. This purge flow creates a barrier around the mirror where the sample flow is not able to penetrate, causing a decrease in the volume the sample occupies in the cavity. If filtered ambient air is used as the purge gas, defining $L = L_S + L_{purge}$ where L_S is the distance the sample occupies in the cavity, we can write the total extinction measured by the CRD, b_{meas}, as

$$b_{meas} = b_S + b_M = b_{S\_S}\frac{L_S}{L} + b_g\frac{L_{purge}}{L} + b_M = (b_p + b_g)\frac{L_S}{L} + b_g\left(1 - \frac{L_S}{L}\right) + b_M$$

$$= b_p\frac{L_S}{L} + b_g\frac{L_S}{L} + b_g - b_g\frac{L_S}{L} + b_M = b_p\frac{L_S}{L} + b_g + b_M$$

$$b_p = \frac{L}{L_S}(b_{meas} - b_g - b_M) = \frac{L}{L_S}(b_{meas} - b_{filtered}) \qquad 2\text{-}5$$

where L/L_S is the ratio of the total length of the cavity to that filled by the sample, b_S is the measured extinction coefficient in the cell between the mirrors, b_{S_S} is the extinction in the cell due to the sample, b_g is the extinction due to gasses in the cavity (assumed to be the same as that of filtered air), b_p is due to particles and b_M is due to mirror losses [*Moosmuller et al.*, 2005]. The extinction coefficient measured for filtered air indicates extinction due to the mirrors and gasses present in the room air. Subtracting the filtered air extinction measurement from the total measured extinction coefficient and multiplying by the correction factor, L/L_S, yields the extinction due to aerosols. This is a valid correction as long as we assume that the mirror losses, Rayleigh scattering of room air, b_g, and pressure are constant throughout the sample period.

2.2 Extinction cell specifics

The Cavity Ring-Down extinction cell discussed in this work was built by Hans Moosmüller and Daniel Obrist from the Desert Research Institute and is similar to that built previously by Moosmüller [2005].

The cavity is constructed of a 34 mm diameter stainless steel tube, mounted on an aluminum optical breadboard 0.61x0.61x0.06 m (schematics shown in Figure 2-1 and Figure 2-2). The cavity is 0.5 m in length with a sample inlet in the middle of the cavity at 90 degrees to the cavity and two outlets located at each end of the cavity, 0.22 m from the inlet and 90 degrees to the cavity. Highly reflective mirrors (Los Gatos Research Inc., quoted reflectivity ≈ 99.9985%, 1" diameter) are mounted on each end of the cavity in mirror mounts which allow small alignment adjustments external to the cavity. The mirrors have a radius of curvature of 0.5 m and are placed 0.56 m apart. A small purge flow of filtered air, <1% of the total flow, is introduced approximately 2 mm in front of each mirror and is kept from mixing with the sample flow by an adjustable iris, set at a 3 mm diameter. The light pulse exiting the laser travels first through an optical isolator after which it is reflected through a backscattering window. The backscattering window diverts some of the light pulse towards a photo-diode which acts as a trigger for the digital oscilloscope. The portion of the pulse that is transmitted through the backscattering window is focused with a lens and reflected by two aluminum mirrors approximately 180 degrees so that it enters through the center of the cavity. Pressure inside the cavity is monitored with an Ultraclean Absolute Pressure Transducer (MKS Instruments 870B Baratron). Temperature and relative humidity are monitored with a temperature and relative humidity probe (Vaisala HMP50)

The laser is a pulsed, diode-pumped, passively Q-switched PowerChip Nd:YAG laser (Teem Photonics PNG-002025-100) at 532 nm with a repetition rate of 1kHz. The laser pulse width is less than 1ns with mean pulse energy of 31.5 μJ and average power of less than 300 mW. The laser pulse width, less than 1 ns, translates to a physical length of 0.3 m which is less than the length of the cell, 0.5 m. On the opposite side of the cavity from the laser source, a 532 nm band-pass filter and photomultiplier tube (PMT) (Hamatasu 7732-01) are attached to the back of the mirror mount. From the PMT, the signal is digitized by a 5 MHz digital oscilloscope card (GAGE, CompuScope 12100) with a 50 Ω impedance. A National Instruments Labview virtual instrument built by Los Gatos retrieves the ring-down at a rate of 60 samples per second averaging every 10 samples. The first 10 points of each fit are rejected to eliminate possible multi-exponential decays due to non-linear PMT response, electronic noise and multiple spatial modes in the cavity [*Baynard et al.*, 2007; *Thompson et al.*, 2002; *Thompson et al.*, 2003]. The data output by the Labview virtual instrument gives average ring-down τ, standard deviation of ring-downs $\Delta\tau$, average extinction coefficient b_{ext} and standard deviation of extinction coefficients Δb_{ext} at a rate of 6 data points per second.

The optical table, a Pentium 4 CPU, sample pump, filtered air purge flow pump and the controls for the PMT, temperature, pressure and RH sensors are mounted in a 25”x29”x64” instrument rack. To facilitate filtered air measurements, a 3-port valve with an electrical actuator is located prior to the inlet which can direct sample flow directly into the cavity or through a filter. The valve is controlled and environmental parameters are monitored through Labview. Values of extinction coefficient calculated by the

instrument are reported in units of Mm^{-1} or $1/10^6$m. This unit is commonly used to express extinction, scattering or absorption coefficients of atmospheric aerosols.

2.3 Theoretical uncertainty

Measurement uncertainty is dominated by aerosol number fluctuations in the laser beam when measuring particles with the CRD [*Pettersson et al.*, 2004]. When no aerosol is present, instrumental fluctuations dominate measured uncertainties and the instrumental limit is given by [*Pettersson et al.*, 2004]

$$b_{\min} = \frac{R_L}{c} \frac{\sqrt{2} s(\tau_0)}{\tau_0^2 \sqrt{RT}} \qquad 2\text{-}6$$

Where R_L is the ratio of the total length of the cavity to that filled by the sample, $s(\tau_0)$ is the minimum detectable change in the ring down time for one laser shot, τ_0 is the background ring down time, R is the repetition rate and T is the sampling time. For our system R = 1kHz = 1000 Hz, $\tau_0 \approx 80$ μs (our best tau from laboratory alignment) and $s(\tau_0)$ ≈1 μs giving a limit of 0.011 Mm^{-1} for an averaging time of T = 5 seconds. Sensitivity was calculated as a function of averaging time T, shown in Figure 2-3. The sensitivity curve was calculated using fixed values of τ_0 and $s(\tau_0)$ although it is expected that at some large value of T, fluctuations associated with the sample or environmental parameters would cause $s(\tau_0)$ to increase, increasing b_{min}.

When the number of particles in the cavity is small, statistical fluctuations in the number concentration in the light pulse can have a large effect on extinction. Using Poisson statistics, we can describe the error associated with the fluctuations in aerosol number concentrations [*Pettersson et al.*, 2004]

$$\frac{\Delta b_{stat}}{b_{meas}} = \frac{1}{\sqrt{NVRT}} \qquad 2\text{-}7$$

where b_{meas} is the measured extinction, N is the mean aerosol number concentration, R is the repetition rate of the laser, T is the sampling time, V is the effective laser beam volume and Δb_{stat} is the statistical uncertainty associated with the aerosol concentration. Using R = 1 kHz = 1000 Hz, T = 5 seconds, and using Gaussian beam theory to calculate the effective sample volume of the cavity, V = 0.07 cm^3, we can determine the uncertainty associated with aerosol concentration (Figure 2-4). At low aerosol particle concentrations the relative uncertainty in extinction measurement is larger than at high particle concentrations.

Combining instrumental fluctuations and variations in number concentration in the effective laser volume we obtain [*Pettersson et al.*, 2004]

$$\Delta b = \sqrt{\frac{b_{meas}^{\ 2}}{NVRT} + b_{\min}^2} \qquad 2\text{-}8$$

Using the value calculated for b_{min}, and extinction coefficient and particle concentration measurements from a PSL experiment described in Chapter 3, the relative error $\Delta b/b_{meas}$ is calculated (Figure 2-5). As extinction coefficient increases, the relative error in extinction coefficient measurement decreases, similar to what was observed for the relative uncertainty in extinction with particle concentration.

Angular patterns in scattering by particles could also cause uncertainty in the measurement of extinction coefficient. Based on the geometry of the TSI integrating nephelometers it was found that there was angular truncation below 7˚ and beyond 170˚ [*Anderson and Ogren*, 1998], introducing a large error when sampling large particles. In the CRD light scattered directly into the forward and backward directions would be

detected by the PMT as if it were unattenuated, yielding an incorrect larger extinction coefficient. It is typically assumed that the angle at which truncation occurs in the CRD system is too small to cause significant error at particle sizes typically measured i.e., less than several microns [*Baynard et al.*, 2007; *Pettersson et al.*, 2004].

2.4 Comparison to other instruments

Table 2.1 presents a short comparison of CRD instruments applied to the measurement of aerosol extinction, including the one used in this study. Most of the previously built CRDs are longer in length than our system, typically 1 m in length compared with 0.5 m for ours, while the instrument built by Strawa [2003] is significantly shorter. The shorter length of our cavity is beneficial in making our instrument easier to move, making it possible to transport and use in field studies. The wavelength of our CRD is similar to that used in many of the other CRDs; 532 nm is a crucial wavelength to observe as it is near to the spectral maximum of solar irradiance. Due in part to the high reflectivity of the mirrors and laser power, our instrument is capable of τ_0 values higher than many of those reported for previous studies. An increased value of τ_0 indicates an increase in the effective path length of the laser pulse giving better sensitivity at low values of extinction and increasing the maximum measurable extinction coefficient. During the FLAME 2 study in the summer of 2007 the instrument was able to measure extinction coefficients as high as 5,000 Mm^{-1}, significantly higher than typical atmospheric values. The theoretical sensitivity of our instrument, 0.011 Mm^{-1} is significantly smaller than those reported by other studies largely due to the increased value of τ_0 capable of our instrument.

Table 2.1 *Comparison of Cavity Ring-Down spectrometers for aerosol extinction measurement*

Author	Length [cm]	Wavelength [nm]	Maximum ring-down [µs]	Sensitivity	Uncertainty/Accuracy
[Sappey et al., 1998]	*98*	*532*	*107*	*not reported*	*not reported*
[Smith and Atkinson, 2001]	*96*	*1064, 532, 355*	*5*	*1 Mm^{-1} (calculated from standard deviation with little averaging)*	*not reported*
[Thompson et al., 2002]	*169*	*510, 578*	*7.6, 8.7*	*1 Mm^{-1} (calculated from standard deviation of average of 1500 ringdowns)*	*2% (comparison to gasses)*
[Bulatov et al., 2002]	*75*	*620*	*1.7*	*8 Mm^{-1} (propagating error between extinction coefficient and ring-down time)*	*not reported*
[Strawa et al., 2003]	*20*	*690, 1550*	*not reported*	*minimum 1.5 Mm^{-1} (ammonium sulfate aerosol tests)*	*not reported*
[Pettersson et al., 2004]	*65*	*532*	*75*	*0.27 Mm^{-1} (calculated considering instrumental fluctuations)*	*5% (comparison to PSL)*
[Moosmuller et al., 2005]	*91*	*532*	*not reported*	*0.18 Mm_{-1} (standard deviation for 1 min average)*	*not reported*
[Baynard et al., 2007]	*87.4 (1064nm, 532nm, 355nm), 93.2 (683nm)*	*1064, 532, 355, 683*	*123, 75, 3.9, 82*	*0.43, 0.2, 9.2, 0.37 (calculated considering instrumental and number concentration fluctuations)*	*1% (based on statistical fluctuations of particle number density averaged at 1 min)*
[Riziq et al., 2007]	*93*	*532*	*16*	*0.377 Mm_{-1} (calculated from standard deviation of 400 laser shots measuring dry nitrogen)*	*not reported*
This study	*50*	*532*	*80*	*0.011 Mm^{-1} (calculated considering instrumental fluctuations)*	*10% (comparison to PSL)*

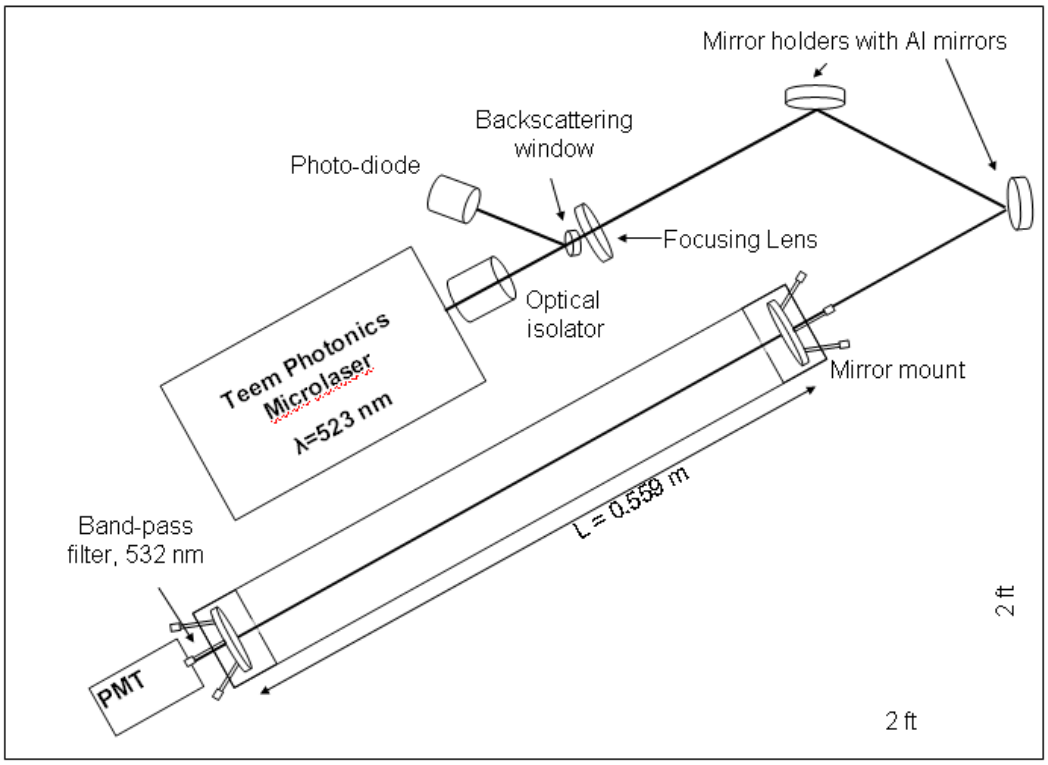

Figure 2-1 *Schematic of CSU cavity ring-down extinction cell*

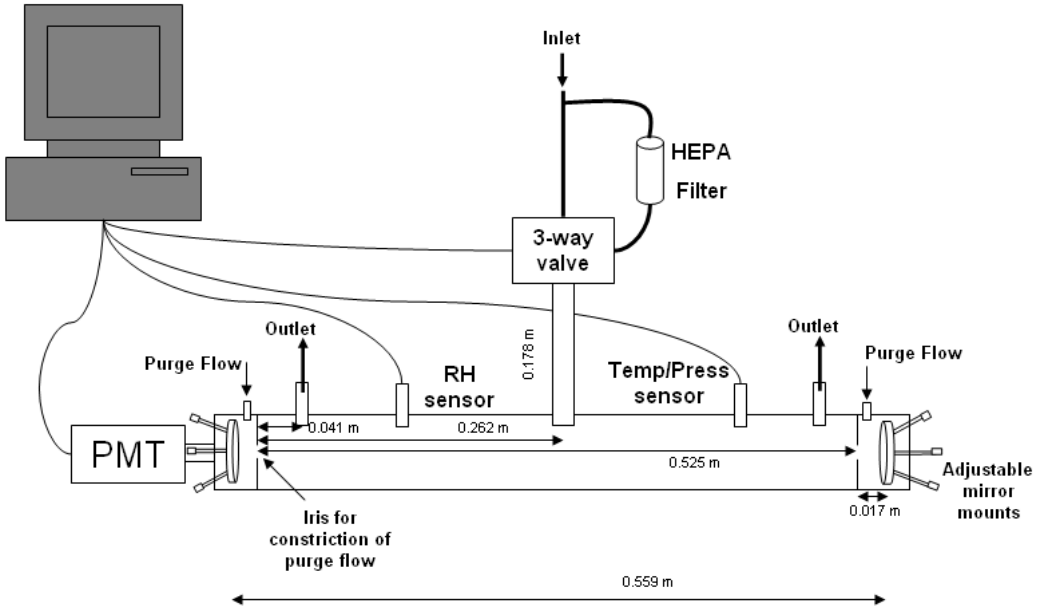

Figure 2-2 *Side view schematic of cavity ring-down extinction cell. Arrows indicate direction of flow.*

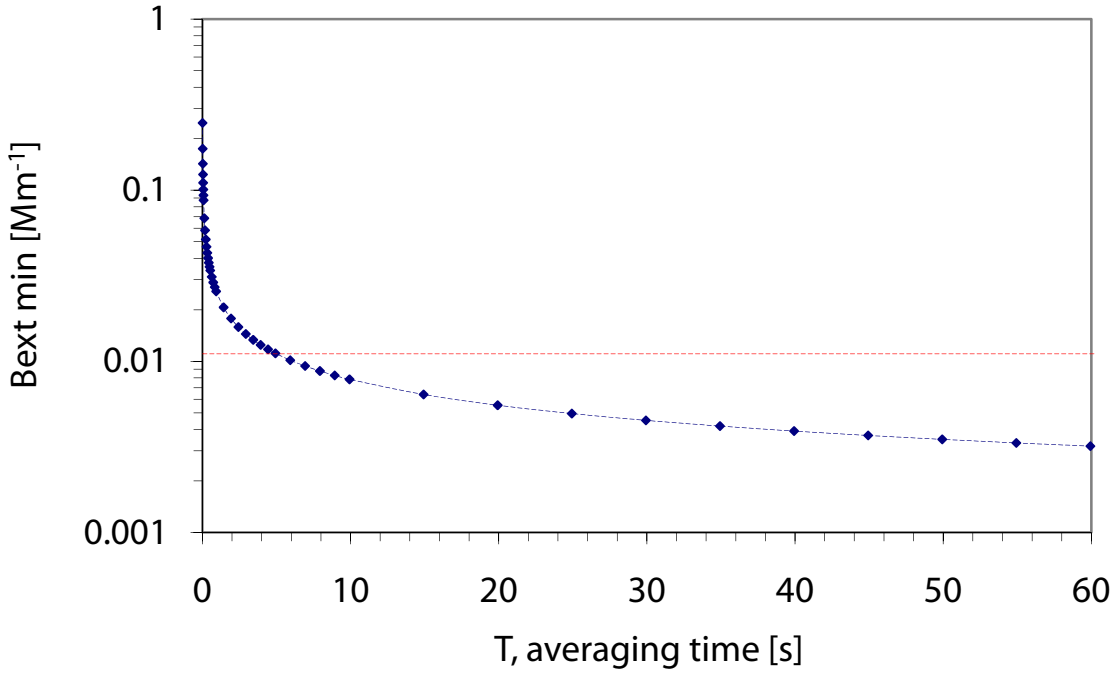

Figure 2-3 *Plot of minimum measurable extinction versus averaging time for τ_0 = 170 μs and $s(\tau_0)$= 1 μs. The red dashed line indicates the minimum measurable extinction with a 5 second averaging time.*

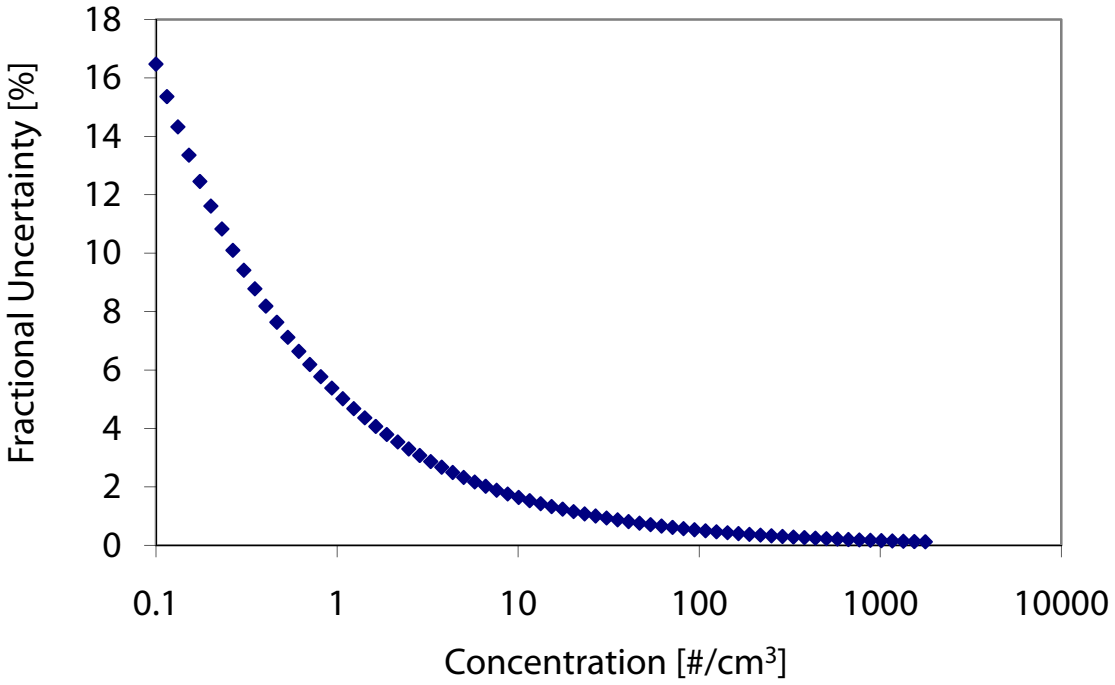

Figure 2-4 *Plot of* $\frac{\Delta b_{stat}}{b_{meas}}$ *vs. aerosol concentration. Smaller particle concentrations cause a larger variability in the relative error.*

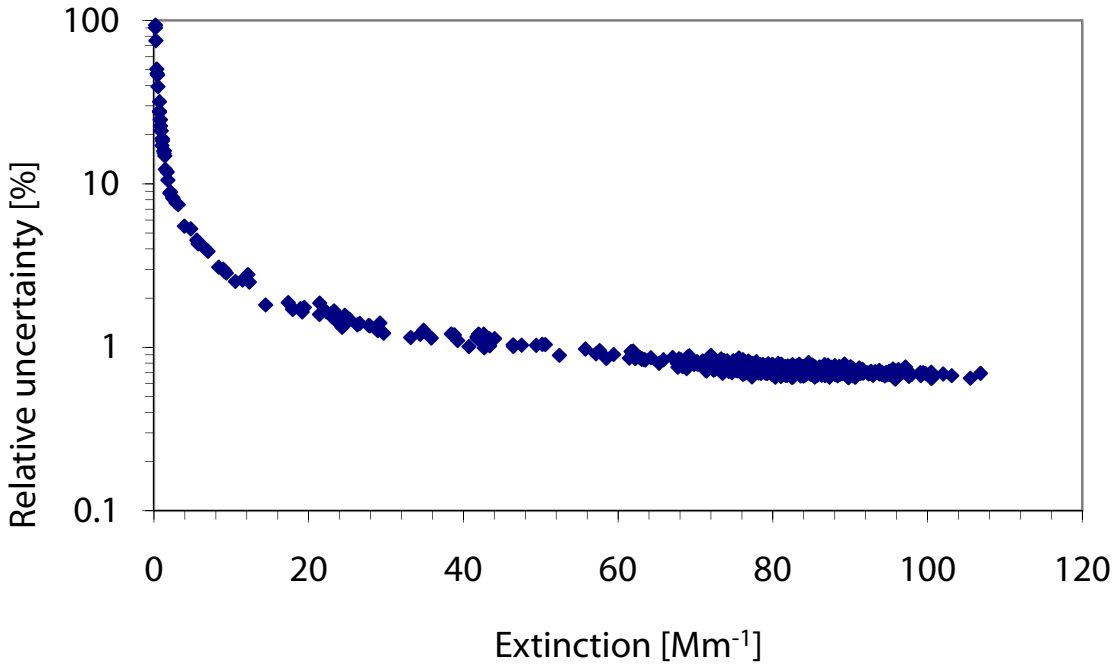

Figure 2-5 *Plot of* $\frac{\Delta b_{stat}}{b_{meas}}$ *vs. extinction coefficients measured for 500 nm PSL tests (discussed in Chapter 3). Fractional error in extinction coefficient measurement increases as extinction coefficient decreases.*

Chapter 3 QUALITY CONTROL AND CALIBRATION OF THE CRD INSTRUMENT

3.1 Performance tests of CRD

According to cavity ring-down theory, the measurement of extinction coefficients using cavity ring-down is absolute and requires no calibration if all the variables in equation 2-5 are known. In spite of this, tests were performed on the CSU CRD to check the accuracy, precision and performance of the instrument.

The CRD extinction cell was calibrated using monodisperse polystyrene latex spheres (PSL) of several diameters with known optical properties at 532 nm. Particle losses were determined using two condensation particle counters (CPCs) sampling monodisperse ammonium sulfate aerosol particles ($(NH_4)_2SO_4$) at multiple ports. Theoretical particle losses were calculated using literature corrections based on flow rate, inlet angle, inlet sizes as well as tube size and length.

3.2 PSL calibrations

CRD measurements of the extinction due to an aerosol of known optical properties, particle size and number concentration can be compared with values calculated from Mie theory using

$$b_{ext} = \sigma_{ext} N \qquad 3\text{-}1$$

where b_{ext} is the measured extinction, σ_{ext}, is the theoretical single particle extinction cross section and N is the measured particle number concentration.

Polystyrene latex spheres (PSL) are manufactured spherical particles of known size and optical properties and thus an excellent calibration aerosol [*Baynard et al.*, 2007; *Lack et al.*, 2006; *Pettersson et al.*, 2004; *Strawa et al.*, 2003]. Accuracy tests were done using Duke Scientific PSL, 0.3 μm (3K-300), 0.4 μm (3K-400), and 0.5 μm (PI-003 D) particles. The 0.5 μm PSL solutions came more highly concentrated than the other solutions, thus we used a mixture diluted 1:10 with ultrapure water. The particle sizes were chosen considering the available PSL diameters, the number concentrations needed to produce measurable extinction and the number concentrations producible by the experimental setup. To produce measureable extinction coefficient values, larger particle diameters are needed, while smaller diameters were needed to maintain large flow ratios in DMA1 (experimental setup described below). DMA1 flow rates were selected to maximize the ratio between sheath and sample flows, measure at the appropriate particle size and provide enough flow for the CRD, UCPC and DMA2 (Figure 3-1).

The PSL solutions were atomized using a medical nebulizer (capacity 0.004 L). The spray was dried by passing through two silica desiccant dryers in series (RH < 20% recorded by the CRD). Particles were then passed through a neutralizer and sent to a differential mobility analyzer (DMA1, TSI model 3080), with the flow rates and selected mobilities listed in Table 3.1. Filtered room air was used as sheath flow for DMA1 and DMA2.

Table 3.1 *DMA 1 flow rates, mobilities and diameters for PSL tests*

PSL diameter [μm]	Sheath [lpm]	Sample [lpm]	z [m^2/Vs]	± Δz [m^2/Vs]	Mid D_p (Max, Min) [μm]
0.299	10	3.3	5.26E-09	1.73E-09	0.3 (0.39941, 0.24726)
0.404	7.5	4.3	3.51E-09	2.01E-09	0.4 (0.77944, 0.28962)
0.500	4	0.4	2.61E-09	2.61E-10	0.5 (0.54277, 0.46505)

Since contamination from the atomizer (from the water or residue from the PSL solutions) or agglomeration of the PSL particles could have introduced particles of other sizes, DMA1 was used to select only those particles of the desired monodisperse size. The monodisperse output from DMA1 was diluted with filtered air to balance flow differences between DMA1 and the total flow rate for the CRD, UCPC and DMA2. The sample was then split and sent to an ultra fine particle counter (UCPC, TSI model 3776, flow rate 0.3 lpm) for particle number concentrations measurements, a second differential mobility analyzer (DMA2, TSI model 3080, flow rates listed in Table 3.2) to measure sample size distributions, and to the CRD for extinction coefficient measurements (Figure 3-1). For these experiments the CRD was run with a sample flow of 3 lpm and a purge flow of 0.025 L, 0.1% of the total flow. A particle impactor was used after DMA 1 for the 0.5 μm PSL particles to give a size cut at approximately 613 nm, eliminating larger coagulated 0.5 μm particles from entering the quasi-monodisperse flow measured by the UCPC, CRD and DMA2.

Table 3.2 *DMA2 flow rates*

PSL diameter [µm]	Sheath [lpm]	Sample [lpm]
0.299	2	0.3
0.404	5	1
0.500	2	0.3

Size distributions from DMA2 were obtained using the TSI scanning SMPS software. Sizes were scanned using an upscan, from small to large diameters, with a scan time of 5 minutes for the 0.3 and 0.5 μm PSL and 3 minutes for the 0.4 μm PSL. The range of the scan was changed for each PSL size to eliminate sizes where no particles were present. The SMPS software automatically corrected for multiply charged particles. Particle number concentration for the size distributions were measured using a water

condensation particle counter, TSI 3785. Size distributions from DMA2 (Figure 3-2, Figure 3-3, Figure 3-4) confirmed that particles only of the desired size were sampled.

For the 0.3 μm and 0.4 μm PSL, two and four runs were done respectively (a run constituted the nebulizer being filled with PSL solution and sampled until dry), for the 0.5 μm PSL only one run was done. Filtered air measurements were taken with the CRD before and after each run, and b_{ext} of the aerosol was calculated according to Chapter 2. A correction of 1.03 was also applied to correct for particle losses as is described later in *3.3 Particle Losses.* The CRD data, obtained at a frequency of 6 samples per second, and UCPC data, obtained at a frequency of one sample every 5 seconds, were averaged to the same time scale as the scanned size distributions (i.e. 3 or 5 minutes).

Values of extinction cross section, $\sigma_{ext}calc,$ were calculated with a Mie code using an index of refraction $m = 1.598+0i$ at 532 nm [*Pettersson et al.*, 2004] and the manufacturer's stated mean diameter of the PSL particles. Average measured extinction cross sections, $\sigma_{ext}meas$, were determined by plotting CRD measured extinction coefficients, b_{ext}, against UCPC concentrations N as shown in Figure 3-5, Figure 3-6 and Figure 3-7, the slope is equal to the measured cross section.

$$b_{ext} = \sigma_{ext}measN \qquad 3\text{-}2$$

It must be noted that all measured concentrations were less than 150 particles/cm^3 and when particle density is in this range, particle number fluctuations in the laser beam dominate uncertainty in measured extinction [*Pettersson et al.*, 2004]. A 10% uncertainty was used for the UCPC particle concentration measurements as stated by the manufacturer.

To determine whether the measured and calculated values of extinction cross section were statistically different, a t-test was performed using

$$\sigma_{ext}calc - \sigma_{ext}meas = \frac{ts}{\sqrt{N}} \qquad 3\text{-}3$$

where t is determined using the desired confidence level and degrees of freedom present (N-2), s is standard deviation of $\sigma_{ext}meas$ and N is the total number of data points used to determine $\sigma_{ext}meas$. A statistical difference at the 95% confidence level was found between the measured and calculated values of σ_{ext} for all three PSL sizes tested (Table 3.3) indicating that the measured values of σ_{ext} were not within statistical error of the calculated values.

Table 3.3 *Results of a t test performed to determine if measured and calculated were statistically different at 95% confidence level.*

Diameter [μm]	σ_{ext} meas [μm²]	σ_{ext} calc [μm²]	t	σ_{ext} calc- σ_{ext} meas [μm²]	Confidence interval	Statistically different?
0.299	0.158 ± 0.005	0.138	2.36	-0.020	0.005	Yes
0.404	0.372 ± 0.055	0.401	2.16	0.028	0.014	Yes
0.500	0.719 ± 0.047	0.763	2.31	0.044	0.036	Yes

Calculated and measured extinction cross sections for PSL particles were compared for this study and those measured by Pettersson [2004] (Table 3.4). Comparing all values, Pettersson reported an overall accuracy of <5% while this study indicated an overall accuracy of <10% (Figure 3-8); the overall accuracy was determined from the slope. Considering each size individually (Table 3.4, Table 3.5), Pettersson reported better accuracy at larger diameters (e.g. 0.4 – 1 μm) than at diameters less than 0.300 μm. This study underestimated σ_{ext} for 0.404 and 0.500 μm particles and showed an overestimation of σ_{ext} for 0.3 μm particles

Table 3.4 *Measured and calculated values of σ_{ext} as reported by Pettersson 2004.*

Diameter [µm]	σ_{ext} meas [µm²]	σ_{ext} calc [µm²]	error [%]
0.152 ± 0.0032	0.004 ± 0.0017	0.004 ± 0.0055	19.407
0.300 ± 0.0043	0.153 ± 0.0047	0.140 ± 0.011	9.357
0.453 ± 0.0063	0.661 ± 0.021	0.639 ± 0.020	3.443
0.596 ± 0.0077	1.287 ± 0.054	1.245 ± 0.015	3.373
0.799 ± 0.0083	1.718 ± 0.080	1.695 ± 0.070	1.357
0.1020 ± 0.011	1.481 ±0.080	1.407 ± 0.040	5.259

Table 3.5 *Measured and calculated values of σ_{ext} as found in this study.*

Diameter [µm]	σ_{ext} meas [µm²]	σ_{ext} calc [µm²]	error [%]
0.299 ± 0.006	0.158 ± 0.005	0.138	14.763
0.404 ± 0.004	0.372 ± 0.055	0.401	-7.065
0.500 ± 0.015	0.719 ± 0.046	0.763	-5.786

The 0.3 μm PSL showed an overestimation of σ_{ext} (14%) while 0.4 μm and 0.5 μm PSL showed an underestimation of σ_{ext} (7.1% and 5.8% respectively) (Figure 3-5, Figure 3-6 and Figure 3-7). Comparing measured and calculated values of σ_{ext} for all three PSL sizes (Figure 3-8) an overall accuracy of around -10% was indicated. Due to the accuracies at each individual PSL size, an overall accuracy of ±10% will be given for measurements made by the CRD. An ammonium sulfate calibration performed at the start of the FLAME2 study indicated a bias of 0.739 too low for CRD measurements, contradicting the ±10% accuracy indicated by the PSL tests.

3.3 Particle Losses

The valve mechanism, the CRD cell, and the inlet, with a 90 degree angle of entry into the cell, are all possible locations of particle losses. Particle loss tests were thus performed on the CRD measuring concentrations of monodisperse ammonium sulfate at 3 locations using two TSI model 3010 CPC's (identified as CPC1 and CPC2, Figure 3-9). To ensure that particle loss measurements were not influenced by biases in CPC measurements, the CPCs were tested for precision by sampling the same ammonium

sulfate aerosol samples. Comparison (Figure 3-10) showed precision between measurements to be 99.9%.

Ammonium sulfate aerosol was generated by atomization of a 1% solution with a constant output atomizer (TSI model 3076). Particles were dried using two silica desiccant dryers in series, sent through a neutralizer and a DMA (TSI 3080) to size select aerosols of 0.2, 0.3, 0.4 or 0.5 μm and diluted with room air to balance the flow between the CPCs and DMA. The non-conductive tubing from the cell to each CPC was cut to approximately the same length to give equivalent sampling losses. Total flow through the cell (including CPC flow rates) was 4.5 lpm with a purge flow rate of 0.025 lpm. Particle concentrations were measured for three separate configurations: at ports 1 and 2; at ports 2 and 3; and at ports 1 and 3 to determine losses through the valve, the cell and throughout the entire system, respectively (Figure 3-9). Particle number concentrations measured by CPC1 and CPC2 were averaged to 5 seconds and visually aligned to account for time delay due to the transit time between the two CPC sampling locations.

A slope of 1.006 between CPC measurements at ports 1 and 2 showed minimal particle losses in the valve mechanism; a slope of 0.998 between ports 2 and 3 showed minimal losses in the cavity. A slope of 0.967 was obtained between ports 1 and 3 giving a total system loss correction of 3% for the CRD (Figure 3-11). The same slope was found for each particle size measured, indicating there is not a size dependence of particle loss in the range 0.2 to 0.5 μm.

Theoretical particle losses were determined using Aerocalc giving minimum and maximum particle sizes measurable in the cavity, losses due to bends in tubing and Reynolds number. Aerocalc is an Excel spreadsheet set up to calculate various aerosol

properties and kinetics based on equations described by Hinds [1982] and Baron and Willeke [2001; 1993]. For particle sizes typically measured by the CRD (D_p < 1μm) and the low flow speeds in the system, particle losses through gravitational settling or by impaction are small. With a cell diameter of 0.035 m and a sample flow of 3 lpm, a Reynolds number of 33 is calculated, well within the laminar region. Losses due to gravitational settling from the inlet to outlet are computed to be about 5% for particles 1.1 μm in size, less than 1% for particles 0.500 μm. Stokes numbers calculated for this system are less than 10^{-3}, thus depositional losses are negligible. Calculated diffusional losses from the inlet to the outlet of the cell were < 1% for particles > 0.1 μm,

Measured losses in the CRD were greater than modeled losses for typical aerosol sizes (D_p <1 μm). Discrepancy between measured and calculated losses is possibly due to error in CPC number concentration measurements, leaks in the system and other losses not modeled by Aerocalc. Theoretical losses indicated that there are minimal particle losses for aerosol particles between 0.1 and 1 μm while measured losses indicate a loss of 3% for particles between 0.2 and 0.5 μm; no size dependence on loss was noted. Assuming a constant particle loss of 3% extended to 0.1 - 1 μm, the most optically and atmospherically relevant range of particle sizes, a correction of 1.03 can be applied to measured extinction coefficients. For particles smaller than 0.1 μm and larger than 1 μm, a larger correction factor is mostly likely necessary, but as particles are less optically and atmospherically relevant for these sizes, a correction of 1.03 to extinction coefficients will be applied.

3.4 Filtered air extinction coefficient measurements

Filtered air samples are a necessary part of the CRD data analysis. A requirement when using filtered air subtraction to eliminate mirror and ambient air losses is that the filtered air extinction remains constant throughout the entire sample period. If the value of the filtered air extinction changes during a measurement it can cause error in the subsequent aerosol extinction coefficient. Filtered air measurements can be influenced by environmental changes (pressure, temperature and relative humidity), gas extinction, particle leaks, mirror cleanliness and drift in mirror alignment. At 532 nm there are a limited number of gasses which cause measurable extinction. Those with the largest absorption cross sections are NO_2 and O_3, with absorption cross sections of 4.84×10^{-19} cm^2/molec (1.19 Mm^{-1}/ppb at STP) and 1.09×10^{-22} cm^2/molec (0.00027 Mm^{-1}/ppb at STP) respectively [*Baynard et al.*, 2007]. CO_2 with scattering cross section of 34 Mm^{-1} at STP [*Anderson et al.*, 1996], air (Rayleigh) with a scattering cross section of 13.70 Mm^{-1} at STP [*Bucholtz*, 1995], and water vapor [*Garland et al.*, 2007] have the largest scattering contributions at 532 nm. If concentrations of these gasses remain constant throughout a measurement, their contribution to extinction during an experiment can be accounted for by subtraction of the filtered air extinction.

To test the stability of CRD filtered air measurements the extinction coefficient for filtered air was measured overnight, removing or monitoring the interferences listed above (Figure 3-12). Contributions to filtered air extinction measurements from gasses are difficult to monitor or control, therefore only contributions from environmental parameters, mirror alignment or mirror cleanliness changes were monitored. Because NO_2 has the largest influence on extinction and would cause the largest variability, a

filter which eliminates NO_2 was placed upstream of the inlet to eliminate any NO_2 in the room air. Dramatically changing RH could also have a large impact on the extinction measurements and consequently a desiccant drier was also placed upstream of the inlet. Temperature, RH, pressure and sample flow through the cell were monitored to determine if they were correlated with extinction measurements. To monitor possible particle leaks through the filter and into the cavity, CPCs (TSI model 3776 and 3010) measured particle number concentration before and after the cavity. The CRD was run with a sample flow of 3 slpm and a purge flow of 0.025 slpm and the data were averaged to a 5 second time scale.

During the sample period, there was some variation in temperature, pressure and RH measurements ($T = 294 \pm 0.11$ K, $P = 0.777 \pm 0.0008$ bar, $RH = 27.67 \pm 0.97$ %) although there was no strong correlation between the measured extinction coefficient and temperature, pressure or relative humidity. This indicates that measured variations in the extinction coefficient measurement of filtered air were not due to environmental parameters. No noticeable particle leaks were detected by the CPCs during the measurement, indicating variability in the CRD measurement was not due to particles leaking into the system.

The magnitude of the extinction measurement was high for this experiment due to dirty mirrors and poor alignment. The extinction measurement varied from 836 Mm^{-1} to 865 Mm^{-1} with an average measurement of 851 Mm^{-1}. The standard deviation of the measurements was 3.89 Mm^{-1}, 0.5% of the total measurement, indicating in reality small variability in extinction measurement.

This test demonstrated that the filtered air extinction coefficient measurement variability due to environmental parameters, mirror cleanliness and mirror alignment drift was negligible. Because water, or greatly changing RH, would cause significant variability in extinction measurements, unless specifically monitoring the RH influence on extinction, samples should be dried before measurement. Drift in filtered air extinction coefficient that occurs will most likely be due to changes in gas concentrations. To account for this possible drift, filtered air extinction measurements should be taken before and after each sample measurement or periodically during a measurement if the sample period is long or dramatic changes are occurring to the aerosol sample.

3.5 Measurement uncertainties

Measurement uncertainty in the CRD can easily be determined due to the fast sampling rate of the instrument. The residence time of the cavity was determined to be between 4 and 9 seconds for flow rates 3 to 6 slpm and the volume of the CRD. Data are sampled at a rate of 6 data points per second where each data point is an average of 10 measurements; the data output gives an average extinction coefficient b_{6Hzave} and standard deviation of the extinction coefficients Δb_{6Hzave} (see *2.2 Extinction cell specifics*). Because the residence time in the cell is much greater than the sampling rate, the data output can be averaged to a 1 second time interval during which the aerosol sample can be assumed to be constant.

Taking into consideration the output standard deviations, the standard deviation for a 1 second average is found using

$$\Delta b_{1\,\mathrm{sec}\ ave} = \sqrt{\frac{\sum_{i=1}^{6}(n_i - 1)\Delta b_{6\,Hzave\ i}^{2}}{\sum_{i=1}^{6}(n_i - 1)}} \qquad 3\text{-}4$$

Where n_i is the number of samples that were used to calculate the data output standard deviation $\Delta b_{6Hzavei}$; in this case $n_i = 10$. Equation 3.4 can be simplified

$$\Delta b_{1\,\mathrm{sec}\ ave} = \sqrt{\frac{(n - 1)\sum_{i\ 1}^{6}\Delta b_{6\,Hzave\ i}^{2}}{(n - 1)6}} = \sqrt{\frac{\sum_{i=1}^{6}\Delta b_{6\,Hzave\ i}^{2}}{6}} \qquad 3\text{-}5$$

The value, $\Delta b_{1secave}$, is then used to determine the measurement uncertainty in the extinction measurement. If the data are averaged further, the uncertainty in the measurements can be calculated using

$$\%\ variation = \frac{\Delta b_{1\,\mathrm{sec}\,ave}}{b_{1\,\mathrm{sec}\,ave}} \qquad 3\text{-}6$$

where $b_{1secave}$ is the one second average value of the extinction coefficient. If the sample extinction does not rapidly change, the percent variance of the sample also does not vary significantly indicating the validity of longer average times. The percent variance was calculated for a sample measurement during the FLAME2 study and was found to be relatively constant during the sample period (Figure 3-13). Thus for samples where the extinction coefficient does not dramatically vary, the average percent variation of the sample can be assumed as a representative uncertainty for the average extinction measurement for time averages longer than 1 second.

3.6 Multi-exponential decay

Cavity ring-down spectroscopy derives extinction coefficients by fitting the exponential decay of light detected by a photo multiplier tube (PMT), photodiode, or

other photodetector located on one side of the sample cavity. It is possible that non-linear PMT response, electronic noise in the system, or multiple spatial modes in the cavity will cause voltage decays, $\tau_{noise,}$ which in turn influence the exponential decay, τ_{sample}, measured by the PMT causing a multi-exponential decay [*Baynard et al.*, 2007; *Thompson et al.*, 2002]. Typically the timescales for these other decays are thought to be much shorter than the timescale of the decay caused by the sample extinction and thus the first few microseconds of the signal are omitted from the signal analysis to remove the influence of the noise [*Thompson et al.*, 2002; *Thompson et al.*, 2003]. If the effects of τ_{noise} are not removed from the signal, a single-exponential fit of the entire decay signal will yield a $\tau_{fit} \neq \tau_{sample}$.

A good indicator of whether there is contamination to the sample decay causing a multi-exponential decay is the residual of the fit to the signal decay. When there is contamination causing decay, the residual between the signal decay and fit will demonstrate oscillation around 0, described as non-random curvature. In the case of the instrument described by Baynard [2007] the residual of the PMT signal was determined to have no non-random curvature (Figure 3-14) indicating no bias due to multi-exponential decay. An instrument described in 2001 by Smith and Atkinson [2001] is able to measure the ring-down for both visible (532 nm) and near-infrared (1064 nm) wavelengths and uses a PMT to measure the signal for the visible and a photodiode for the near-infrared. The authors report a very good fit of the PMT signal for the visible decay with a relatively flat residual of the fit (Figure 3-15) while the decay for the near-infrared light shows non-random curvature to the residual of the photodector signal fit (Figure 3-16). Smith and Atkinson attributed the curvature of the residual to multi-

exponential decay caused by bandwidth effects in the transimpedance amplifier of the InGaAs photodiode used to analyze the near-infrared decay [*Smith and Atkinson*, 2001].

For our system, we attempted to eliminate error due to noise with short time scales by eliminating the first 10 data points, corresponding to approximately the first 2 μs of the signal decay. During the FLAME2 campaign, the fit residual often demonstrated non-random curvature (Figure 3-17 represents a screen shot of the residual plotted by the analysis program but not saved) indicating signal contamination. From this figure it is evident that eliminating the first 2 μs of the signal would be insufficient to remove the contamination. Because of the large amount of data that is obtained (the signal decay is sampled by the PMT at a rate of 5 MHz, and 60 decays are fit each second) only the values of the fitted ring-down time, τ_{fit}, are recorded; we have no data records of the signal decay or of the fit residuals. Unfortunately, this means that there is no way to re-analyze the signal decays measured during FLAME2 and during laboratory PSL tests to determine the magnitude of error caused by signal contamination.

It is likely that extinction coefficients reported by the CRD from FLAME2 and the PSL laboratory tests are biased because of signal contamination and this bias cannot be determined or removed from the measurements.

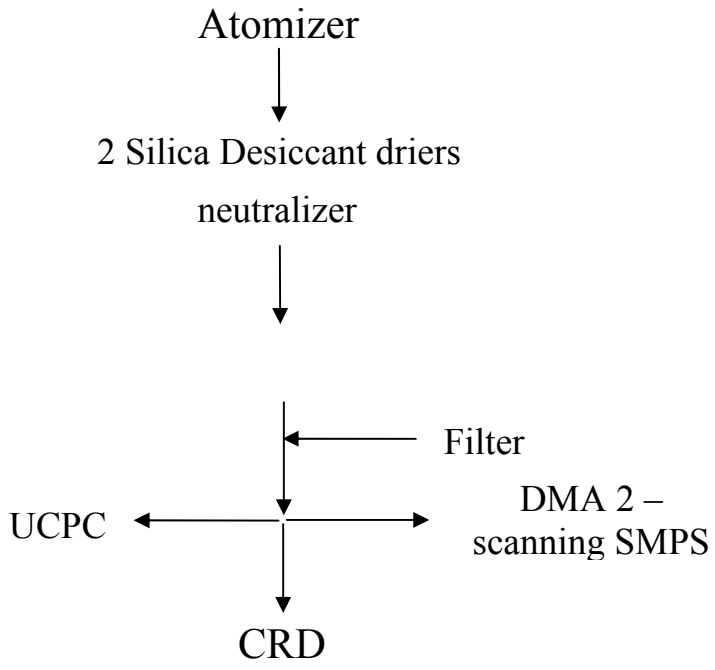

Figure 3-1 *Instrumental setup for the PSL studies*

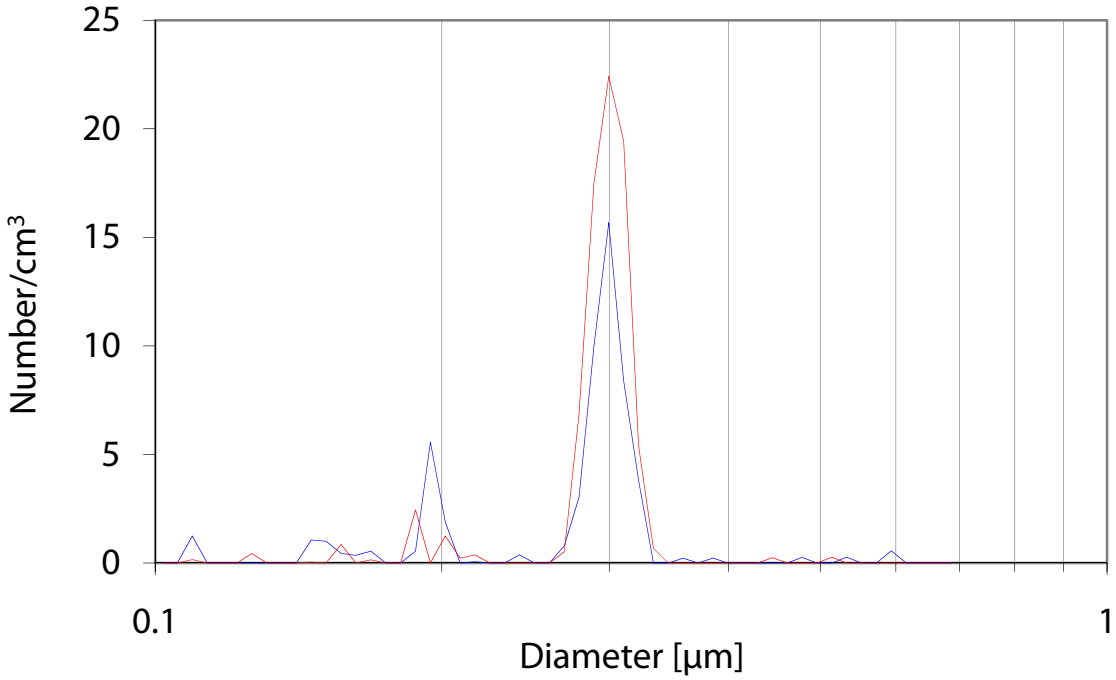

Figure 3-2 *Sample size distributions for 0.3 µm particles. The peak occurs at the manufacturer's stated diameter.*

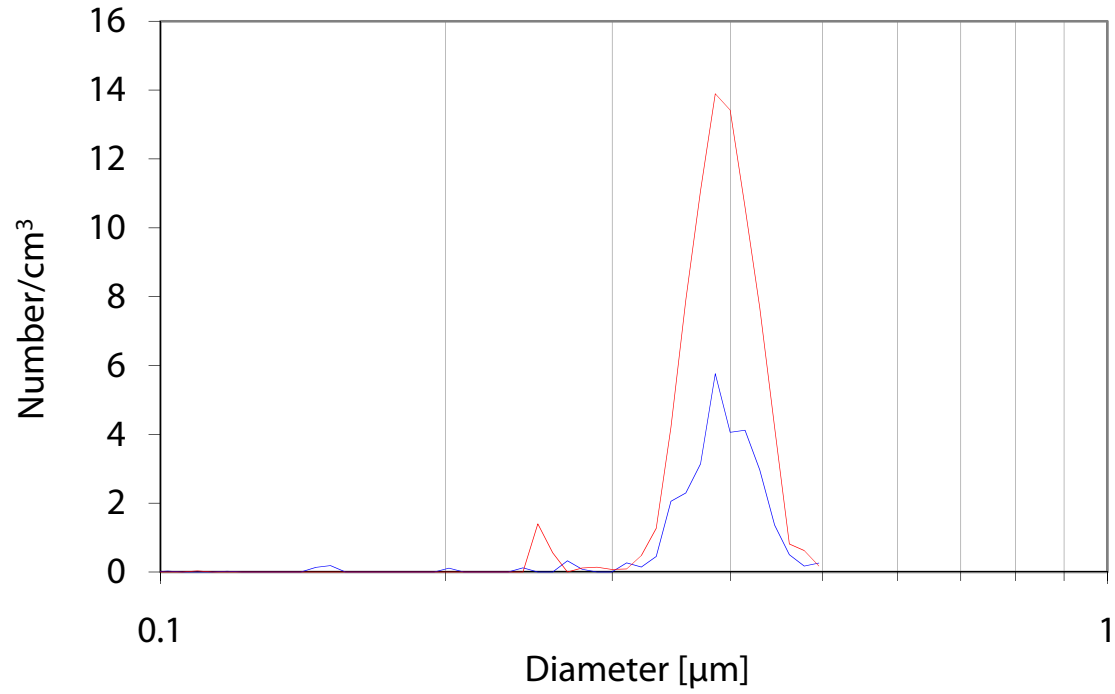

Figure 3-3 *Sample size distributions for 0.4 µm particle. The peak occurs at the manufacturer's stated diameter.*

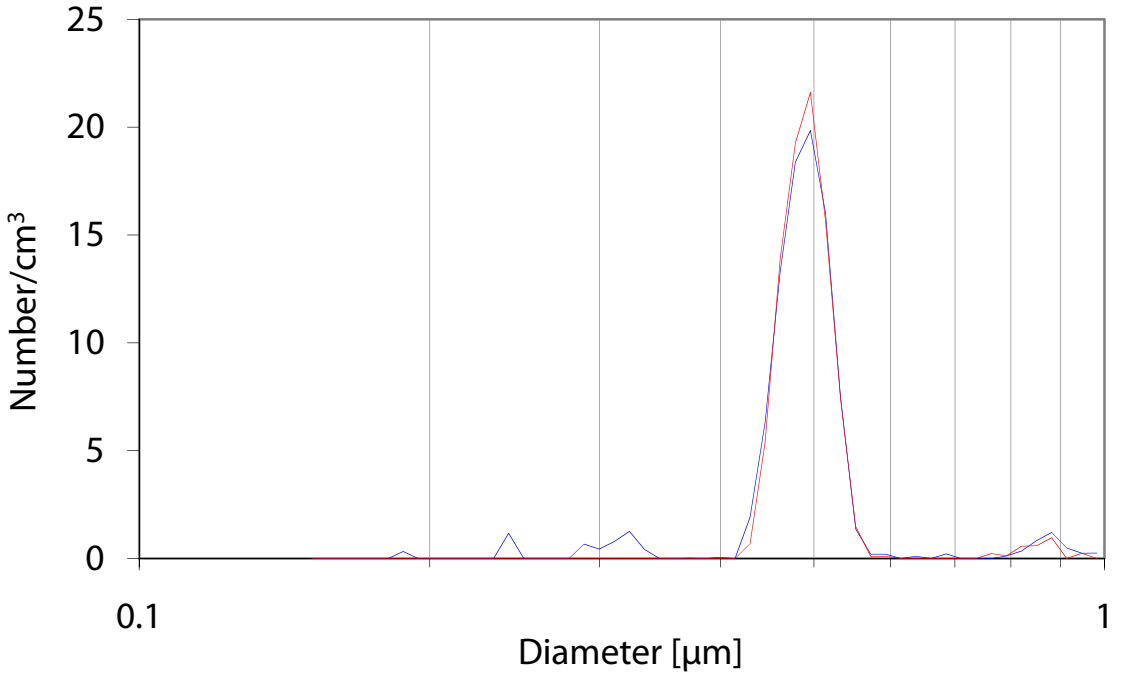

Figure 3-4 *Sample size distributions for 0.5 µm particles. The peak occurs at the manufacturer's stated diameter.*

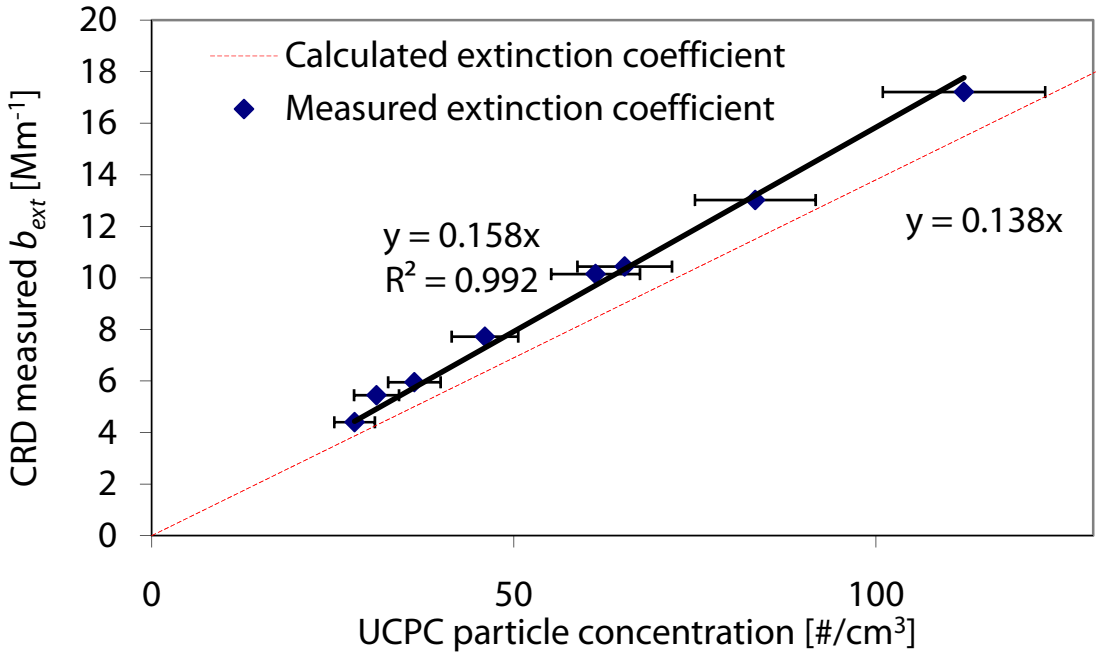

Figure 3-5 *Comparison of measured particle concentrations (x-axis) and measured b_{ext} (y-axis) for 0.3 µm PSL particles. The slope indicates the measured optical cross section σ_{ext}meas,[µm^2], red dashed line indicates calculated cross section, σ_{ext}calc. Comparison of the calculated and measured cross sections yields a 14.7% error.*

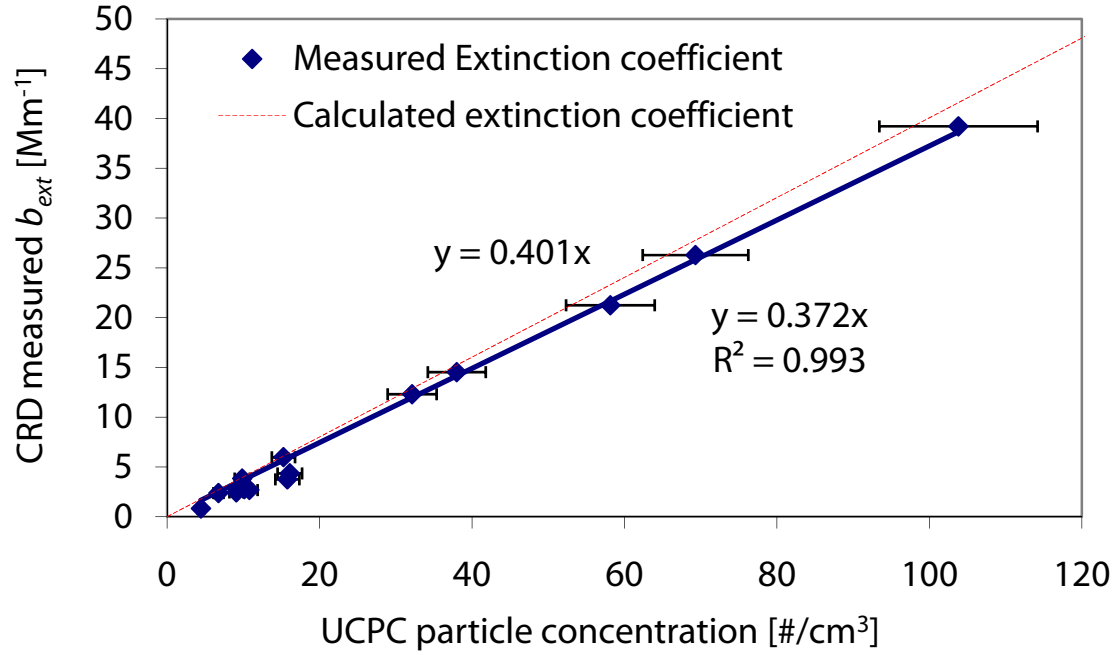

Figure 3-6 *Comparison of measured particle concentrations (x-axis) and measured b_{ext} (y-axis) for 0.4 µm PSL particles. The slope indicates the measured optical cross section σ_{ext}meas,[µm^2], red dashed line indicates calculated cross section, σ_{ext}calc. Comparison of the calculated and measured cross sections yields a 7.1% error.*

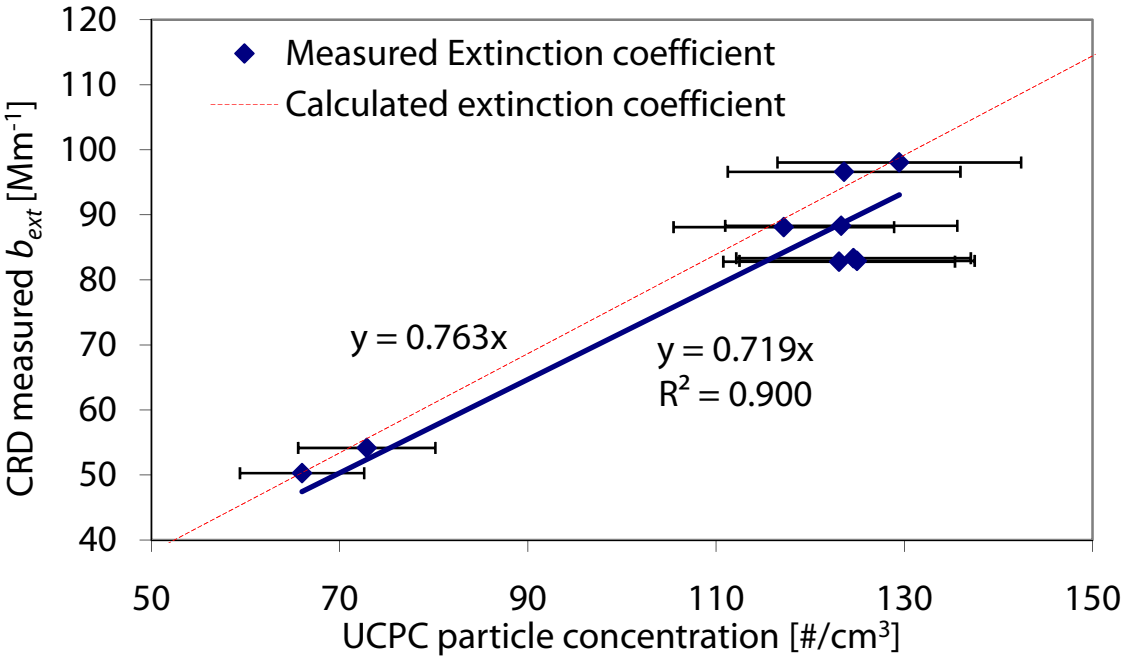

Figure 3-7 *Comparison of measured particle concentrations (x-axis) and measured b_{ext} (y-axis) for 0.5 µm PSL particles. The slope indicates the measured optical cross section σ_{ext}meas,[µm^2], red dashed line indicates calculated cross section, σ_{ext}calc. Comparison of the calculated and measured cross sections yields a 5.8% error.*

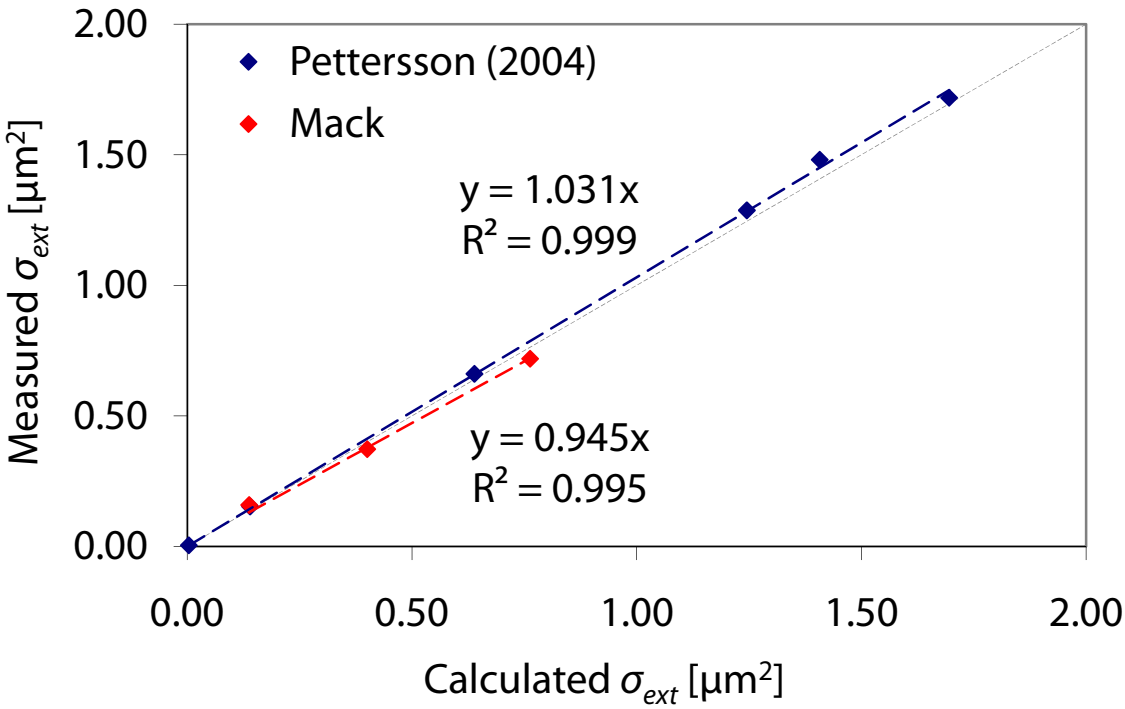

Figure 3-8 *Comparison of calculated extinction cross section and measured extinction cross section for values reported by Pettersson et al [2004] and for this study. Values reported by Pettersson indicated a total accuracy <5% while the CSU CRD indicated an overall accuracy of <10%.*

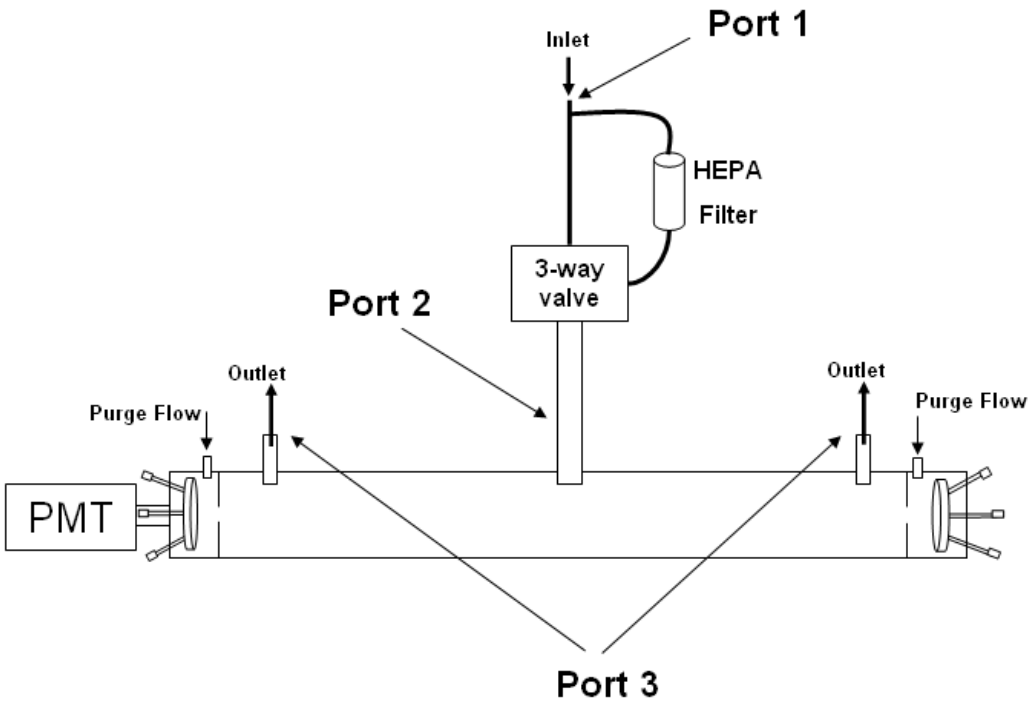

Figure 3-9 *Diagram of particle loss tests and air flow in Cavity Ring Down. Particle losses were determined between port 1 & 2, port 2 & 3 and port 1 & 3. When measuring from port 3, both outlets were measured simultaneously. Solid arrows indicate direction of air flow.*

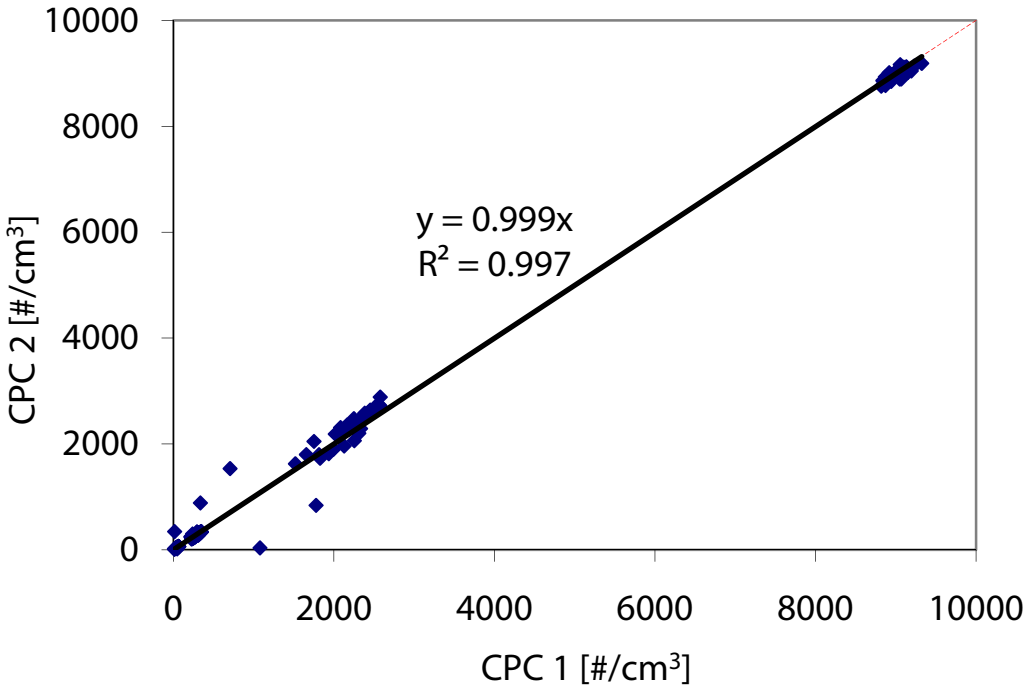

Figure 3-10 *Precision between CPC1 and CPC2 for ammonium sulfate aerosol.*

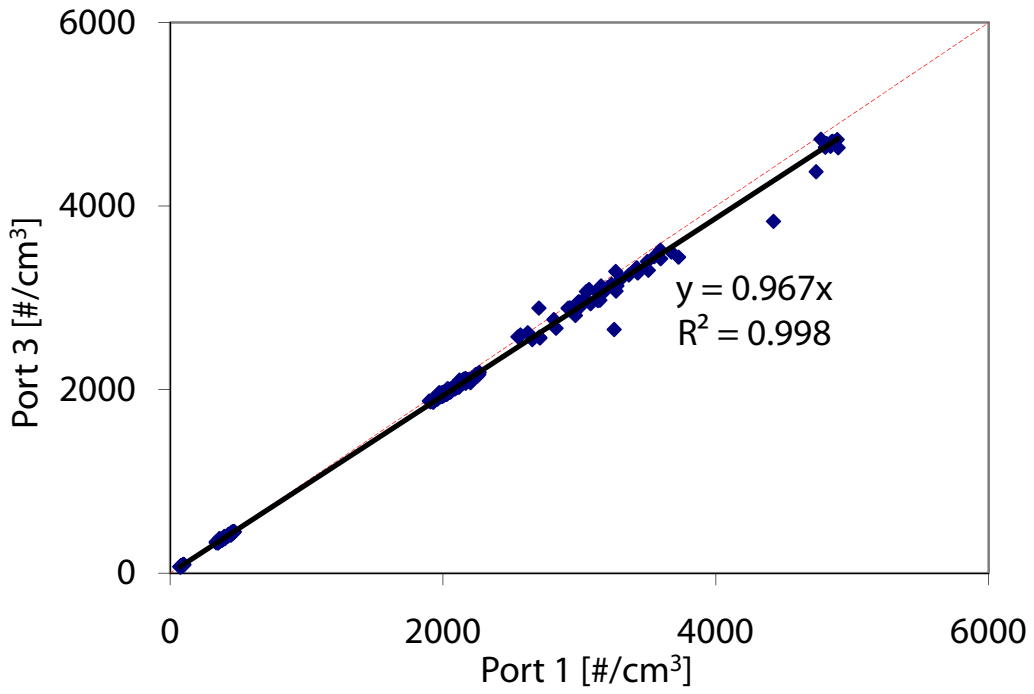

Figure 3-11 *Particle concentrations measured at port 3 (outlet) compared to those measured at port 1 (inlet) for particles 0.2 – 0.5 µm. The slope indicates penetration efficiency.*

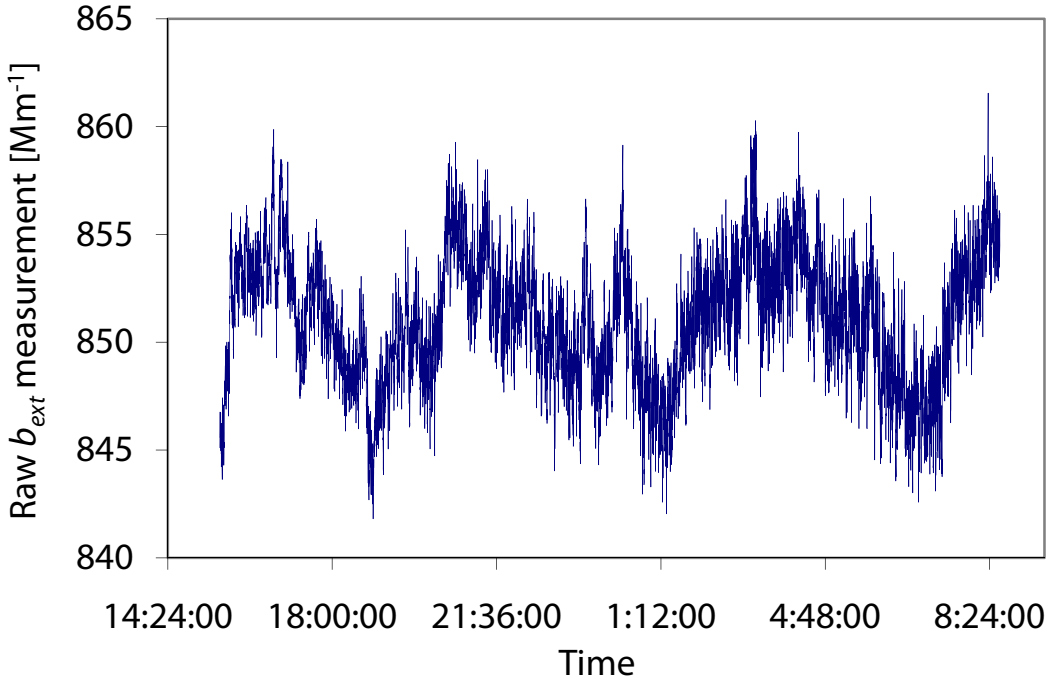

Figure 3-12 *Filtered air extinction measurements taken overnight on 12-07-07. An NO_2 filter was placed upstream of inlet. Extinction coefficients have such a large magnitude because of the poor mirror alignment of the CRD at the time of measurement.*

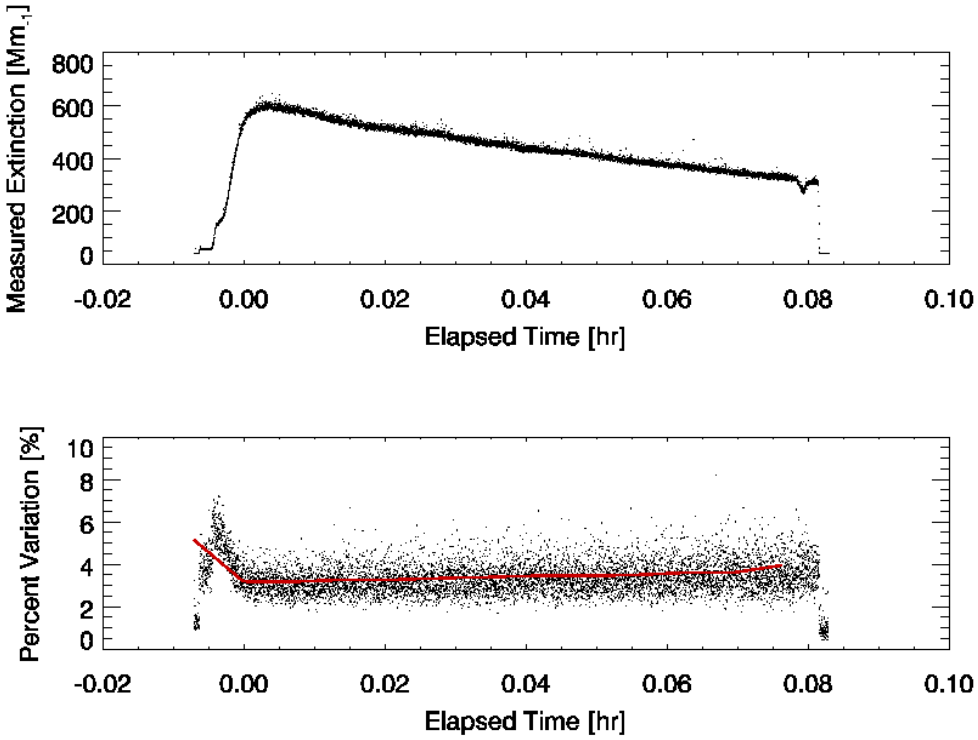

Figure 3-13 *Sample extinction measurement from FLAME2. The top plot is an example of 1 sec averages of measured CRD extinction. The bottom plot indicates the percent variance for the sample, while the red line indicates 10 minute averages of the percent variance.*

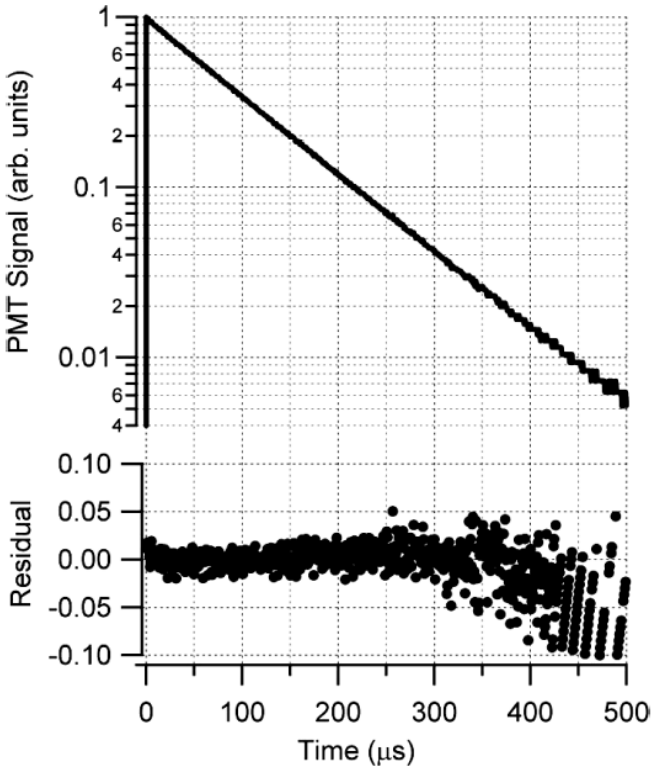

Figure 3-14*Example PMT signal and fit residual from [Baynard et al., 2007], with no systematic curvature of the residual indicating no significant bias from multi-exponential decays.*

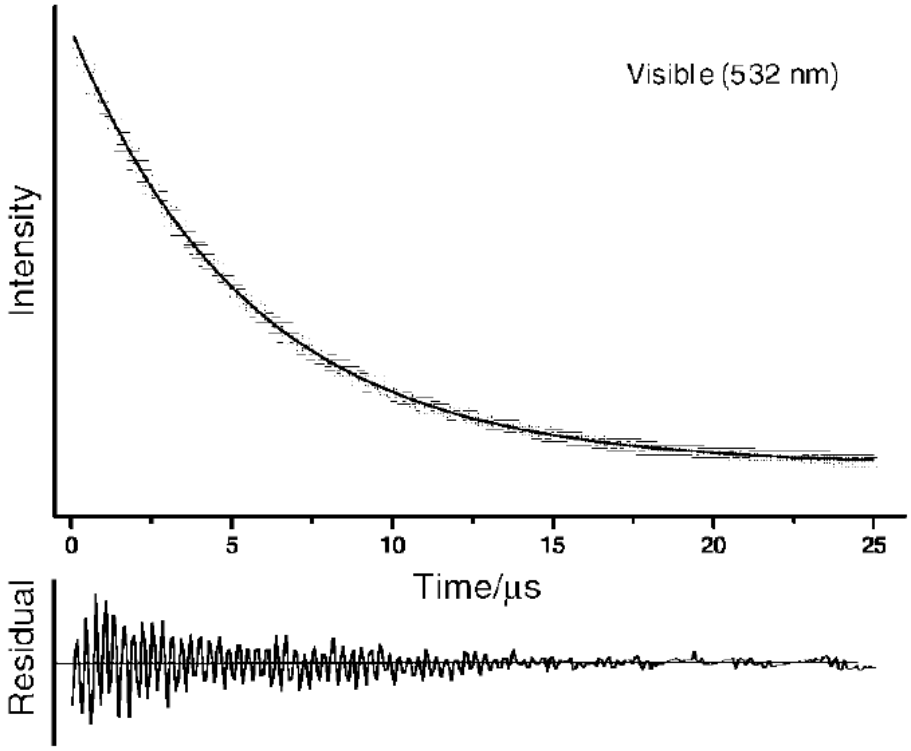

Figure 3-15 *Example PMT signal, fit and residual from [Smith and Atkinson, 2001] for the visible (532 nm) decays with no non-random curvature.*

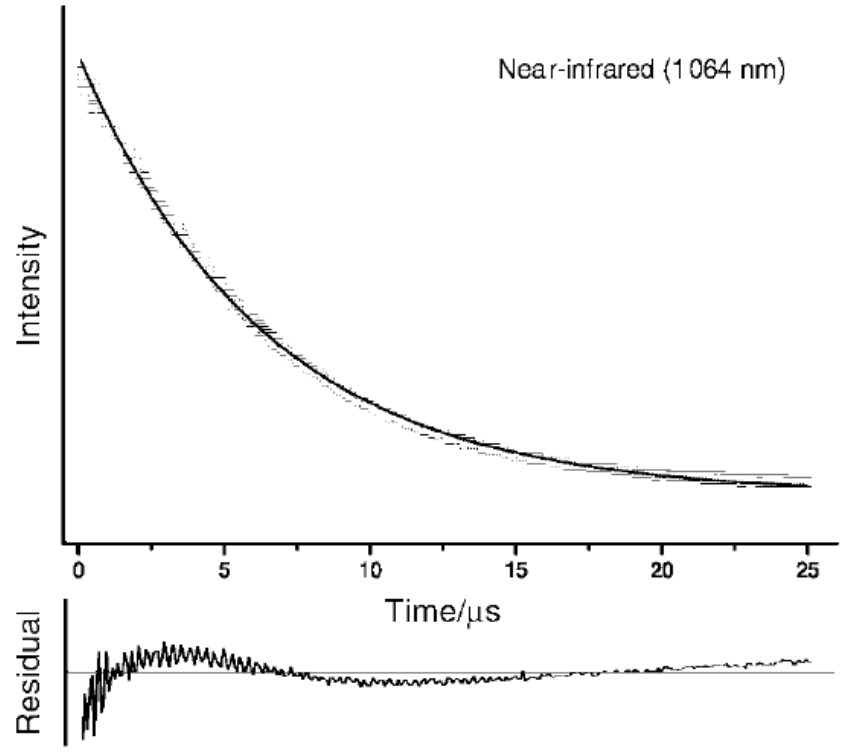

Figure 3-16 *Example PMT signal, fit and residual from [Smith and Atkinson, 2001] for the near-infrared (1064 nm) ring-down decays having non-random curvature in the residual similar to what is observed with the CSU CRD.*

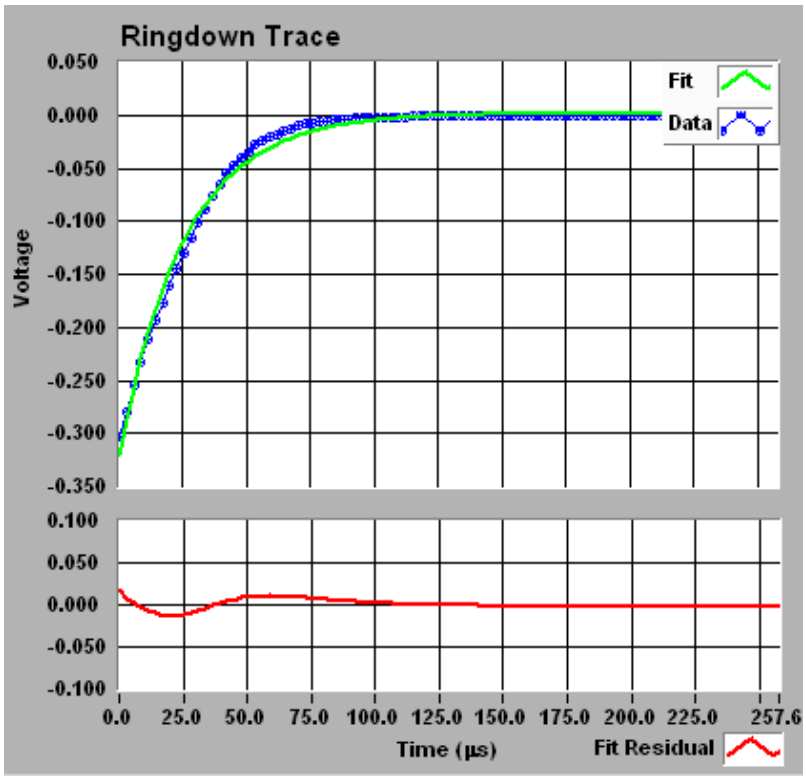

Figure 3-17 *Example of CSU CRD signal, fit to the signal and residual of the fit as shown in the data acquisition program. In this example the curvature of the fit residual, as well as the noticeable discrepancy between the data and fit indicate the presence of signal contamination by multiple exponential decays.*

Chapter 4 FLAME2

4.1 Introduction

The Fire Laboratory at Missoula Experiment 2 (FLAME2) study was conducted at the U.S. Forest Service Fire Science Lab (FSL) in Missoula, Montana from May 20 - June 6, 2007. FLAME2 followed work done during the summer 2006 FLAME1 study to examine properties of emissions from biomass burning. The optical closure portion of the FLAME2 experiment examined the optical properties, SSA and complex refractive index of biomass smoke. Instrumentation used included the CSU CRD extinction cell, FSL TSI nephelometer, photoacoustic spectroscopy (PAS) instrument from the Desert Research Institute (DRI) and the CSU sizing rack.

4.2 Description of experiment

This work focuses on the chamber portion of FLAME2 study during which a fuel was ignited in the large combustion chamber at the FSL (12.5 x 12.5 x 19.5 m) and the smoke was allowed to fill the entire chamber. Emissions were sampled by a 55 gallon drum and a sample line went from the drum to a smaller manifold in an adjacent room from which each instrument in the optical closure study sampled (Figure 4-1). Since flow rates and tubing inner diameters varied among the various instruments, the tubing length to each instrument from the manifold was adjusted to give similar residence times in the sample lines and thus similar gravitational and diffusional losses. The aerosol

sample had a relative humidity of <35% (Table 4.1) by the time it reached the instruments.

The chamber portion of FLAME2 consisted of 21 separate burns; burn names, fuel information and ambient meteorological conditions are listed in Table 4.1. After the fuel was ignited and emissions were typically sampled for about two hours before the chamber was diluted with clean outside air and prepared for the next burn. Three burns were sampled longer than two hours (burns 119, 129 and 130). For burn 129 and 130, the initial aerosol concentrations were large and the sample was diluted twice by adding outside air to the large combustion chamber and then sampling for an hour at each concentration level. Burns 119 and 130 (a dilution burn) were also sampled overnight.

4.3 Fuel types

Fuel types for the FLAME2 campaign were chosen to represent fuels commonly burned in the United States during wild and prescribed fires. Fuels were also chosen to represent the various vegetation types which would burn during these fires: trees, grasses and shrubs. Two fuels were also burned which represent fuels commonly burned in Asia. The list of fuels burned during the chamber portion of the study, corresponding burn IDs and other fuel and chamber information are listed in Table 4.1. A more complete description of each burn can be found in [*McMeeking*, 2008].

Table 4.1 *Identification number, fuel information and local ambient pressure, temperature and RH during the FLAME2 chamber burns as well as RH measured by the PAS. A sample length time of "Ov" indicates an overnight burn.*

Burn	Fuel	Vegetation type	Source	Date	Sample length [hr]	Fuel Weight (g)	Ash (g)	Moisture Content [%]	Temperature [C]	Pressure [mb]	Ambient RH [%]	PAS RH [%]
113	LLP / wire grass	trees / grass	MS	30-May-07	2.25	150	36.0	5.61	14.47	910.16	50.00	20.58
114	black needlerush	grass	FL	30-May-07	1.98	150	12.7	5.64	19.73	908.38	34.25	18.79
115	oak and hickory	trees	NC	30-May-07	2.10	101	7.8	7.44	23.90	906.32	17.33	16.88
116	fresh fir	tree	MT	31-May-07	2.14	100	4.3	4.52	16.30	906.32	41.67	18.53
117	dry fir	tree	MT	31-May-07	1.75	100	17.4	12.11	22.03	905.08	28.67	19.40
118	palmetto	SE shrub	FL	31-May-07	2.00	105	14.0	5.62	26.33	903.27	18.33	17.97
119	palmetto	SE shrub	MS	31-May-07	Ov	105	17.5	5.47	11.50	902.37	36.38	17.30
120	rice straw	Asian fuel	Taiwan	1-Jun-07	2.00	100	20.4	8.30	16.27	904.74	48.67	20.73
121	duff	duff	AK	1-Jun-07	2.00	86.6	28.6	9.74	23.87	903.05	34.67	21.78
122	rhododendron	SE shrub	NC	1-Jun-07	2.00	100	5.2	10.62	29.27	901.58	21.33	22.66
123	black spruce	tree	AK	1-Jun-07	1.99	101	38.5	5.02	29.03	900.59	19.25	19.53
124	dry fir	tree	MT	4-Jun-07	1.49	50	26.5	14.15	21.30	905.19	50.00	27.11
125	duff	duff	AK	4-Jun-07	1.49	40	20.6	12.16	27.60	903.38	31.33	25.25
126	wiregrass	grass	FL	4-Jun-07	1.50	50	5.3	7.80	30.37	901.47	22.67	23.08
127	chamise	desert shrub	CA	4-Jun-07	1.49	100	4.6	5.52	28.77	898.76	26.67	21.12
128	black needlerush	grass	FL	4-Jun-07	2.00	50.0	4.5	7.27	19.27	902.76	67.50	19.50
129	sage	desert shrub	MT	5-Jun-07	3.83	250	16.0	7.82	18.23	893.06	69.00	31.49
130	LLP	tree	MS	5-Jun-07	Ov	250	135.0	8.92	11.73	891.20	69.70	28.91
131	gallberry	SE shrub	MS	6-Jun-07	1.50	50	5.3	4.54	9.47	891.08	73.33	23.30
132	sugarcane	Asian fuel	China	6-Jun-07	1.50	50	4.0	9.44	8.40	891.76	83.00	19.66
133	white spruce	tree	AK	6-Jun-07	1.50	50	13.1	38.30	7.70	893.23	81.00	19.65

4.4 Cavity Ring Down – extinction coefficient

The CRD extinction cell used in this study is described in more detail in previous chapters. For this study a flow rate of 6 slpm and purge flow of 0.05 lpm were used; the ratio between flow rate and purge flow was consistent between FLAME2 and subsequent laboratory studies described in Chapter 3. Filtered air extinction coefficients were measured before and after each burn except during dilution burns, where they were additionally taken while the sample was diluted.

Over the entire study, the mean value of filtered air extinction coefficient was $b_{filt\_ave} = 55.16 \pm 1.16$ Mm^{-1}. The small variation in the filtered air extinction coefficient during the study indicates minimal contamination of the mirrors due to particles and minimal changes in alignment of the mirrors. Because filtered air extinction measurements were taken before and after each burn, a linear relationship with time for the filtered air extinction measurement was assumed during the burn; that is, any changes in extinction due to changing gas concentrations or mirror contamination were assumed to be linear. For various reasons, for two of the burns, filtered air extinction measurements were only available either before or after the burn, but not at both times (burns 127 and 128). For these burns the average of the filtered air extinction coefficients available was used.

The CRD derived extinction coefficients were multiplied by a factor of 1.47 which accounted for corrections due to particle loss in the CRD, purge flow and the ammonium sulfate calibration, described in section *4.8 Ammonium Sulfate Calibration*. Data were output by the CRD at a rate of 6 samples per second and were averaged to a 1 second timescale to calculate measurement uncertainty according to *3.5 Measurement*

uncertainties. The data were then averaged to the same 10 minute time scale as the measured size distributions. Because data are averaged to a 10 minute time scale, uncertainty in extinction measurement was reported as the average percent variance of the 10 minute sample. Rapidly changing extinction coefficients were excluded by eliminating measurements where the percent variance was greater than 10%. Uncertainty during the FLAME2 study varied from 2 – 6 % and was relatively constant during each burn (Figure 4-2).

Biomass burning can produce significant amounts of NO_2. At 532 nm NO_2 is the most significant gas absorber causing 1.19 Mm^{-1}/ppb at STP. During FLAME2, the instrument measuring NO_2 did not accurately work making it impossible to determine the amount of measured extinction cause by NO_2 absorption. During FLAME1, there were accurate measurements of NO_2. In general NO_2 concentrations were between 10-40 ppb, with most in the 10-20 ppb range and decreased slowly over the course of the burn. An NO_2 concentration of 20 ppb will then lead to an absorption coefficient of 23.8 Mm^{-1}, which would lead to an error of approximately 10% for an absorption coefficient of 200 Mm^{-1}.

The ±10% accuracy determined by the PSL tests was not applicable to the FLAME2 CRD measurements due to the large correction factor indicated by the ammonium sulfate calibration. All data are reported at ambient temperature and pressure.

4.5 TSI Nephelometer – scattering coefficient

A three wavelength nephelometer (TSI model 3563) from the FSL measuring at wavelengths of 450, 550 and 700 nm, was used to measure scattering coefficients for this study (Figure 4-3). Gas calibrations were performed before and after the FLAME2 study

and the nephelometer data were corrected according to the calibration at the end of the study. The calibrations were performed using calculated and measured values of scattering coefficient for SUVA (HCF-134a), CO_2 and filtered air. The calculated values of scattering coefficient used were 88.02 Mm^{-1}, 22.14 Mm^{-1} and 0 Mm^{-1} for SUVA, CO_2 and filtered air at STP and λ = 532 nm. During calibrations, Rayleigh scattering, or the signal due to filtered air, was subtracted from the sample scattering coefficient (i.e. the instrument was calibrated such that Rayleigh scattering = 0 Mm^{-1} and the reported scattering coefficient represents only that of the aerosol). The nephelometer calibration at the end of the study yielded a correction of 1/0.085 = 0.922 (Figure 4-4) which was applied to the TSI nephelometer data.

Uncertainties caused by angular nonidealities of the TSI nephelometer are a recognized source of error in the scattering measurement and have been well modeled. The angular scattering of light by aerosol particles is dependent on the particle size and refractive index of the aerosol sample. Due to the geometry of the TSI nephelometer, light scattered from 0˚ to 7˚ and 170˚ to 180˚ is unseen by the detector [*Anderson et al.*, 1996; *Anderson and Ogren*, 1998]; this is known as angular truncation. Errors in the nephelometer measured scattering coefficient also arise due to the slightly nonlambertian light source; the light intensity in the sampling chamber depends on angle. Nonlambertian errors dominate for submicron particles while error due to truncation dominates for super micron particles [*Anderson and Ogren*, 1998]. Assuming aerosols sampled during the study are primarily submicron, or have a geometric volume mean diameter < 1 μm, a correction developed by Anderson and Ogren can be applied to the raw nephelometer data. The correction was developed assuming bimodal lognormal size

distributions of homogenous spherical particles with a range of geometric volume mean diameters and refractive indices [*Anderson and Ogren*, 1998]. For each nephelometer wavelength, the correction *C* is found by

$$C = a + b\text{Å}^{b} \tag{4-1}$$

where a and b are constants reported by [*Anderson and Ogren*, 1998] and *Å* is the Ångstrom exponent between two of the nephelometer wavelengths.

$$\text{Å} = -\frac{\log(\sigma_{\lambda 1} / \sigma_{\lambda 2})}{\log(\lambda_1 / \lambda_2)} \tag{4-2}$$

For the assumed submicron aerosol distributions, this correction, *C*, is on average 1.094, 1.076, and 1.049 for wavelengths 450nm, 550nm, and 700nm respectively.

Knowing the response function of the nephelometer due to the angular non-idealities, it is possible for known size distributions and refractive indices to exactly account for angular nonidealities in the nephelometer measurements (see *Appendix A: Mie code and correction for TSI nephelometer* angular non-idealities). For this study, the refractive index of the measured aerosol is unknown so it is necessary to use the approximate correction from Anderson and Ogren for angular nonidealities, recognizing that the actual particle size distribution and refractive index might not be in the range assumed for the correction.

An estimate of the TSI nephelometer scattering coefficient at the common instrument wavelength of 532 nm was obtained using the Ångstrom exponent between values scattering coefficient at 450 and 550 nm corrected for angular non-idealities.

$$Å = \frac{\log(b_{scat\_450nm} / b_{scat\_550nm})}{\log(\lambda_{450nm} / \lambda_{550nm})} \quad 4\text{-}3$$

For submicron particles the TSI nephelometer has been shown to have negligible particle loss and uncertainty of the nephelometer was shown to be ±1% [*Anderson and Ogren*, 1998]. Accuracy of the TSI nephelometer was determined to be at most 10% [*Anderson et al.*, 1996]. Nephelometer data, obtained at a frequency of one sample every two seconds, were averaged to the same time scale as the size distributions, 10 minutes. All data are reported at ambient temperature and pressure. Each subsequent mention of the TSI nephelometer data indicates data interpolated to 532 nm using the Ångstrom exponent and corrected for the gas calibration at the end of the study.

4.6 Photoacoustic – absorption coefficient

A photoacoustic spectroscopy (PAS) instrument constructed and operated by Pat Arnott of the Desert Research Institute [*Arnott et al.*, 1999; *Arnott et al.*, 2000] was used in this study to measure absorption coefficients (Figure 4-5). The PAS used in this study operates at a wavelength of 532 nm, consistent with the CRD.

The PAS is calibrated using the principle of the Beer Lambert Law to measure the decrease in laser power caused by a sample:

$$\frac{I}{I_0} = \exp\left(-b_{ext} L\right) \quad 4\text{-}4$$

where I_0 is the initial laser intensity, I the final laser intensity, L the length occupied by the sample and b_{ext} the extinction coefficient of the aerosol being sampled. A photo detector in the PAS measures the light intensity of the laser when no sample is present, I_0, then measures the intensity of the laser when a sample is present, I. Using the sample

path length of the instrument, the extinction due to the sample, b_{ext}, can be calculated. This is the same basic principle upon which the CRD operates but due to the short path length of the PAS, extinction coefficients must be very large for a measurable decrease in laser intensity [*Lewis*, 2007].

The PAS is capable of measuring the scattering coefficient using the principle of reciprocal nephelometry as described by Lewis [2007]. Reciprocal nephelometer measurements are calibrated assuming a linear relationship between scattering coefficient and instrument response, requiring a calibration slope and offset. The offset of the scattering calibration is determined by measurement of a particle-free sample, setting the scattering coefficient equal to 0 Mm^{-1}. The calibration slope is determined using measurements made of common table salt dissolved in water, aerosolized by a nebulizer and dried. Assuming that the salt has negligible absorption, extinction coefficients calculated using the Beer Lambert law, eq. 4.4, are compared to scattering measurements and a calibration slope is found. For calibration of the reciprocal nephelometer, extinction and scattering coefficients on the order of 100,000 Mm^{-1} are used [*Lewis*, 2007], introducing increased possibility of measurement uncertainty at low extinction and scattering coefficients.

Absorption coefficients measured by the PAS are calibrated using kerosene soot, producing particles that cause both absorption and scattering. After scattering coefficient measurements were calibrated using table salt, known absorption coefficients can be found by subtracting scattering coefficient measurements from extinction coefficient measurements. Comparing absorption coefficients calculated using photoacoustic theory to those found from the extinction and scattering coefficient measurements, a calibration

correction for the photoacoustic absorption coefficient measurements can be found. Extinction, scattering and absorption coefficients are on the order of 100,000 Mm^{-1} during calibration of the absorption coefficient [*Lewis*, 2007].

In preparation for the FLAME2 study, the 532 nm photoacoustic was calibrated using table salt to calibrate the reciprocal nephelometer and subsequent measurements of kerosene smoke to calibrate absorption coefficient measurements (from personal correspondence with Kristin Lewis, April 2008).

Absorption caused by NO_2 will also lead to error for the PAS. As mentioned before, we do not have accurate NO_2 measurements from FLAME2 and thus do not know the magnitude that NO_2 absorption contributes to the measured absorption coefficients.

The PAS data, obtained at a frequency of one sample every two minutes, were averaged to the same time scale as the size distributions, 10 minutes. Uncertainty in the absorption measurements of the PAS result from uncertainties in the variables required for calculation of the absorption coefficient; a 5% uncertainty is determined for the PAS for typical conditions [*Lewis et al.*, 2008]. All data are reported for ambient temperature and pressure.

4.7 Sizing rack – aerosol size distribution

A sizing rack, built at CSU [*Hand*, 2001], was used to measure particle size distributions. The sizing rack utilizes three separate techniques to measure the size distribution of particles over different ranges: the TSI Aerodynamic Particle Sizer 3320 (APS) measures particles 0.53 – 22 μm, the PMS Optical Particle Counter: LASAIR 1003 (OPC) measures particles 0.2 – 2 μm, and the TSI 3071 Differential Mobility Analyzer (DMA) measures particles 0.04 – 0.84 μm. Capitalizing on the different diameter ranges

measured by each instrument, density and refractive index of the aerosol particles can be retrieved [*Hand*, 2001]. For this work, only data from the DMA and OPC were used, measurements reported by the APD during FLAME2 indicated error due to poor calibration.

OPC derived particle diameters depend on the refractive index of a particle and assume the particle has no contribution from absorption. The OPC is calibrated using several types of purely scattering particles of known size and refractive index. Absorbing particles will cause a different instrumental response than scattering particles leading the OPC to over or underestimate the size of the particles; because particles larger than 0.3 μm are used in the alignment procedure discussed below, particle diameters of absorbing aerosols will be underestimated [*Hand et al.*, 2002].

A Twomey inversion was applied to the raw DMA and OPC measurements to produce a finer resolved distribution as well as correct for instrumental response [*Hand*, 2001]. The inverted DMA and OPC distributions were aligned to produce a particle size distribution covering a larger range. The alignment procedure varies the real part of the refractive index and OPC bin calibrations until error between the OPC and DMA inverted distributions is minimized. Because of the errors associated with the OPC for absorbing aerosols, aligned DMA and OPC particle size distributions were used only for aerosols with small contributions from absorption; for aerosols where there was a large contribution from absorption distributions from the DMA only were used.

One source of error in the DMA measurement is from multiply charged particles. The DMA measures the particle size distribution using the mobility of the particle, Z_p,

$$Z_p = \frac{v_t}{E} = \frac{neC_p}{3\pi\eta\chi D_p} \qquad 4\text{-}5$$

where v_t is the terminal velocity of the particle in an electric field E, e is the charge of an electron, η is the viscosity of air, C_p is the Cunningham correction factor, χ is the shape factor, n is the number of elementary charges and D_p is the particle diameter. Thus a particle with a given mobility can have a number of different diameters, D_p, depending on the number of charges on the particle. This causes larger particles which have been multiply charged to be measured by the DMA as smaller particles. The charging efficiencies of particle sizes are well known and therefore if the full size distribution of the particles can be measured, corrections for multiply charged particles can be applied. If the full size distribution is not known, there is no way of knowing how many large particles are present and how many were incorrectly measured as small particles due to multiple charges. For this work, refractive index was retrieved for cases where the size distribution was not always known and there might be increased error due to multiply charged particles.

A second source of error in the DMA measurement is due to the shape factor, χ, used in the calculation of particle mobility. The shape factor describes the sphericity of a particle, and for our study spherical particles were assumed, giving a value of $\chi = 1$. It is well known that absorbing, sooty particles can be highly non-spherical [*Martins et al.*, 1998], giving a shape factor $\chi > 1$. Solving equation 5.5 for D_p

$$D_p = \frac{neC_p}{3\pi\eta\chi Z_p} \propto \frac{1}{\chi Z_p} \qquad 4\text{-}6$$

it can be seen that the calculated diameter of a particle is inversely proportional to the mobility and shape factor of the particle. If non-spherical particles are measured and are

assumed to be spherical, the measured diameters would be overestimated, indicating larger particles than are actually present. This could lead to significant errors in the extinction, scattering and absorption coefficients calculated using Mie theory and lead to an incorrect retrieved refractive index.

A large source of error in the OPC is due to the uncertainty in refractive index and contributions from absorption. As a significant portion of the aerosols measured during FLAME2 have a large contribution from absorption, the OPC will incorrectly size the particles present. For aerosols which primarily scatter light, uncertainties due to refractive index for scattering aerosols will be accounted for by the alignment procedure which varies the assumed refractive index of the aerosol until the DMA and OPC measured size distributions agree [*Hand*, 2001]. If an absorbing particle is measured by the OPC, diameters will be underestimated yielding error in the aligned distribution. For this work, aligned DMA and OPC size distributions were used for aerosols with SSA > 0.85, for SSA < 0.85 only DMA data were used to construct the size distribution.

For aerosol samples with large number concentrations, the OPC response can saturate so that the size distributions are no longer accurately measured. If large number concentrations are present, the OPC may sample multiple particles at one time. This would cause the OPC to under measure the total number of particles present. Multiple particles would also give a larger scattering single leading the OPC to overestimate the particle size. Data measured while the OPC was saturated were not used in any calculation.

Uncertainty in extinction, scattering and absorption coefficients derived from measured size distributions are found using Hand [2001]

$$\delta \mathrm{b} = \sum_i \left[\left(\frac{3Q_i}{2D_{p,i}} \right)^2 (\delta V_i)^2 + \left(\frac{3Q_i V_i}{2D_{p,i}^2} \right)^2 \left(\delta D_{p,i} \right)^2 \right]^{1/2} \quad \text{4-7}$$

where δb represents δb_{ext}, δb_{sca} or δb_{abs} for a corresponding Q_{ext}, Q_{scat} and Q_{abs} calculated using Mie Theory, and D_p is the diameter of each bin with corresponding volume concentration V. Uncertainties in the volume concentration, δV, are calculated from uncertainties in diameter and number; uncertainty in diameter depends most strongly on uncertainties in shape factor and has been assumed to have a constant value of $\delta D_p = 0.05$ μm [*Hand*, 2001].

For this study, the DMA was run with a sheath flow of 3 lpm and a sample flow rate of 0.3 lpm. The size distributions from the DMA were obtained using a stepping DMPS mode which ranged in size from 0.05 μm to 0.84 μm over 10 minutes, OPC size distributions were obtained for the same 10 minute sampling period. Data from the CRD, nephelometer and PAS were averaged to match the sampling rate of the size distributions. All sizing data were reported at ambient conditions. Further details of the sizing rack and data reduction are reported in Levin [2008]

4.8 Ammonium Sulfate Calibration

During the FLAME2 study at the Fire Science Lab, an ammonium sulfate calibration was performed for all of the instruments in the optical closure portion of the study. Ammonium sulfate was chosen as it has well known optical properties, is easy to generate, and is purely scattering. Similar to the PSL calibrations described in section *3.2 PSL calibrations*, extinction and scattering coefficients measured by the CRD and the nephelometers were compared to extinction coefficients calculated using Mie theory and

measured size distributions, Values were compared to evaluate biases and inaccuracies in the measured extinction and scattering coefficient measurements.

Polydisperse ammonium sulfate aerosol was generated with a TSI 3076 constant output atomizer and mixed with dry room air in a 55 gallon drum; a sample line ran from the drum to a smaller manifold in an adjacent room from which each instrument in the optical closure study sampled. Dilution with room air dried the aerosol to a relative humidity of <26% by the time it reached the instruments.

Using the known index of refraction for ammonium sulfate, $n = 1.534+0i$ at 532 nm, and measured size distributions (Figure 4-6) a Mie code was used to calculate the extinction and scattering coefficients for each averaged data point. Aligned size distributions were obtained using measurements from the DMA and OPC, using the methods described above. A 10 minute average was applied to the measured extinction and scattering coefficients to match the scan time of the sizing rack. TSI nephelometer scattering coefficients were corrected for the gas calibration performed at the end of the study as well as corrected to 532 nm. CRD measured extinction coefficients were corrected for particle loss and the purge flow.

Prior to ammonium sulfate aerosol sampling, a filter system was placed on the drum and each instrument measured the extinction/scattering coefficient of "zero air". Concentrations of ammonium sulfate aerosol were raised or lowered by altering the amount of dry filtered room air used to dilute the atomized aerosol. Aerosol concentrations were measured at three concentration levels giving a total of four averaged data points; the concentration was held relatively constant during each 10 minute measurement period.

The validity of the Anderson and Ogren correction for the TSI nephelometer was checked using the ammonium sulfate aerosol data. Measured scattering coefficients not corrected for truncation were compared to scattering coefficients calculated using a Mie code where the angular nonidealities of the nephelometer were accounted for (*Appendix A: Mie code and correction for TSI nephelometer* angular non-idealities). Measured scattering coefficients corrected according to Anderson and Ogren [*Anderson and Ogren*, 1998] and scattering coefficients calculated using a Mie code with no correction for angular nonidealities were also compared. Corrected (uncorrected) nephelometer scattering coefficients compared well to uncorrected (corrected) Mie theory scattering coefficients; regressions of 0.917 and 0.950 respectively were found (Figure 4-7, Table 4.2). A regression of 1.002 was found comparing scattering coefficients from the reciprocal nephelometer (section *4.6 Photoacoustic – absorption coefficient*) and Anderson and Ogren truncation corrected TSI nephelometer scattering coefficients (Figure 4-8).

Table 4.2 *Regression values found between corrected (uncorrected) TSI nephelometer scattering coefficients and uncorrected (corrected) scattering coefficients found from Mie theory.*

		TSI nephelometer scattering coefficients (λ = 532 nm)	
		Angular non-idealities corrected according to Anderson and Ogren (1998)	Uncorrected
Scattering coefficients from Mie theory	Uncorrected	0.917	
	Angular non-idealities accounted for		0.950

The good agreement found between scattering coefficients measured by the TSI nephelometer and calculations from Mie theory as well as good agreement between nephelometers indicates that the Anderson and Ogren correction for angular nonidealities

adequately corrects the error in the TSI nephelometer measurements and can be applied without hesitation to the FLAME2 data.

Extinction coefficients measured by the CRD were compared with TSI nephelometer scattering coefficients corrected for angular non-idealities and indicated poor agreement (Figure 4-8). Assuming that the corrected TSI nephelometer is the correct scattering measurement, an additional correction for the CRD measured extinction coefficients of at least 1/0.739 = 1.353 is indicated over the range 0 – 600 Mm^{-1}; this correction was applied to all of the subsequent burn data. It was later determined that the cause of the large error in extinction measurements during FLAME2 was due to problems with contamination in the signal (*3.6 Multi-exponential decay*).

4.9 Index of refraction retrieval

Using Mie Theory, it is possible to find an extinction cross section and index of refraction consistent with an aerosol sample if the full size distribution and extinction, scattering or absorption coefficients are known. If the aerosol being observed is purely scattering, such as ammonium sulfate, only b_{ext} or b_{scat} need to be known; while if the aerosol has contributions from both absorption and scattering, at least two of the three, $b_{ext,}$ b_{scat} or $b_{abs,}$ need to be known in addition to size distribution and an assumption of sphericity.

The index of refraction retrieval method outlined below is based on that used by Riziq [2007]. Values of Q_{ext}, Q_{scat} and Q_{abs} were calculated using a Mie Code for values of real and imaginary indices of refraction $1.0 < n < 2.5$ and $0 < i < 0.7$, where $m = n + ik$. To increase the resolution of the refractive index retrieval, 400 values of real and

imaginary indices of refraction were used. Using experimentally measured size distributions, values of $b_{ext,}$ b_{scat} and b_{abs}.

$$b_{ext} = \sum \sigma_{ext,i} dN_i = \sum Q_{ext,i} \frac{\pi}{4} D_{p,i}^2 dN_{p,i}$$

$$b_{scat} = \sum \sigma_{scat,i} dN_i = \sum Q_{scat,i} \frac{\pi}{4} D_{p,i}^2 dN_{p,i}$$

$$b_{abs} = \sum \sigma_{abs,i} dN_i = \sum Q_{abs,i} \frac{\pi}{4} D_{p,i}^2 dN_{p,i} \qquad 4\text{-}8$$

The best-fit index of refraction is found by finding the minimum error between the measured and calculated values for each refractive index guess. The error between measured and calculated values is defined by the merit function χ^2/N [*Dinar et al.*, 2008; *Riziq et al.*, 2007] where

$$\chi^2 = \sum_{i=1}^{N} \frac{\left(y_{meas} - y_{calculated}\right)_i^2}{\varepsilon_{i\,meas}^2 + \varepsilon_{i\,calc}^2} \qquad 4\text{-}9$$

where y_{meas} is the measured value of interest, $y_{calculated}$ is the corresponding calculated value, ε_{meas} is the uncertainty associated with the measured quantity, ε_{calc} is the uncertainty associated with the calculated quantity and N is the number of elements being summed over. The best fit refractive index is then the set of n and k for which χ^2 is minimum, $\chi^2_{min.}$ For this work, the merit function was summed over A.) b_{ext} and SSA_{ext_scat}, calculated using measurements of b_{ext} and b_{scat} and B.) b_{scat} and SSA_{scat_abs}, calculated using measurements of b_{scat} and b_{abs}.

$$\text{A.)}\quad \chi^2 = \sum_{i=1}^{N} \frac{\left(b_{ext\_meas,i} \quad b_{ext\_calc,i}\right)^2}{\Delta b_{ext\_meas,i}^{\ 2} + \Delta b_{ext\_calc,i}^{\ 2}} + \frac{\left(SSA_{ext\_scat,i} - SSA_{calc,i}\right)^2}{\Delta SSA_{ext\_calc,i}^{\ 2} + \Delta SSA_{calc,i}^{\ 2}} \qquad 4\text{-}10$$

$$\text{B.)}\quad \chi^2 = \sum_{i=1}^{N} \frac{\left(b_{scat\_meas,i} \quad b_{scat\_calc,i}\right)^2}{\Delta b_{scat\_meas,i}^{\ 2} + \Delta b_{scat\_calc,i}^{\ 2}} + \frac{\left(SSA_{scat\_abs,i} - SSA_{calc,i}\right)^2}{\Delta SSA_{scat\_abs,i}^{\ 2} + \Delta SSA_{calc,i}^{\ 2}}$$

Uncertainties for SSA were calculated according to *1.3.1 Single scattering albedo measurement,* uncertainties in Δb_{ext_meas}, Δb_{scat_meas} and Δb_{abs_meas} are described previously in this chapter and uncertainties from calculations of Δb_{ext_calc}, Δb_{scat_calc} and Δb_{abs_calc} are described previously in this chapter. The merit function was summed over some number of time periods, N. If the measurement errors, ε_{meas} and ε_{calc} are normally distributed, calculated values of χ^2 will follow a χ^2 distribution [*Dinar et al.*, 2008]. A χ^2 distribution with two degrees of freedom, n and k, has a 1 σ confidence level at a value of $\chi^2 = 2.298$. Thus, uncertainty in refractive index, Δn and Δk, can be found determining where $\chi^2 \leq \chi^2_{\min} + 2.298$; where χ^2 are one standard deviation away from the minimum value.

The refractive index retrieval was done using both methods A and B as a further measure of the closure between the instruments. If closure between the instruments is good, refractive indices retrieved using each method should be similar.

Several limitations of the retrieval method should be noted. Mie Theory assumes that all particles are spherical, which in the case of soot or agglomerated particles is not valid. The refractive index retrieval also assumes that the size distributions used in the Mie Code are full and accurate representations of the particles. Size distributions used in this study were measured using a Differential Mobility Analyzer (DMA), assuming spherical particles, and an Optical Particle Counter (OPC) for highly scattering aerosols;

limitations of each instrument are described in *4.7 Sizing rack – aerosol size distribution*. Thus the refractive index that is retrieved will not be a good representation of the true values for non-spherical or highly absorbing aerosols.

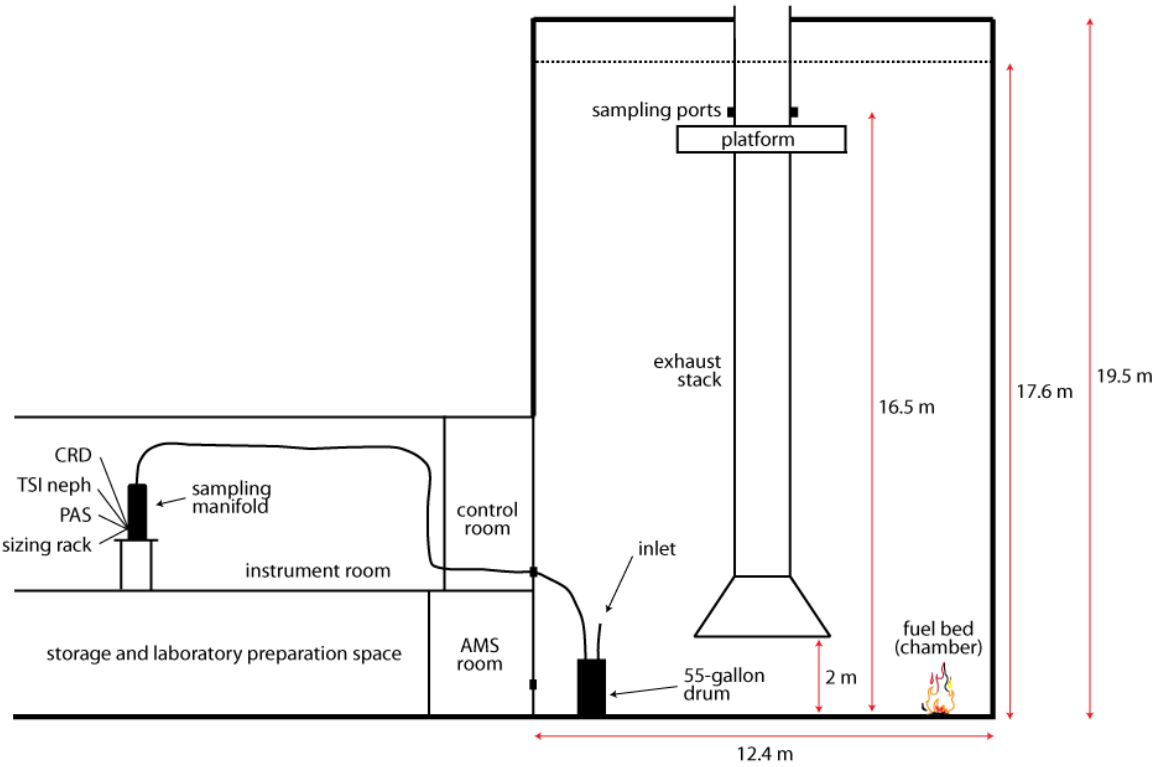

Figure 4-1 *Diagram of Fire Science Laboratory where FLAME 2 experiments were performed.*

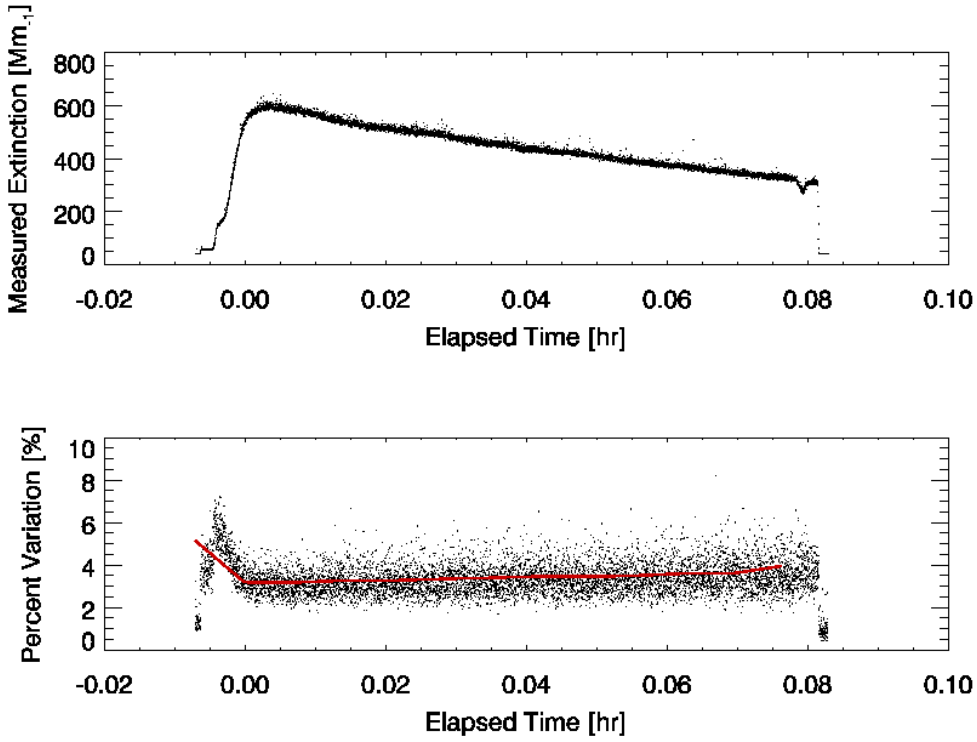

Figure 4-2 *Sample burn from FLAME2, the top plot is example of 1 sec average of measured CRD extinction during burn. The bottom plot is percent variance for same burn; the red line indicates 10 minute average of percent variance.*

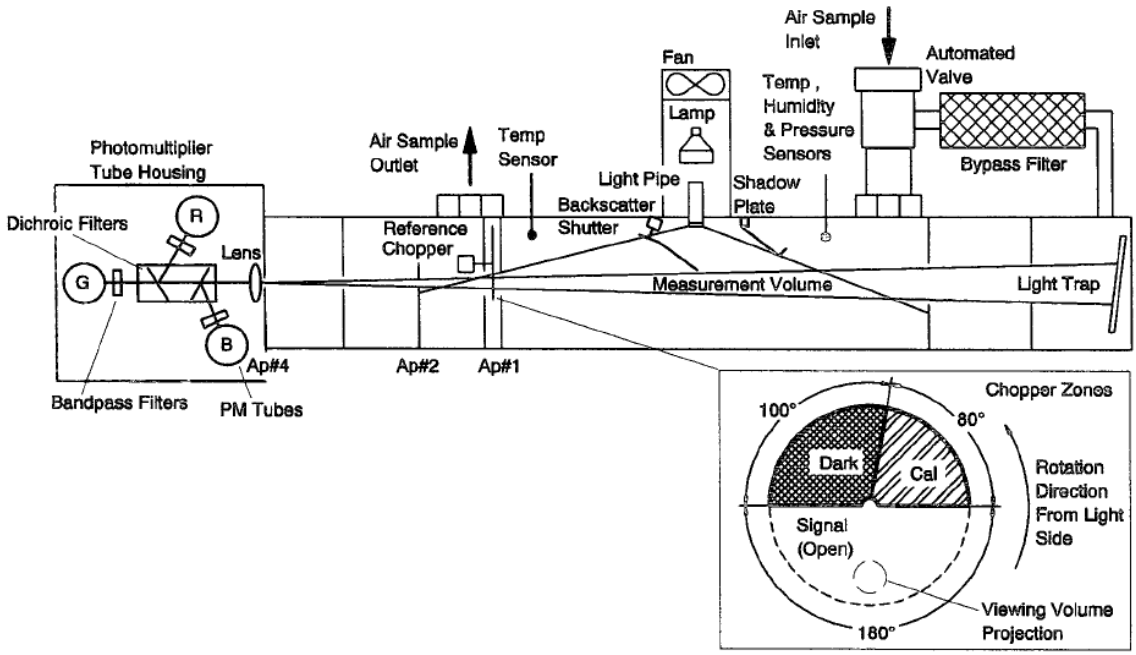

Figure 4-3 *Schematic of TSI nephelometer model 3563 [Anderson et al., 1996]*

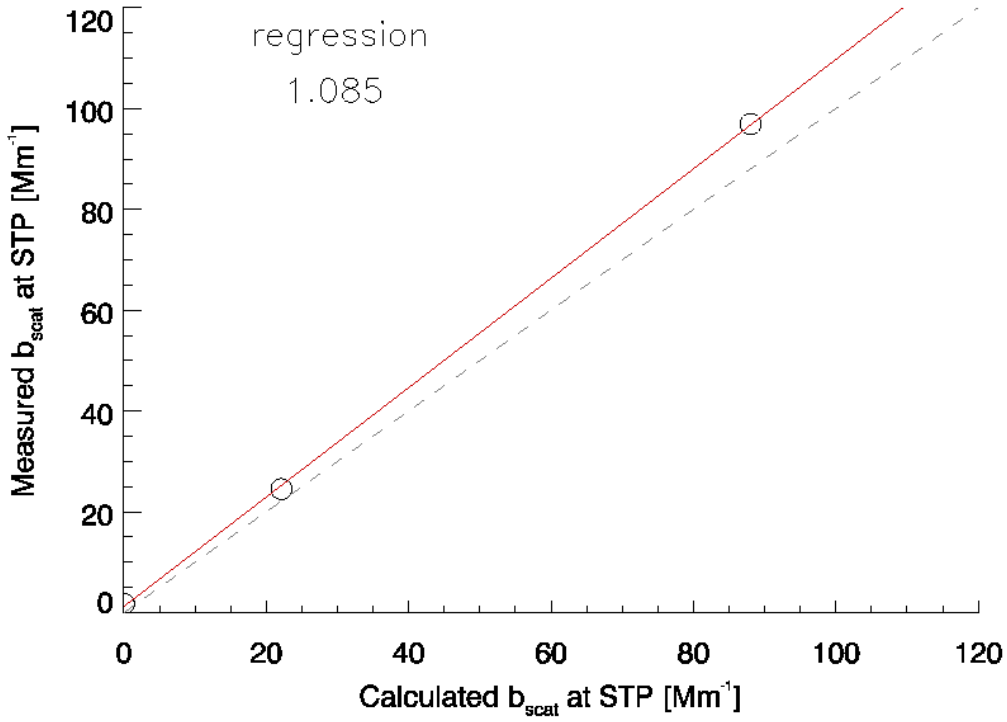

Figure 4-4 *The TSI nephelometer calibration done using filtered air, CO_2 and SUVA (HCF-134a) gas at 532 nm. Correction of 1/1.085 = 0.922 determined.*

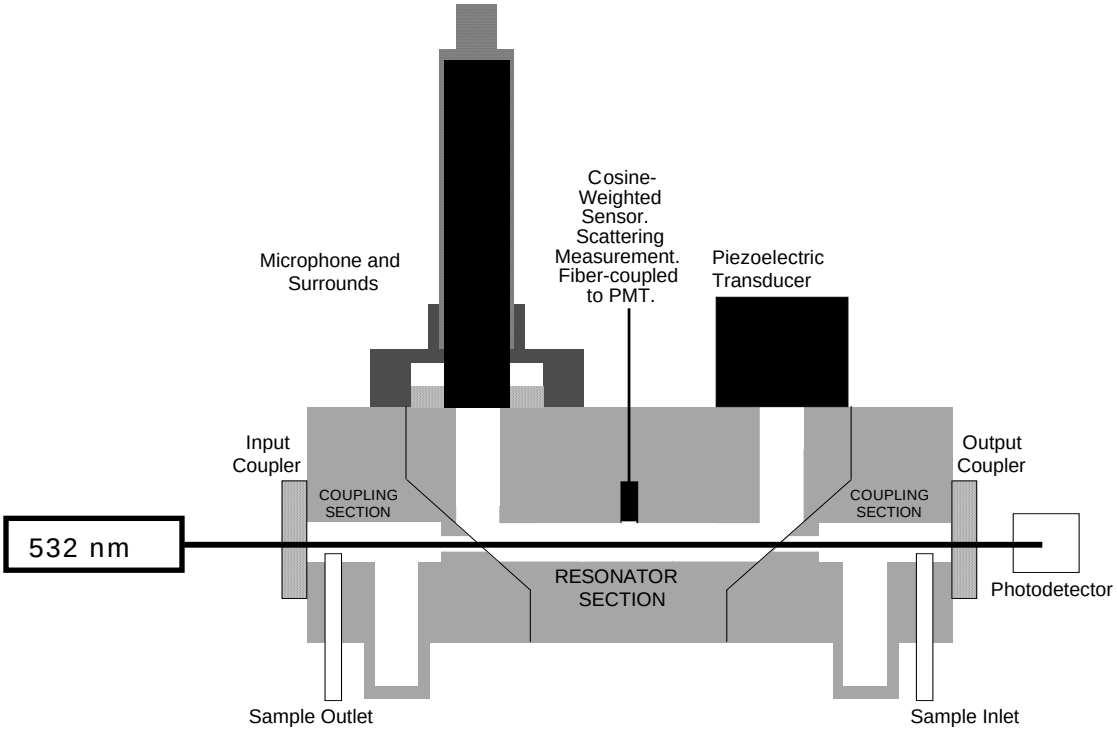

Figure 4-5 *Schematic of 532 nm Photoacoustic[Lewis, 2007]*

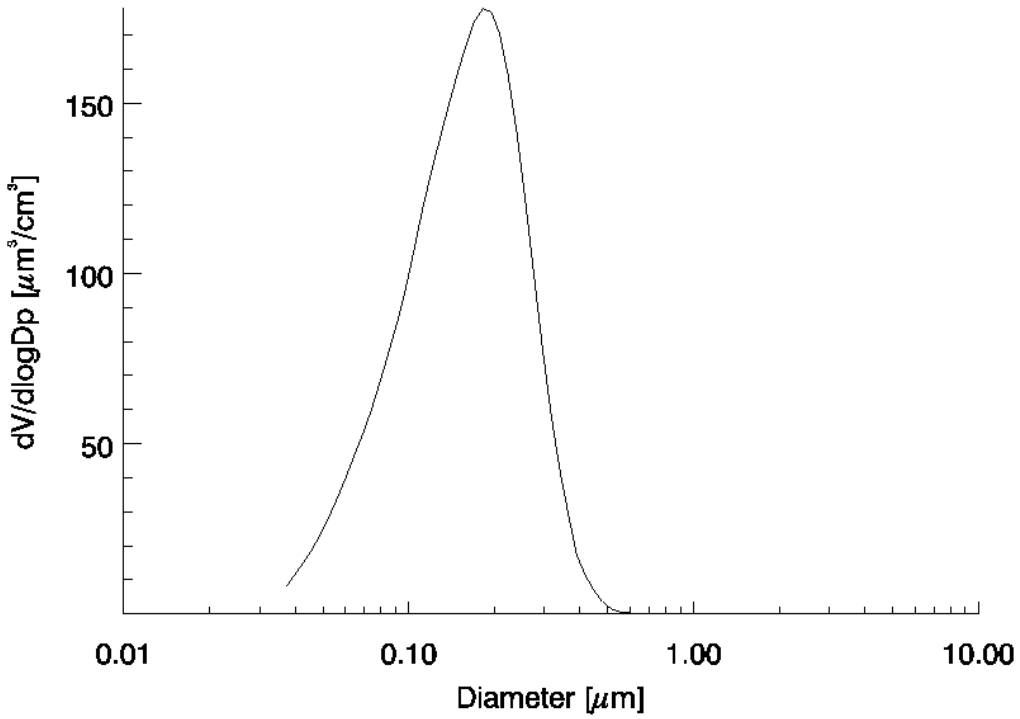

Figure 4-6 *Sample aligned size distribution for ammonium sulfate calibration from FLAME2.*

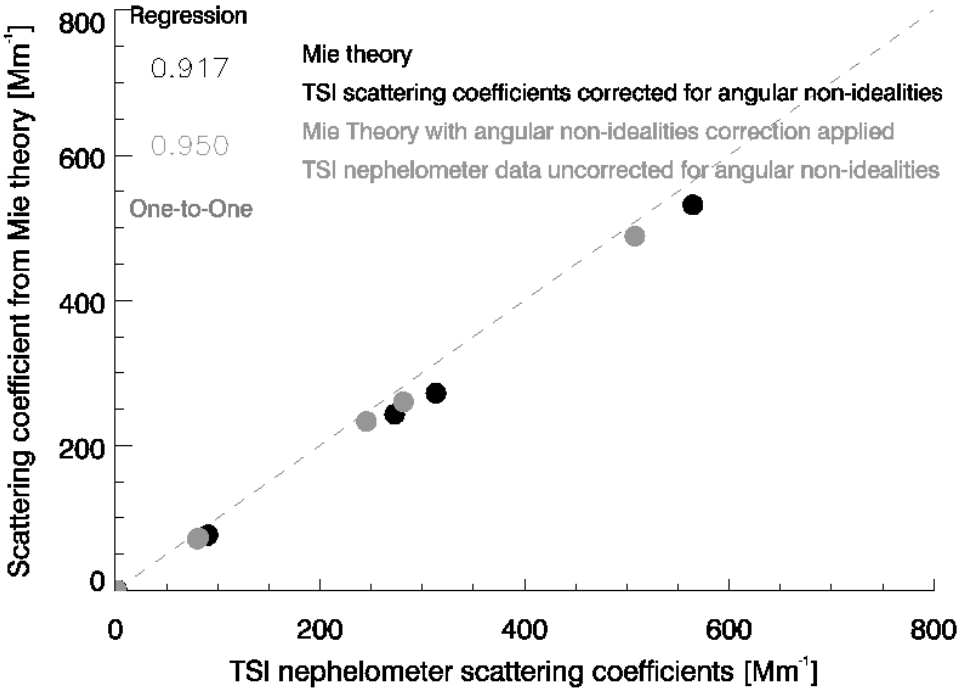

Figure 4-7 *Comparison of corrected (uncorrected) TSI nephelometer scattering coefficients and uncorrected (corrected) Mie Theory scattering coefficients in black (grey). TSI nephelometer angular non-idealities are well modeled by the Anderson and Ogren correction.*

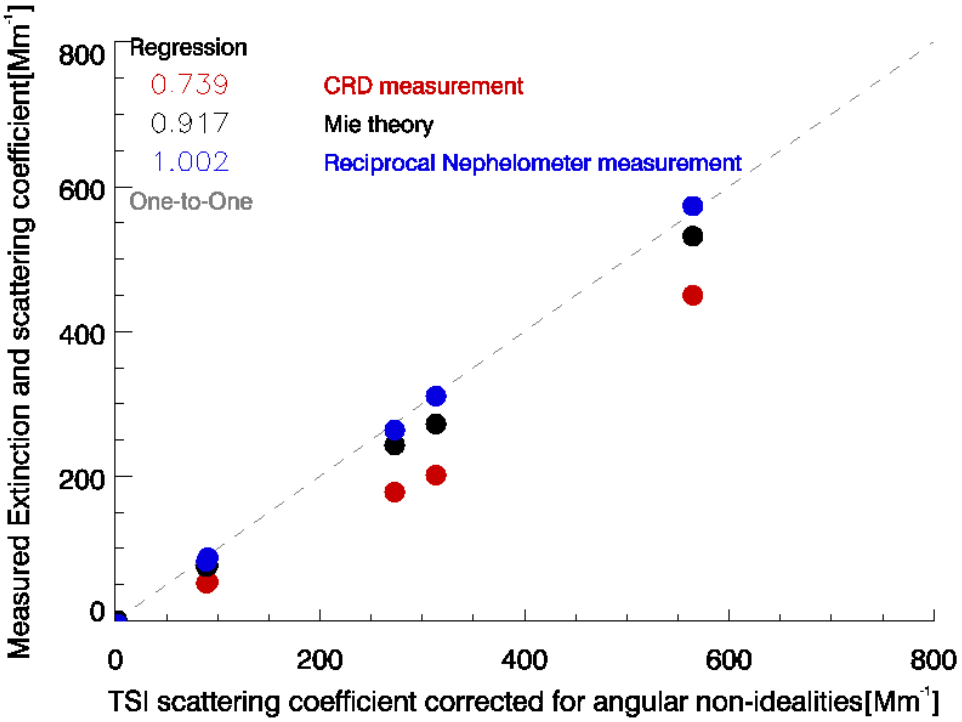

Figure 4-8 *Comparison of corrected TSI nephelometer measurements to CRD extinction coefficients, calculated scattering coefficients from Mie Theory and scattering coefficients from the reciprocal nephelometer. A correction of 1/0.739 is needed for the measured CRD extinction coefficients.*

Chapter 5 RESULTS

After corrections were applied to each of the measurements as outlined in Chapter 4, the data were analyzed to determine whether there was optical closure between instruments at the common wavelength λ = 532 nm and to compute single scattering albedo (SSA) and index of refraction for the smoke produced by each of the fuels. For reference, the list of fuels and burn numbers are listed in Chapter 4. Extinction coefficients were corrected for particle loss, purge flow and the ammonium sulfate calibration correction, yielding a total applied correction factor of 1.477. TSI nephelometer scattering coefficients were corrected for the gas calibration done at the end of the study, corrected to 532 nm using the angstrom exponent and corrected for angular non-idealities using the Anderson and Ogren [1998] correction outlined in Chapter 4. Measured size distributions (DMA and OPC) were corrected for particle loss and aligned DMA/OPC size distributions were corrected for multiply charged particles.

5.1 Extinction closure

One of the goals of this study was to determine if there was good agreement between the three optical instruments, i.e. measured absorption + measured scattering = measured extinction, where scattering measurements used are from the TSI nephelometer. Aerosol absorption coefficients can be difficult to measure directly [*Sheridan et al.*, 2005] so often the difference method, $b_{abs} = b_{ext} - b_{scat}$, is used to determine the contribution of absorption from an aerosol. When absorption coefficients

are small, a small uncertainty in either the extinction or scattering coefficient can lead to large errors in calculated absorption [*Bond et al.*, 1999]. Independent measurements of extinction, scattering and absorption coefficients in this study make it possible to determine if there was agreement between measurements.

Figure 5-1 shows the comparison between measured extinction coefficients and the sum of measured absorption and measured scattering coefficient. Good agreement was found between these quantities for the FLAME2 chamber study with an r^2 value of 0.998 (Figure 5-1). Measured absorption coefficients were compared to absorption coefficients found from the difference method, b_{ext_meas} - b_{scat_meas} (Figure 5-2) and an r^2 = 0.986 was found. Large absorption coefficients show a better agreement in part because the small uncertainties in scattering and extinction no longer have as large an effect on the calculated differences. Lower values of absorption coefficient still compare well but show an increase in variability around the 1-1 line.

5.2 Single scattering albedo

Values of single scattering albedo (SSA) for each burn were calculated using extinction and scattering measurements, $SSA_{ext\_scat} = \frac{b_{scat}}{b_{ext}}$ [method A], and scattering and absorption measurements, $SSA_{scat\_abs} = \frac{b_{scat}}{b_{scat} + b_{abs}}$ [method B]. Calculated values of SSA compare well with an r^2 = 0.974, indicating no bias although several values of SSA_{ext_scat} lie outside of the physical range of SSA.

SSA is an indicator of the fraction of total extinction caused by scattering and physical values range from 0 to 1. When the SSA of an aerosol is very close to 1,

uncertainty in extinction and scattering coefficients can cause measured scattering coefficients to be greater than the measured extinction coefficients giving an unphysical SSA greater than 1. If SSA is equal to 1 within uncertainty, it can reasonably be assumed to be 1. If SSA is not equal to 1 within uncertainty then it indicates that b_{ext_meas} was not corrected sufficiently by the ammonium sulfate calibration correction or the Anderson and Ogren correction for angular non-idealities overcorrected b_{scat_meas}. Because of the correction needed by the CRD, values of SSA_{scat_abs} will be used as the true values from here on. Values of SSA_{scat_abs} also cannot produce unphysical values of SSA, SSA > 1, based simply on the way it is calculated.

The average SSAs of each burn were calculated for all chamber burns and are listed in Table 5.1. The calculated values of SSA_{ext_scat} and SSA_{scat_abs}, were compared (Figure 5-3) and showed good agreement with a correlation of 0.948; values of SSA less than 0.8 compared better than those closer to 1. Calculated values of SSA_{ext_scat} had a higher level of uncertainty than SSA_{scat_abs}, larger uncertainty near 1 and included values greater than 1. SSA values greater than 1 reflect unphysical values of SSA_{ext_scat}. Calculated values of SSA_{scat_abs} are shown in Figure 5-4 and range from 0.43 to 0.99.

Table 5.1 *Average SSA, retrieved refractive index and merit function calculated using method A and B (See 4.9 Index of refraction retrieval) for each Chamber burn during FLAME2 for λ = 532 nm. Different size distributions were used in the refractive index retrieval and choices of which distribution to use were based on the limitations described in Chapter 4. Refractive indices retrieved for size distributions where the size distribution captured a significant portion of the particles (as described in section 5.3 Retrieved refractive index) are shaded in yellow.*

				Method A				Method B			
ID	Fuel Type	DMA only	DMA/OPC alignment	SSA_{ext_scat}	χ^2/N^2	*n*	*k*	SSA_{scat_abs}	χ^2/N^2	*n*	*k*
113	*LLP and wire grass*		•	0.877 ± 0.044	0.004	1.466 ± 0.094	0.019 ± 0.036	0.934 ± 0.003	0.007	1.447 ± 0.075	0.009 ± 0.024
114	*Black needlerush*		•	0.900 ± 0.026	0.152	1.526 ± 0.113	0.018 ± 0.036	0.918 ± 0.004	0.256	0.504 ± 0.162	0.008 ± 0.032
115	*Oak and hickory*	•		0.887 ± 0.022	0.038	1.639 ± 0.023	0.024 ± 0.013	0.852 ± 0.005	0.087	1.647 ± 0.015	0.033 ± 0.008
116	*Douglas fir*	•		0.550 ± 0.013	0.902	1.252 ± 0.011	0.052 ± 0.006	0.527 ± 0.007	4.202	1.259 ± 0.004	0.061 ± 0.007
117	*Dry Douglas fir*		•	0.987 ± 0.046	0.013	1.590 ± 0.038	0.002 ± 0.022	0.958 ± 0.002	0.041	1.609 ± 0.086	0.007 ± 0.020
118	*Palmetto*	•		0.433 ± 0.013	0.190	1.180 ± 0.011	0.053 ± 0.005	0.428 ± 0.005	2.210	1.180 ± 0.004	0.052 ± 0.008
119	*Palmetto*	•		0.597 ± 0.020	0.140	1.233 ± 0.023	0.039 ± 0.013	0.615 ± 0.007	0.491	1.248 ± 0.015	0.046 ± 0.018
120	*Rice straw*		•	0.824 ± 0.030	0.021	1.508 ± 0.068	0.029 ± 0.025	0.890 ± 0.004	0.036	1.395 ± 0.034	0.010 ± 0.018
121	*Duff*		•	0.965 ± 0.039	0.012	1.508 ± 0.056	0.004 ± 0.014	0.970 ± 0.001	0.053	1.508 ± 0.064	0.004 ± 0.012
122	*Rhododendron*	•		0.788 ± 0.020	0.019	1.538 ± 0.023	0.034 ± 0.011	0.809 ± 0.006	0.074	1.534 ± 0.011	0.029 ± 0.009
123	*Black Spruce*	•		0.663 ± 0.018	0.360	1.316 ± 0.015	0.047 ± 0.010	0.666 ± 0.008	1.291	1.320 ± 0.008	0.049 ± 0.009
124	*Dry Douglas fir*		•	1.040 ± 0.039	5.338	1.669 ± 0.053	0 ± 0.008	0.975 ± 0.001	42.709	1.654 ± 0.004	-
125	*Duff*		•	0.984 ± 0.040	0.013	1.718 ± 0.124	0.002 ± 0.018	0.990 ± 0.001	0.048	1.718 ± 0.162	0.002 ± 0.015
126	*Wiregrass*	•		0.821 ± 0.039	0.218	1.556 ± 0.064	0.031 ± 0.023	0.853 ± 0.005	0.288	1.553 ± 0.060	0.026 ± 0.022
127	*Chamise*	•		0.422 ± 0.008	0.032	1.211 ± 0.008	0.066 ± 0.004	0.429 ± 0.005	0.107	1.211 ± 0.004	0.063 ± 0.006
128	*Black needlerush*		•	0.961 ± 0.035	0.022	1.586 ± 0.045	0.007 ± 0.019	0.900 ± 0.004	0.030	1.624 ± 0.083	0.021 ± 0.021
129	*Sage*	•		0.722 ± 0.018	0.061	1.432 ± 0.019	0.057 ± 0.012	0.701 ± 0.007	0.102	1.432 ± 0.011	0.057 ± 0.012
130	*Longleaf pine*		•	1.104 ± 0.055	0.113	1.519 ± 0.169	0.015 ± 0.042	0.951 ± 0.002	0.004	1.504 ± 0.132	0.009 ± 0.027
131	*Gallberry*	•		0.448 ± 0.009	0.017	1.184 ± 0.008	0.050 ± 0.004	0.446 ± 0.006	0.076	1.184 ± 0.004	0.049 ± 0.006
132	*Sugarcane*	•		0.652 ± 0.026	11.464	1.162 ± 0.008	0.030 ± 0.004	0.696 ± 0.007	79.662	1.207 ± 0.008	0.034 ± 0.006
133	*White spruce*	•		0.902 ± 0.027	0.053	1.477 ± 0.030	0.011 ± 0.012	0.910 ± 0.004	0.098	1.477 ± 0.019	0.010 ± 0.010

Fuels with the lowest measured values of SSA_{ext_scat} were Florida palmetto, chamise and gallbery, with values below 0.5. Douglas fir needles and branches, Mississippi palmetto, Alaskan black spruce, Chinese sugarcane and sagebrush produced low SSAs, in the range 0.527 to 0.701. Rhododendron, oak and hickory leaves, Florida wiregrass and rice straw gave SSAs in a middle range from 0.809 to 0.890. Fuels with the highest SSA were black needlerush, Alaskan white spruce, longleaf pine and wiregrass, longleaf pine needles, Douglas fir and Alaskan duff with SSAs > 0.9.

Several fuels were burned multiple times, making it possible to compare measured SSAs for each burn. Alaskan duff was burned during burns 121 and 125 producing aerosols with SSA_{ext_scat} of 0.965 and 0.984 and SSA_{scat_abs} of 0.970 and 0.990. Black needlerush was burned during burns 114 and 128. Calculated values of SSA, SSA_{ext_scat} of 0.900 and 0.961, SSA_{scat_abs} of 0.918 and 0.900, agreed well except SSA_{ext_scat} for burn 128. Douglas fir was burned three times during the course of the study, twice (burns 117 and 124) using dry fir that produced smoke with SSA_{ext_scat} of 0.987 and 1.040 and SSA_{scat_abs} of 0.958 and 0.975; burn 116 was fresh fir needles and branches producing SSA_{ext_scat} of 0.550 and SSA_{scat_abs} of 0.527. Longleaf pine needles and wiregrass were each burned separately (burns 130 and 126) producing SSA_{scat_abs} of 0.951 and 0.853 respectively. A mixture of the two fuels produced aerosols with an SSA_{scat_abs} of 0.934, between that of the individual fuels.

Elemental carbon is often used to describe the substance in a sample that is the most soot-like and causes the measured light absorption. The apparent elemental carbon (EC_a) is specifically the fraction of carbon that is oxidized above a certain temperature during combustion analysis [*Andreae and Gelencser*, 2006]. Measured values of

SSA_{scat_abs} were compared to calculated values of EC_a mass fractions (Figure 5-5) calculated for each burn during the study. The methods used to calculate values of EC_a are described in another work, [*Holden*, 2008]. SSA_{scat_abs} and EC_a were strongly correlated with an $r^2 = 0.887$, where larger values of EC_a corresponded to lower values of SSA.

5.3 Retrieved refractive index

The index of refraction of aerosols was found for each burn using the retrieval described in *4.9 Index of refraction retrieval*; the merit function was minimized in two ways, using values of SSA_{ext_scat} and b_{ext} (method A) and using values of SSA_{scat_abs} and b_{scat} (method B). Refractive indices retrieved using each method produced similar values, which was expected due to the good instrument closure already discussed.

Although refractive indices retrieved for both method A and B are reported for every burn in Table 5.1, many of the reported retrieved refractive indices are fit using unreliable size distributions as discussed below. Refractive indices retrieved using method A were also deemed to be less reliable as measurements of extinction coefficient had to be heavily corrected due to software problems.

Aligned size distributions were shown to be unreliable when strongly absorbing particles were present [*Levin*, 2008]. In those cases only DMA distributions were used for the retrievals but the DMA measurements had an upper size limit of 0.87 μm. For many of the burns, a significant fraction of the total volume in particle sizes was larger than 0.87 μm and the DMA was unable to adequately capture the distribution. Further, without OPC data, corrections for multiply charged particles in the DMA inversion are not accurate. Because larger particles generally cause more aerosol extinction than

smaller particles, particle volume distributions are a good indicator of whether the measured distribution captured most of the extinction causing aerosols. If the peak of the volume distribution was captured by the DMA, the DMA measured size distribution could be fit to a lognormal distribution and the missing data could be filled in. For cases where the peak of the volume distribution was not captured by the DMA, it is not possible to fit the distribution.

Burns 120, 122, 127, 128, 129 and 133 had volume size distributions (DMA or aligned distributions as indicated in Table 5.1) that were deemed satisfactory or could be improved (Figure 5-6 through Figure 5-11); in particular the entire size distribution was captured for burn 133. Measured DMA volume distributions for burns 120, 122 and 127 were fit with lognormal distributions to fill in missing portions and distributions for burn 127 and 129 were shifted by a shape factor of 1.32 to account for the possibility of non-spherical particles.

5.4 Burn 127, Chamise

Burn 127, chamise, had one of the lowest average SSAs of the study (0.43) due to a large contribution from absorption (Figure 5-12). The large contribution from absorption indicates the likelihood of non-spherical particles in the sample. If the measured particles are non-spherical, size distributions measured by the DMA for these burns will overestimate the physical diameter of the particles. Using the DMA measured size distributions a refractive index of $m = 1.211 \pm 0.004 + i0.063 \pm 0.006$ with a merit function of 0.107 was retrieved for burn 127 (Figure 5-13). The extremely low retrieved index of refraction is likely biased due to the presence of non-spherical particles.

To examine the possible shape factor effect on the DMA measured size distributions, the refractive index retrieval was rerun assuming a shape factor of 1.32, relevant for a 4 sphere chain [*Hinds*, 1982]. Thus, measured DMA size distributions were shifted down by a factor of 1.32 to smaller particle diameters (Figure 5-14). The refractive index retrieval was rerun (Figure 5-15) giving a new refractive index of $m = 1.425 \pm 0.015 + i0.153 \pm 0.027$ for a merit function of 0.030. Comparing measured and calculated values of extinction, scattering and absorption coefficients (Figure 5-16) there is good agreement between measurement and calculations using refractive indices found using both the shifted and un-shifted DMA size distributions. There was a dramatic change in the retrieved refractive index (Figure 5-17). The imaginary part of the refractive index increased from $k = 0.063$ to $k = 0.153$, while the real part of the refractive index increased slightly for burn 127 to values greater than that of water ($n = 1.33 + 0i$ at $\lambda = 589$ nm).

Although shifting the size distributions by a shape factor of 1.32 did dramatically change the retrieved refractive index, many of the most optically relevant particles are not accounted for in the retrieval because the DMA doesn't capture the entire size distribution (Figure 5-8). By fitting the shifted measured DMA size distributions, information about large particle sizes can be gained. Measured particle volume distributions corrected for shape factor were fit to a bimodal lognormal distribution where each mode was modeled by

$$n_v\left(\ln D_p\right) = \frac{\pi}{6} D_p^3 n_N\left(\ln D_p\right) = \frac{\pi}{6} D_p^3 \frac{N_t}{(2\pi)^{1/2} \ln \sigma_g} \exp\left[- \frac{\left(\ln D_p - \ln \overline{D}_{pg}\right)^2}{2 \ln^2 \sigma_g} \right] \qquad 5\text{-}1$$

where N_t is the total aerosol number concentration, and $\overline{D}_{pg}$ and σ_g are the geometric mean diameter and geometric standard deviation of the distributions. The fit lognormal distribution was extended to 100 diameters ranging from 0.0076 to 7.07 μm while the measured size distribution covered only 46 diameters ranging from 0.0282 to 0.630 μm (Figure 5-18).

To estimate the differences in the captured particle extinction distributions between the DMA only and the fit size distributions, a refractive index of $m = 1.5 \pm 0.01i$ was assumed and particle extinction distributions were calculated (Figure 5-19). The residual from the fit was plotted along with the residual of the fit outside of the range of the DMA (Figure 5-20). The residual of the fit demonstrates how well the fit distribution captured the extinction in the range measured by the DMA. The residual of the fit outside the range of the DMA demonstrates the added information gained by fitting the distribution. In general, there was good agreement between the fit and measured distributions, as indicated by a small residual; for large particles, the measured distributions were consistently larger than the fit distributions. Examining the residual in the range outside of the DMA measurement, it is evident that a lot of extinction information is gained for large particle sizes. The particle extinction distributions and corresponding residuals demonstrated that our fit distributions were able to capture most of the measured particle extinction distribution as well as provide a significant amount of new information about the particle extinction distribution.

Using the fit lognormal distribution, the refractive index retrieval was rerun obtaining a merit value of 0.370 for a refractive index of $m = 1.365 \pm 0.019 + i0.150 \pm 0.007$ (Figure 5-21). Comparing measured and calculated values of extinction, scattering

and absorption coefficients using refractive indices retrieved using measured and fit size distributions (Figure 5-22) there is very good agreement between measured values and calculated values. This good agreement merely reflects the fact that a small merit function was found for each refractive index. The refractive indices retrieved using the fit lognormal distributions (Figure 5-23) also showed a large increase in the imaginary part of the refractive index, k, and a slight increase again in the real part of the refractive index, n.

Because of the large absorption by the smoke from burn 127, it was assumed that non-spherical particles influenced the distributions measured by the DMA causing the distribution to be shifted to larger particles. By shifting the particles by a shape factor of 1.32, assuming a four sphere chain, and fitting the volume distribution to fill in the missing information at larger sizes, we were able to see an increase in both the imaginary and real parts of the refractive index to more realistic values. An increase in k indicates an increase in absorption (as well as some scattering), consistent with shifting the distribution to smaller particles. Both shifted size distributions (measured and fit) increased the real index of refraction to n = 1.425 and 1.365, larger than that of water. The refractive index retrieved using the fit lognormal size distributions is likely a better estimate of the true refractive index because of the extra optical information gained at larger particle sizes and will be reported as a good representation of the true value.

5.5 Burn 129, Sagebrush

Burn 129, sagebrush, had an average SSA of 0.701 indicating a significant influence from absorption (Figure 5-24). The merit function for burn 129 was quite low, 0.046 for a refractive index of $m = 1.432 \pm 0.011 + i0.057 \pm 0.012$, indicating a good fit

between calculated and measured optical properties (Figure 5-25). Because of the high contribution of absorption, it is again likely that the DMA shifted the aerosol size distribution towards large particles leading to an incorrectly retrieved refractive index. A comparison of extinction, scattering and absorption coefficients (Figure 5-26) demonstrates that measured and calculated values compare quite well, confirming the small value of the merit function and goodness of the index of refraction fit. As well as retrieving the refractive index for the entire time period of the burn (minimizing the merit function for all data points during the burn) a refractive index was found for each time average point during the burn; this method could provide information about whether the refractive index changed during the burn. The refractive index did not vary much during the burn (Figure 5-27), staying fairly consistently near the value retrieved for the whole burn.

Because burn 129, sagebrush, had a large contribution from absorption the measured particles are again likely to be non spherical leading to error in the measured DMA size distribution. The refractive index retrieval was run using the measured size distributions corrected for a shape factor of 1.32 as described in *5.4 Burn 127, Chamise*.

A merit function value of 6.766 and refractive index of $m = 1.250 \pm 0.0 + i0.119 \pm 0.006$ were retrieved using the shifted lognormal size distribution (Figure 5-29). Comparing measured and calculated values of extinction, scattering and absorption coefficients (Figure 5-30) it is evident that this is a poor fit of refractive index. By using the shifted and fit size distribution to retrieve the refractive index, n increased to the upper bound of our retrieval (Figure 5-31).

Shifting the measured distribution by a factor of 1.32 did not at all improve the retrieved refractive index for this burn and therefore the shifted distributions were not fit with lognormals. It can then be concluded that for burn 129, a value of χ = 1.32 overcompensates for any non-spherical particles that might be present. The refractive index retrieved using the measured size distributions will then be assumed to be our best guess of the true refractive index.

5.6 Burn 122, Rhododendron and Burn 120, rice straw

Burns 122 and 120, Rhododendron and rice straw, had SSAs of 0.809 and 0.890, indicating significant contribution from absorption although much less than the burns previously discussed (Figure 5-32 and Figure 5-43). DMA only size distributions were used for Burn 122 because the measured values of SSA_{scat_abs} were less than 0.85. Due to an apparent anomalous increase in particle concentration for large DMA sizes (Levin 2008), the DMA distributions were limited to sizes less than 0.4 μm. This anomalous increase was also present for the DMA measured sized distributions for burn 120 that were aligned with the OPC measured distributions; this likely increases the error in the aligned distribution.

Merit function values of 0.074 and 0.036 with refractive indices of $m = 1.534 \pm 0.011 + i0.029 \pm 0.009$ and $m = 1.395 \pm 0.034 + i0.010 \pm 0.018$ were retrieved for burns 122 and 120 (Figure 5-33 and Figure 5-44). A comparison of calculated and measured values of extinction, scattering and absorption coefficients shows good agreement for scattering and absorption coefficients (Figure 5-34 and Figure 5-45). As would be expected, because method B was used, there is better agreement for scattering and absorption coefficients than for extinction coefficients. Plotting the refractive indices

retrieved over the entire burn (Figure 5-35 and Figure 5-46) shows a small variability in retrieved refractive index. For burn 122, the refractive indices (Figure 5-35) indicate a decrease in absorption as the burn began, with an increase in absorption halfway through the burn; this relationship is also seen in the timeline of SSA_{scat_abs} (Figure 5-36). The increase in absorption seen in the refractive index and SSA are evident in the timeline of the burn (Figure 5-32) where it can be seen that the absorption measured during the burn was steadily decreasing during the first half of the burn and seemed to reach a steady state value for the second half of the burn. The measured extinction coefficient also reflects this change and it shows a slight drop after the three first time periods. The number distributions do show an increase in mean particle size (Figure 5-7) but do not show the dramatic change demonstrated by SSA. It is likely that the change in absorption is due to a change in NO_2 concentration in the chamber or composition of the aerosols.

Because a large portion of the volume distribution was not measured by the DMA for burn 122 the measured DMA volume distributions were fit with lognormal distributions. Aligned volume distributions for burn 120 may have been strongly influenced by anomalous data in upper DMA channels so DMA measured distributions were also fit with lognormal distributions. Single mode or bimodal lognormal distributions were fit to the DMA measured volume distributions for sizes less than 0.4 μm according to the methods described previously (*5.4 Burn 127, Chamise*). The fit distributions matched the measured distributions quite well except for larger particle sizes (Figure 5-37 and Figure 5-47) where the fit distribution underestimated the volume as seen previously for burn 127.

Using an assumed value of refractive index, $m = 1.5 \pm 0.01i$, particle extinction distributions were modeled for each of these burns. Modeled extinction distributions using the lognormal fit distributions were quite similar to those calculated using the measured distributions (Figure 5-38 and Figure 5-48) A residual between the two modeled extinction distributions (Figure 5-39 and Figure 5-49) shows the large discrepancy at larger diameters with good agreement at lower diameters. The particle extinction distributions and corresponding residuals demonstrated that our fit distributions were able to capture most of the measured particle extinction distribution as well as provide a significant amount of new information about the particle extinction distribution.

The index of refraction retrieval was rerun using the fit lognormal distributions. Merit function values of 1.217 and 0.383 were obtained for (Figure 5-40 and Figure 5-50) refractive indices of $m = 1.609 \pm 0.015 + i0.027 \pm 0.002$ and $m = 1.722 \pm 0.015 + i0.0102 \pm 0.001$. *C*alculated and measured extinction, scattering and absorption (Figure 5-41 and Figure 5-51) were also compared and showed slightly worse agreement between measured and calculated values of extinction coefficient. Merit functions retrieved using the fit lognormal distributions are much larger than those retrieved using the measured size distributions, 0.074 and 0.036. Retrieved refractive indices using the fit distributions had higher values of n than those retrieved using the measured distributions (Figure 5-42 and Figure 5-52); the retrieved value of k was similar using measured or fit size distributions

By fitting the volume distributions, we were able to capture missing extinction, scattering and absorption information for large particle sizes. Burns 120 and 122

demonstrated slightly better agreement between measured and calculated values of extinction, scattering and absorption coefficients using the refractive index refractive index from the fit lognormal size distributions, although the merit functions were larger. It will be assumed that the information gained using the fit lognormal size distributions produces refractive indices which are a better representative of the true refractive index.

5.7 Burn 128, black needlerush and Burn 133, Alaskan white spruce

Burns 128 and 133, black needlerush and Alaskan white spruce, had SSA values of 0.900 and 0.910, indicating very little contribution from absorption (Figure 5-53 and Figure 5-57). Merit function values of 0.030 and 0.098 and refractive indices of $m = 1.624 \pm 0.083 + i0.021 \pm 0.021$ and $m = 1.477 \pm 0.019 + i0.010 \pm 0.010$ were retrieved for burns 128 and 133 (Figure 5-54 and Figure 5-58). DMA measured size distributions were used for Burn 133 due to the saturation of the OPC. Almost the entire volume distribution was measured by the DMA. There was good agreement between measured and calculated values of extinction and scattering coefficients using the retrieved refractive indices (Figure 5-55 and Figure 5-59); extinction coefficients did not agree as well as scattering and absorption coefficients for burn 128. Individual refractive indices retrieved agreed well with those retrieved for the burn as a whole (Figure 5-56 and Figure 5-60). The refractive indices retrieved for these burns showed very good agreement between calculated and measured values of scattering and absorption coefficients.

5.8 Comparison to literature

The FLAME2 study was fairly unique among biomass studies because of the large number and variety of fuel types burned during the study. In the literature, average

refractive indices or SSA values are often categorized according to type of fuel burned, the FLAME2 study data will yield information on whether this is a good method of categorization. A comparison of our values with literature reported values will help extend the list of values of biomass optical properties and help deduce a proper way to categorize the optical properties.

5.9 SSA

Retrieved values of SSA were compared to values found in the literature for biomass smoke, most of which were obtained in the ambient atmosphere and probably included water in the aerosol phases unlike the FLAME2 data. Literature values of SSA are listed in Table 5.2 for a range of wavelengths near 532 nm and for a variety of combustion conditions and fuel types. Combustion phases indicated are flaming, smoldering, a mix of flaming and smoldering, and aged ambient smokes. For comparison SSA_{scat_abs} values measured for this study are listed in Table 5.3 with their corresponding fuel types. Suggested values of SSA for three broad fuel types (grass/savanna, tropical forest and temperate and boreal) are listed for both fresh and aged smokes in Table 5.4 [*Reid et al.*, 2005].

Table 5.2 *Literature values of SSA for biomass smoke. The phase of combustion is indicated with L – laboratory, A – aged, F – flaming, S – smoldering, M – mixed.*

Reference	Wavelength [nm]	SSA	Phase	Type
[*Hobbs et al.*, 1996]	540	0.85 ± 0.03	F	Temperate and Boreal
[*Hobbs et al.*, 1996]	550	0.90 ± 0.06	M	Temperate and Boreal
[*Hobbs et al.*, 1996]	540	0.97 ± 0.02	S	Temperate and Boreal
[*Miller and O'Neill*, 1997]	550	0.7	F	Temperate and Boreal
[*Radke et al.*, 1991]	540	0.83 ± 0.11	M	Temperate and Boreal
[*Radke et al.*, 1988]	550	0.86 ± 0.11	M	Temperate and Boreal
[*Dubovik et al.*, 2002]	440/670	0.94/0.935 ± 0.02	A	Temperate and Boreal
[*Colarco et al.*, 2004]	550	0.93 ± 0.01	A	Temperate and Boreal
[*Chen et al.*, 2006]	532	0.32/0.6	F/S	Temperate and Boreal
[*Chen et al.*, 2006]	532	0.75/0.99	F/S	Temperate and Boreal
[*Reid and Hobbs*, 1998]	550	0.74 ± 0.06	F	Tropical Forest
[*Reid and Hobbs*, 1998]	550	0.84 ± 0.02	S	Tropical Forest
[*Dubovik et al.*, 2002]	440/670	0.94/0.93 ± 0.02	A	Tropical Forest
[*Procopio et al.*, 2003]	440/670	0.93/0.90 ± 0.01	A	Tropical Forest
[*Guyon et al.*, 2003]	550	0.90 ± 0.03, 0.91 ± 0.02	A	Tropical Forest
[*Kuzmanoski et al.*, 2007]	500	0.91	A	Tropical Forest
[*Kuzmanoski et al.*, 2007]	500	0.88	A	Tropical Forest
[*Reid and Hobbs*, 1998]	550	0.77 ± 0.03	F	Scrub Forest/Cerrado
[*Dubovik et al.*, 2002]	440/670	0.91/0.89 ± 0.03	A	Scrub Forest/Cerrado
[*Abel et al.*, 2003]	559	0.84	F	Grasslands/Savanna
[*Reid and Hobbs*, 1998]	550	0.76 ± 0.08	F	Grasslands/Savanna
[*Dubovik et al.*, 2002]	440/670	0.88/0.84 ± 0.015	A	Grasslands/Savanna
[*Hungershoefer et al.*, 2008]	550	0.945 ± 0.004	M	Grasslands/Savanna
[*Hungershoefer et al.*, 2008]	550	0.950 ± 0.02	M	Grasslands/Savanna
[*Patterson and McMahon*, 1984]	550	0.74 ± 0.06	L	Laboratory

Table 5.3 *Measured SSA values for the FLAME2 chamber study listed by fuel type.*

Burn number	Fuel	Measured SSA_{scat_abs}	Fuel Type
120	Rice straw	0.890 ± 0.004	Asian fuel
132	Chinese sugarcane	0.696 ± 0.007	Asian fuel
127	Chamise	0.429 ± 0.005	desert shrub
129	Sagebrush	0.701 ± 0.007	desert shrub
121	Alaskan duff	0.970 ± 0.001	duff
125	Alaskan duff	0.990 ± 0.001	duff
114	Black needlerush	0.918 ± 0.004	grass
126	Florida wiregrass	0.853 ± 0.005	grass
128	Black needlerush	0.900 ± 0.004	grass
118	Florida coastal palmetto	0.428 ± 0.005	southeastern shrub
119	Mississippi palmetto	0.615 ± 0.007	southeastern shrub
122	Rhododendron leaves	0.809 ± 0.006	southeastern shrub
131	Gallberry	0.446 ± 0.006	southeastern shrub
116	Douglas fir	0.527 ± 0.007	tree
117	Douglas fir	0.958 ± 0.002	tree
123	Alaskan black spruce	0.666 ± 0.008	tree
124	Douglas fir	0.975 ± 0.001	tree
130	Longleaf pine	0.951 ± 0.002	tree
133	Alaskan white spruce	0.910 ± 0.004	tree
115	Oak and hickory	0.852 ± 0.005	trees
113	Longleaf pine and wiregrass	0.934 ± 0.003	trees and grass

Table 5.4 *Suggested SSA values suggested by Reid [2005] for various fuel types both aged and fresh at* λ *= 550 nm.*

SSA	Phase	Fuel type
0.821 ± 0.05	Fresh	grass/savanna
0.86 ± 0.05	Aged	grass/savanna
0.85 ± 0.05	Fresh	tropical forest
0.89 ± 0.05	Aged	tropical forest
0.88 ± 0.05	Fresh	temperate/boreal
0.915 ± 0.05	Aged	temperate/boreal

All of the SSA values listed in Table 5.2, Table 5.3 and Table 5.4 were plotted and categorized according to fuel type (Figure 5-61). SSA_{scat_abs} values measured in this study were categorized according to the broad fuel types in Table 5.2 where trees were put into the temperate/boreal category, desert shrubs were categorized as scrub forest/cerrado, grasses were put into the grass/savanna category, and southeastern shrubs, duff and Asian fuels were listed as "Other". SSAs in each category cover a very wide range of values, though SSAs listed as tropical fuels cover the smallest range. Values

suggested by Reid for fresh and aged smokes for the different fuel types do not agree well with the average of the measured SSAs except for tropical fuels [*Reid et al.*, 2005]. Measured SSA_{scat_abs} fall in the range of the literature values of SSA for each fuel type, except for chamise and sagebrush which are much lower than the other three SSA values listed for scrub forest/cerrado.

SSA values reported in the literature and from this study for biomass fuels cover a very wide range, from 0.32 up to 1 with an average value of 0.813. It does not appear that fuel type is a good categorization technique for SSA so measured SSAs were also categorized according to combustion conditions (Figure 5-62). Although it is apparent that there is still a broad range of SSA for each combustion type, there are slightly narrower ranges for flaming, smoldering and aged smokes. Flaming smokes appear to have the smallest SSA values with an average of 0.716 ± 0.168, smoldering smokes have larger SSA values at 0.850 ± 0.180 and aged smokes smallest range and highest SSAs at 0.913 ± 0.022. As mixed phase smokes contain both flaming and smoldering it is logical that the average SSA for these smokes lies between those of flaming and smoldering at 0.799 ± 0.183; mixed combustion type fuels also cover the widest range of SSA values, from 0.45 to 1.

Studies have shown that the fraction of CO emitted during a fire can be highly dependent on the combustion conditions of the fire such that smoldering fires produce more CO than flaming fires [*Crutzen and Andreae*, 1990]. The modified combustion efficiency (MCE), the ratio of CO_2 to CO_2 + CO present in the smoke, has been shown to be a good indicator of the combustion conditions during a fire. Lower values of MCE indicate smoldering type conditions and large values indicate flaming [*McMeeking*,

2008]. FLAME2 burns in Figure 5-62 were shaded according to the measured MCE for those burns. Unfortunately there does not appear to be any clear dependence of SSA on MCE.

Values of SSA_{scat_abs} from FLAME2 are similar to those reported in the literature for flaming, smoldering, mixed and aged smokes from biomass burning. SSA appears to depend more strongly on combustion conditions than fuel type although there was not a strong dependence of FLAME2 SSA values on MCE. Aged smokes produced the highest and most narrow range of SSA values. This is likely due to the aging process the smoke plumes undergo in the atmosphere; the relatively high SSAs of the aged plumes are probably influenced by the smoke plume interacting with water in the atmosphere.

5.10 Refractive index

Refractive indices retrieved from FLAME2 and those reported in the literature for biomass smokes were also compared. Refractive indices from literature are reported for wavelengths near 532 nm and a variety of fuel types in Table 5.5. The largest difference between retrieved refractive indices is the technique that was used to retrieve the refractive index. Most of the studies listed in Table 5.5 retrieve the refractive index from models using aerosol radiance measurements, while two of the studies [*Guyon et al.*, 2003; *Hungershoefer et al.*, 2008] used techniques similar to this study using size distributions, scattering, absorption and Mie theory to find refractive index.

Table 5.5 *Literature values of refractive index for biomass smoke. Phase of combustion is indicated by L – laboratory tests, A – aged plumes, F – flaming, S – smoldering.*

Reference	***Wavelength [nm]***	***RI***	***Phase***	***Fuel type***	***Technique***
[*Westphal and Toon*, 1991]	500	1.45 - 1.55; 0.01i	L	Boreal forest	Meteorology, aerosol and radiative transfer model
[*Yamasoe et al.*, 1998]	440	1.53 ± 0.04	A	Cerrado	Sky radiance (AERONET radiometers)
[*Yamasoe et al.*, 1998]	670	1.55 ± 0.04	A	Cerrado	Sky radiance (AERONET radiometers)
[*von Hoyningen-Huene et al.*, 1999]	560 - 870	1.45 (1.37 - 1.55)	A	Tropical forest	Sky brightness (CIRATRA radiometers)
[*Dubovik et al.*, 2002]	440 - 1020	1.47 ± 0.03 + i0.0093 ± 0.003	A	Tropical forest	Sky radiance (AERONET radiometers)
[*Dubovik et al.*, 2002]	440 - 1020	1.52 ± 0.01 + i0.015 ± 0.004	A	Cerrado	Sky radiance (AERONET radiometers)
[*Dubovik et al.*, 2002]	440 - 1020	1.51 ± 0.01 + i0.021 ± 0.004	A	Savanna	Sky radiance (AERONET radiometers)
[*Dubovik et al.*, 2002]	440 - 1020	1.50 ± 0.04 + i0.0094 ± 0.003	A	Boreal forest	Sky radiance (AERONET radiometers)
[*Guyon et al.*, 2003]	545	1.41 ± 0.05 + i0.013 ± 0.005	A	Tropical forest	OPC (PCASP)/Neph/PAS/iteration
[*Procopio et al.*, 2003]	440 - 1020	1.50 ± 0.07 + 0.012 ± 0.006	A	Cerrado	Sky radiance (AERONET radiometers)
[*Colarco et al.*, 2004]	440	1.524 + 0.0056i	A	Boreal forest	AERONET Almucantar
[*Colarco et al.*, 2004]	670	1.554 + 0.0043i	A	Boreal forest	AERONET Almucantar
[*McMeeking et al.*, 2005]	632	1.577 ± 0.008	A	Temperate Forest	DMA/OPC alignment
[*Schkolnik et al.*, 2007]	545	1.49 + 0.013i	A	Tropical forest	DMA/APS/Neph/PSAP/Mie theory
[*Hungershoefer et al.*, 2008]	550	1.60 + 0.010i	F	Savanna grass	DMA/CPC/neph/PAS/Mie theory
[*Hungershoefer et al.*, 2008]	550	1.56 + 0.010i	F	Musasa	DMA/CPC/neph/PAS/Mie theory

Literature and FLAME2 retrieved refractive indices (Table 5.6) were plotted (Figure 5-63) to more easily compare the retrieved values. Refractive indices retrieved from FLAME2 cover a wider range in values than the literature values, and some much larger values of the imaginary index of refraction *k*. As most of the previously reported refractive indices were retrieved for aged plumes, it is understandable that variability present in fresh smokes would decrease due to the atmospheric aging process. There does not appear to be a large dependence of fuel type on refractive index, though it is possible that a stronger dependence could be evident in a larger number of samples.

5.11 FLAME2 conclusions

After the appropriate corrections were made to the data, good agreement between the CRD, PA and TSI nephelometer measurements of extinction, scattering and absorption coefficients was demonstrated for all the burns done during the FLAME2 chamber study with an $r^2 = 0.999$. Measurements of SSA_{ext_scat} and SSA_{scat_abs} fell on the 1-1 line indicating good closure between extinction, scattering and absorption measurements. The fuels burned during the FLAME2 chamber study showed a wide range of SSAs, yielding SSA values of 0.43 to 1 indicating a large variation in the contribution from absorption. A strong relationship was found between measurements of SSA_{scat_abs} and EC_a indicating a good relationship between EC_a and absorption. After manipulations were performed on the measured size distributions to give a better representation of the particles present, refractive indices were retrieved for six burns (Table 5.6).

Table 5.6 *Refractive indices retrieved for FLAME2 Chamber burns.*

ID	Fuel Type	Fit distribution	DMA only	DMA/OPC	SSA_{scat_abs}	$\chi 2/N^2$	*n*	*k*
120	Rice straw	•			0.890 ± 0.004	0.383	1.722 ± 0.015	0.012 ± 0.001
122	Rhododendron leaves	•			0.809 ± 0.006	1.217	1.609 ± 0.015	0.027 ± 0.002
127	Chamise	•			0.429 ± 0.005	0.370	1.365 ± 0.019	0.150 ± 0.007
128	Black needlerush			•	0.900 ± 0.004	0.030	1.624 ± 0.083	0.021 ± 0.021
129	Sagebrush		•		0.701 ± 0.007	0.102	1.432 ± 0.011	0.057 ± 0.012
133	Alaskan white spruce		•		0.910 ± 0.004	0.098	1.477 ± 0.019	0.010 ± 0.010

FLAME2 values of SSA were compared to literature values indicating good agreement. Measured values of SSA cover a wide range and appear to depend more on combustion conditions than fuel type. Refractive indices retrieved from FLAME2 were also compared to literature values but covered a wider range of values, most noticeably larger values of *k*. Fuel type did not appear to have a large impact on refractive index, though firm conclusions are not possible due to the small sample size.

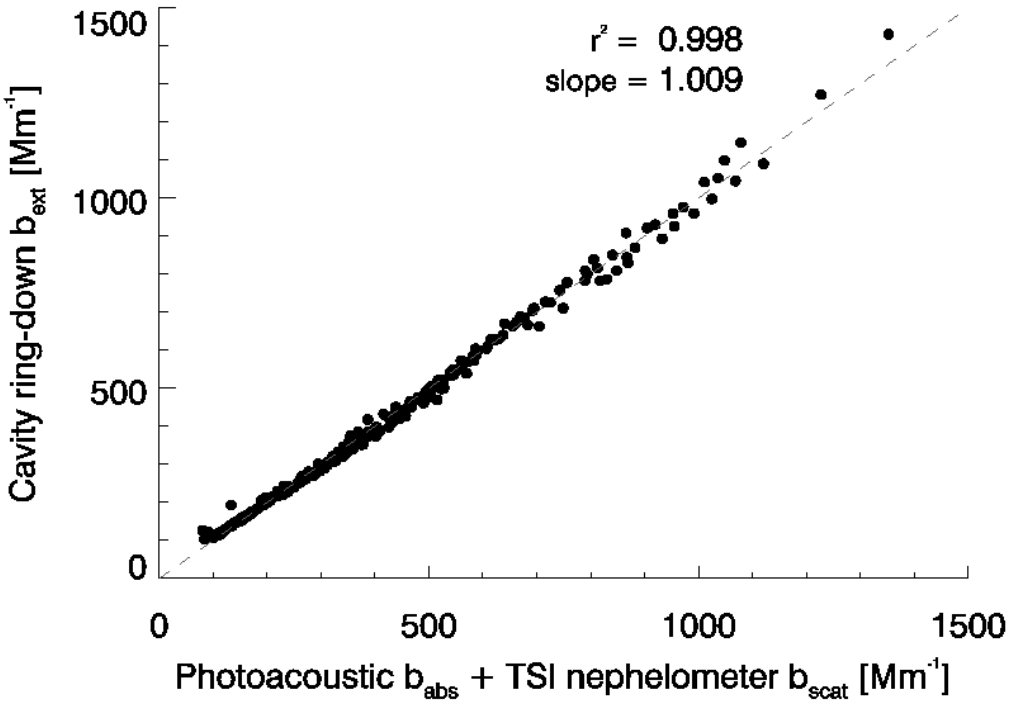

Figure 5-1 *Optical closure, as expressed by the r^2 value, between CRD measured extinction coefficients and the sum of the absorption and scattering coefficients measured by the PA and TSI nephelometer. Grey dashed line indicates 1-1 line.*

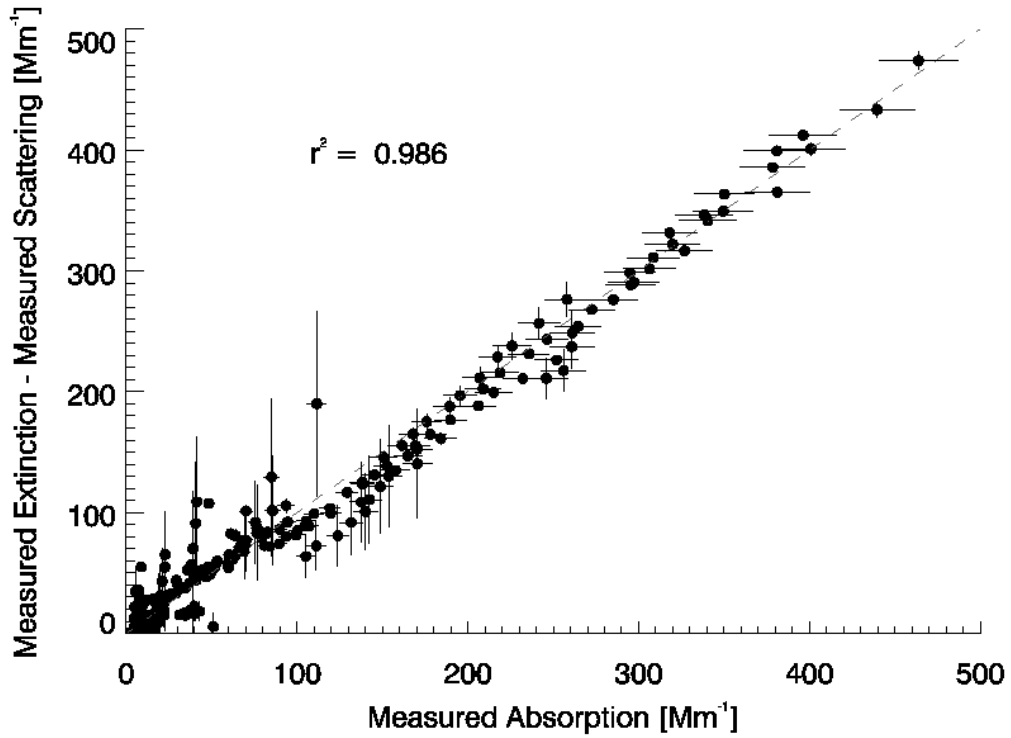

Figure 5-2 *Measured PAS absorption coefficients compared to absorption coefficients determined by the difference method for FLAME2. Grey dashed line indicates 1-1 line.*

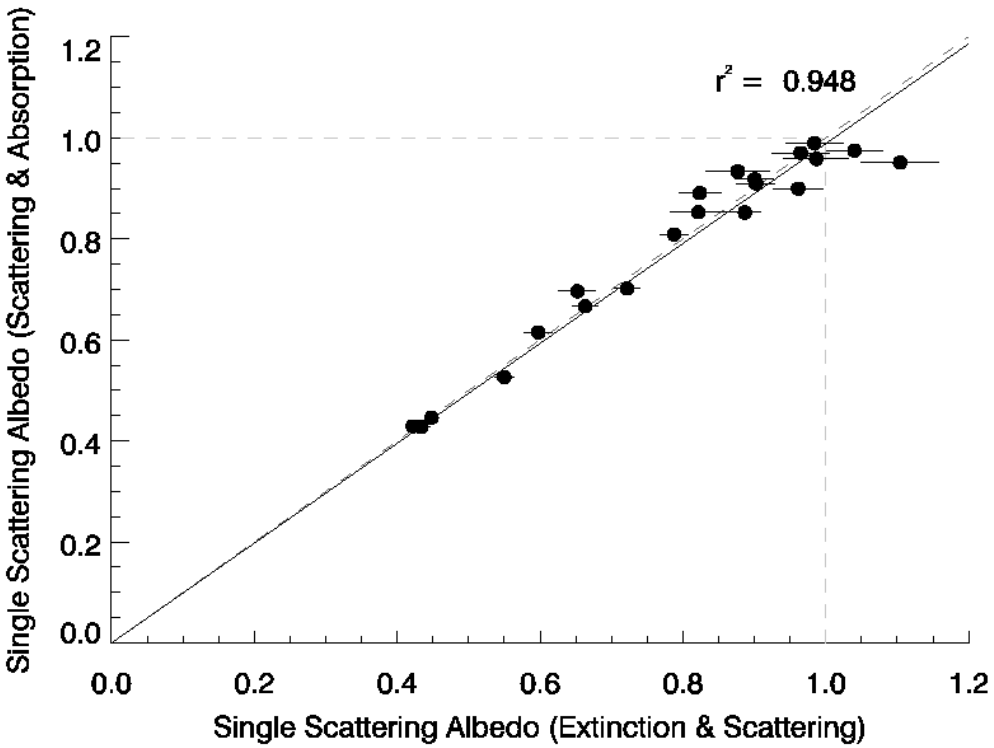

Figure 5-3 *Comparison of $SSA_{ext\ scat}$ and $SSA_{scat\ abs}$ for FLAME2.*

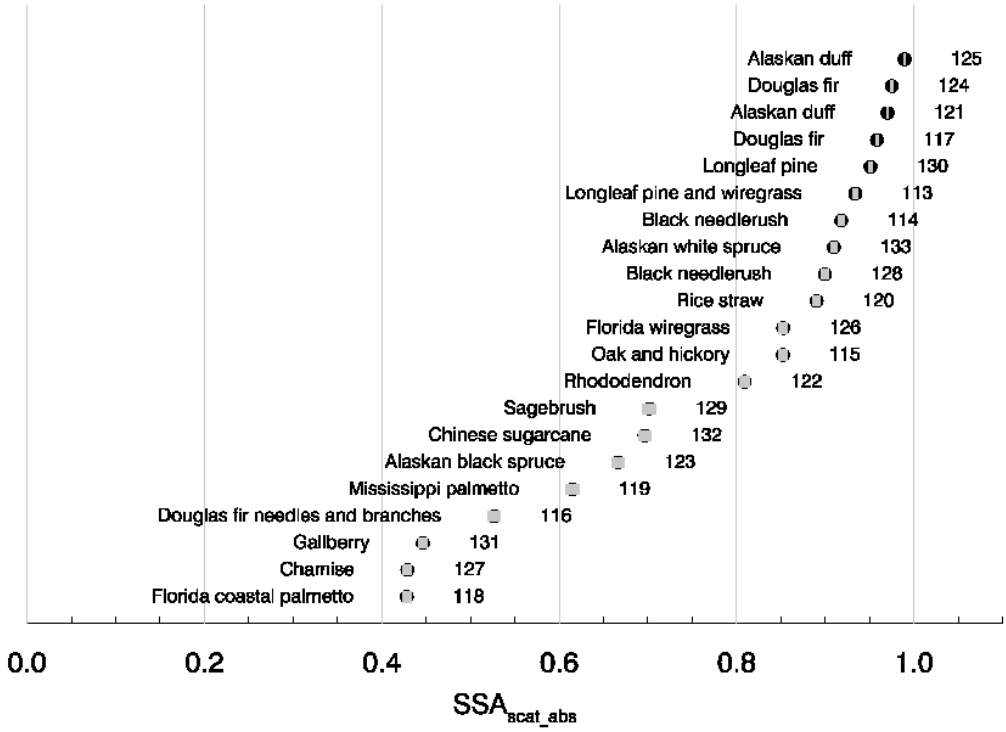

Figure 5-4 *Burns ordered according to SSA_{scat_abs}. The uncertainty is indicated by grey shading. Fuel types are listed to the left of each point and burn numbers are listed to the right. SSA shown here was calculated using scat/(scat+abs) measurements.*

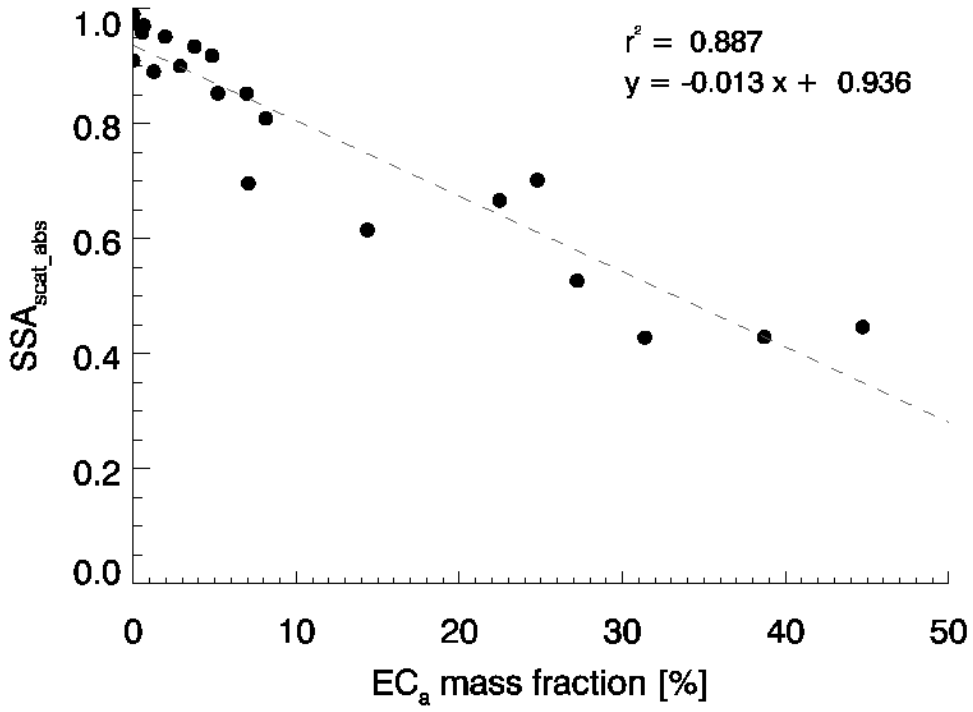

Figure 5-5 *Comparison of measured apparent EC fraction and SSA_{scat_abs} for the FLAME2 chamber study.*

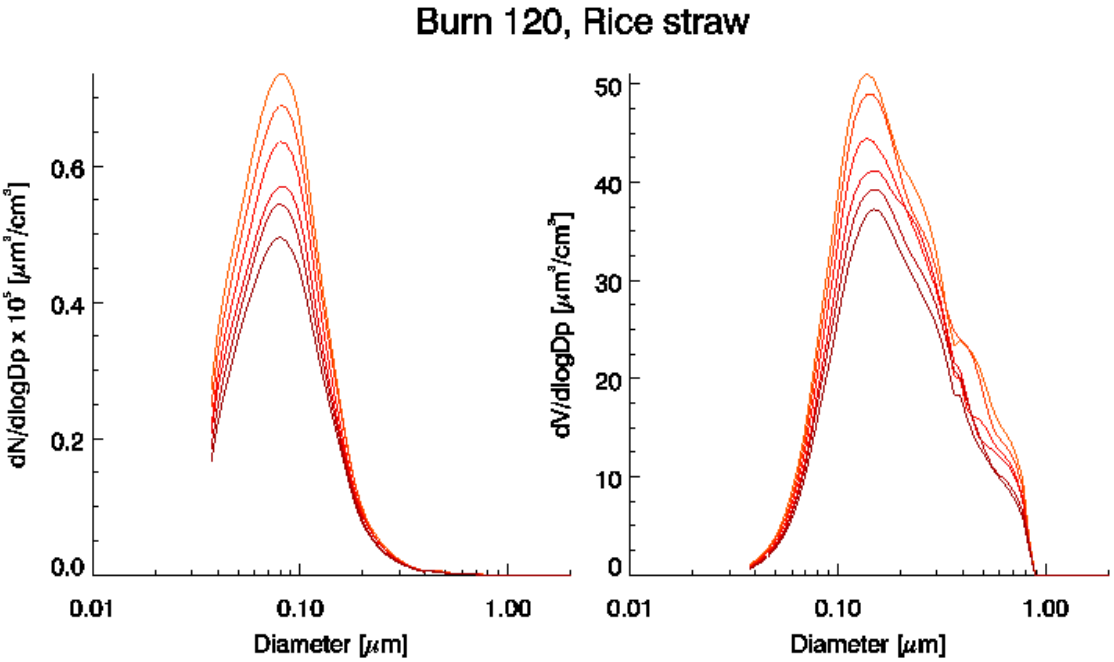

Figure 5-6 *Aerosol number and volume distributions for burn 120 Rice straw. Colors indicate time during the burn where blue is the beginning and red the end. Distributions are from alignment of DMA and OPC measured distributions.*

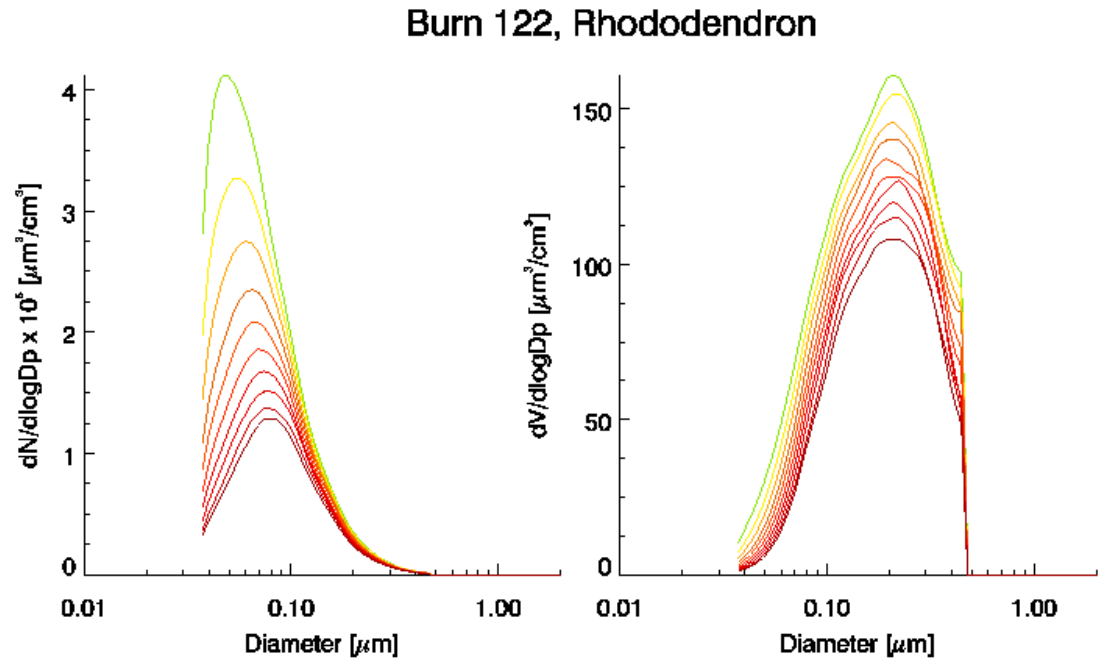

Figure 5-7 *Aerosol number and volume distributions for burn 122, rhododendron leaves. Colors indicate time during the burn where blue is the beginning and red the end. Distributions are DMA measured distributions cut off at 0.47 μm.*

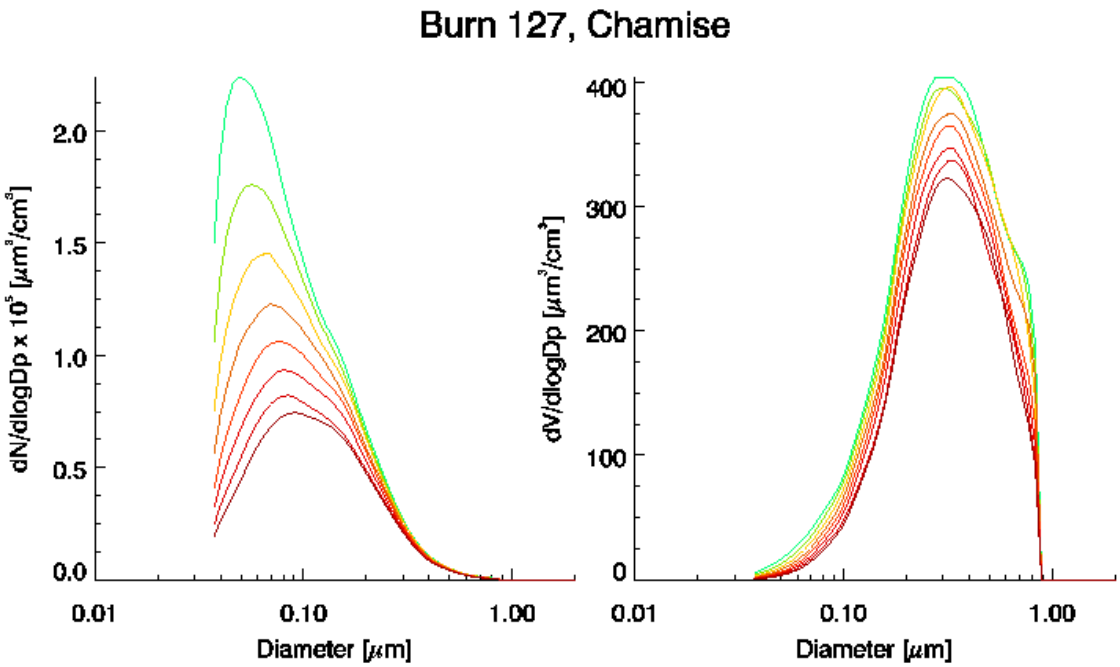

Figure 5-8 *Aerosol number and volume distributions for burn 127, chamise. Colors indicate time during the burn where blue is the beginning and red the end. Distributions are from DMA only.*

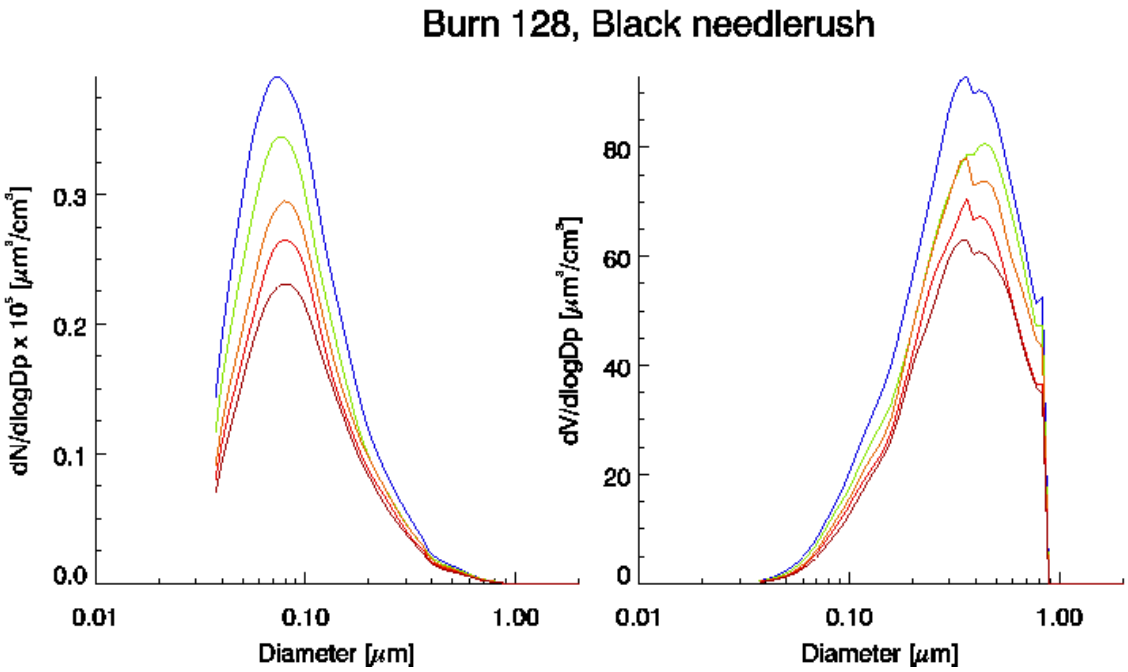

Figure 5-9 *Aerosol number and volume distributions for burn 128, black needlerush. Colors indicate time during the burn where blue is the beginning and red the end. Distributions are from alignment of DMA and OPC measured distributions.*

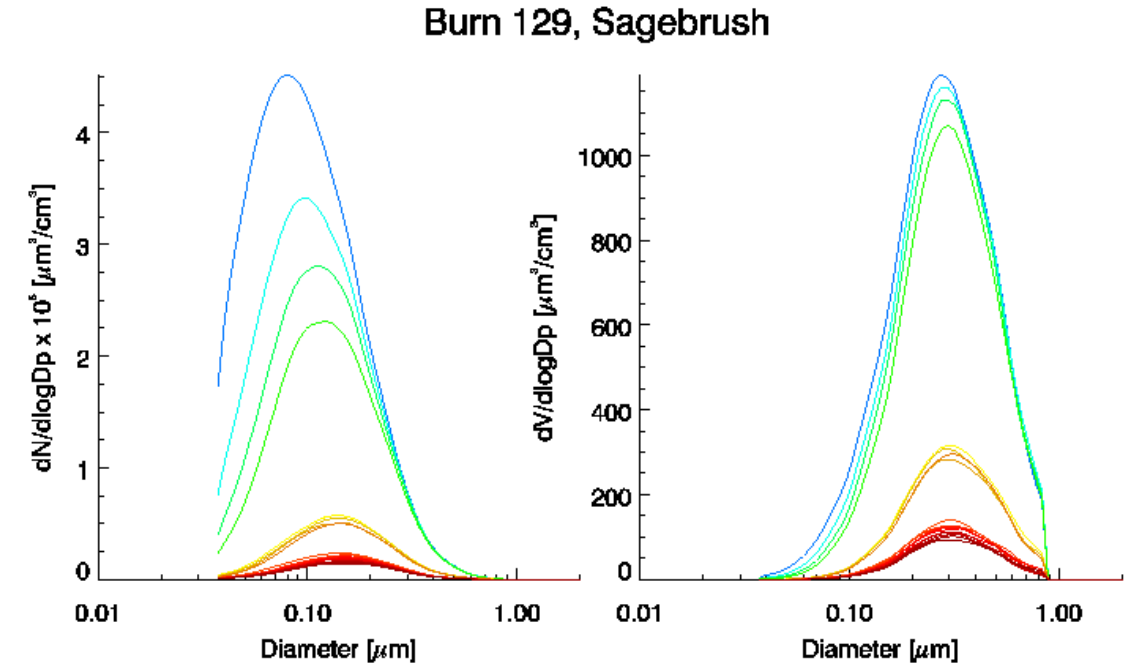

Figure 5-10 *Aerosol number and volume distributions for burn 129, sagebrush. Colors indicate time during the burn where blue is the beginning and red the end. Distributions are from DMA only.*

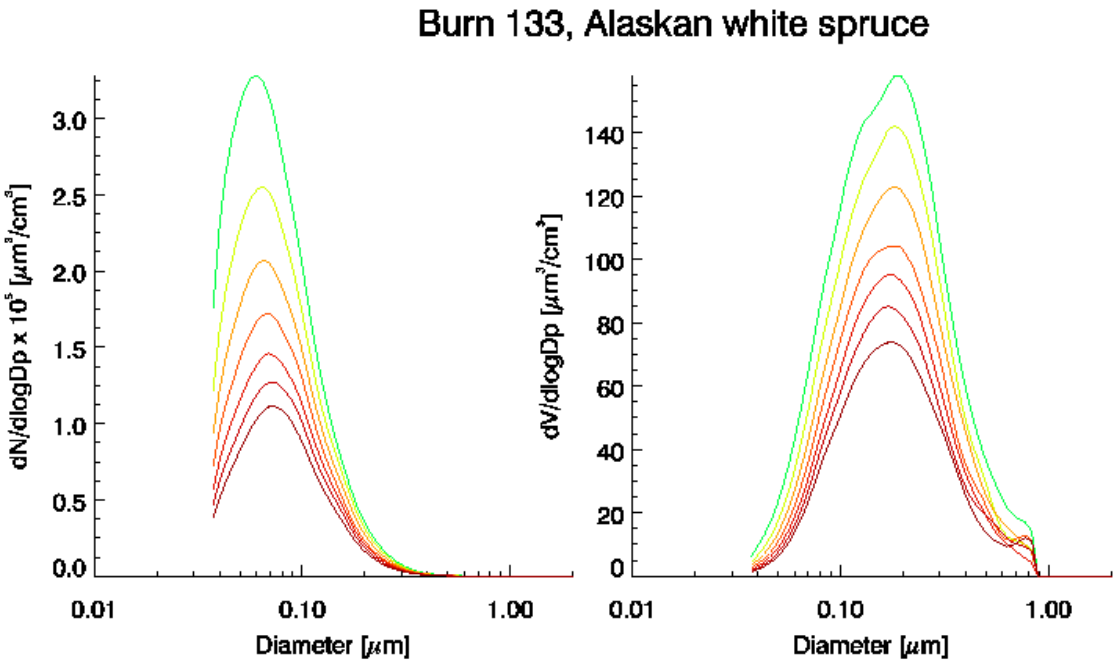

Figure 5-11 *Aerosol number and volume distributions for burn 133, Alaskan white spruce. Colors indicate time during the burn where blue is the beginning and red the end. Distributions are from DMA only.*

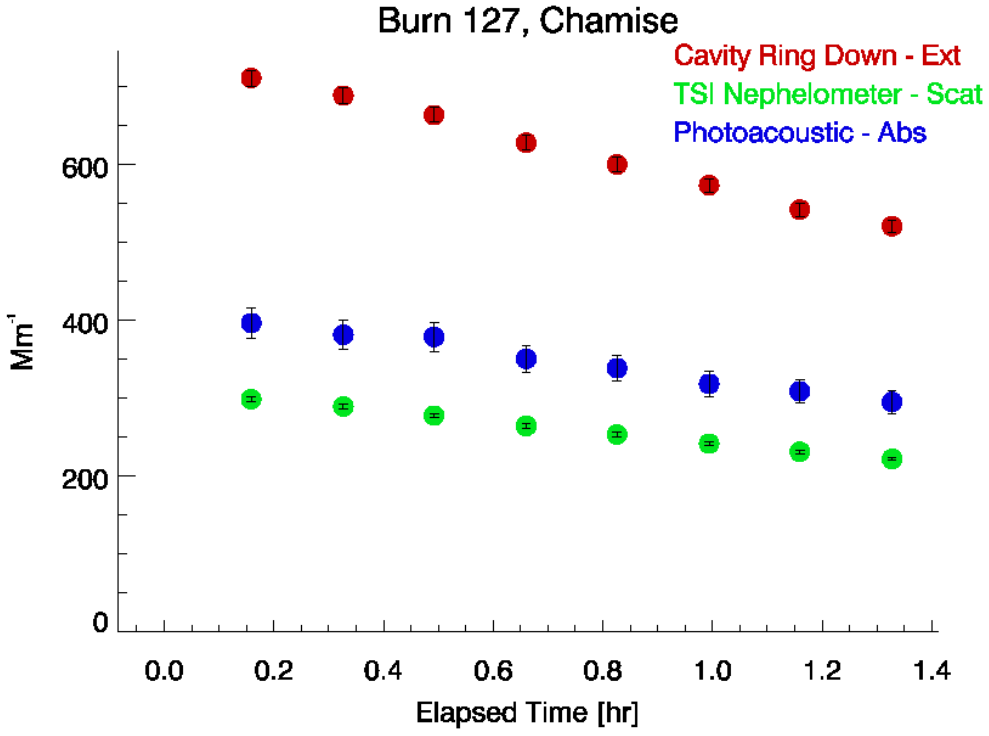

Figure 5-12 *Timeline of extinction, scattering and absorption coefficients for burn 127, chamise.*

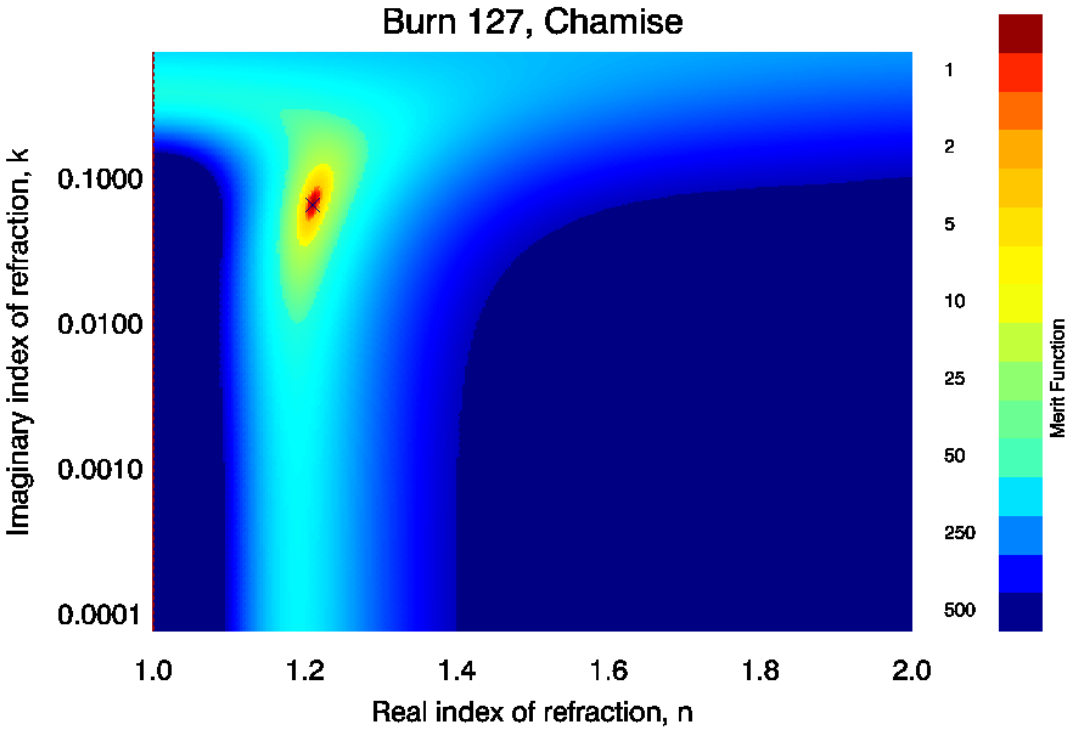

Figure 5-13 *Merit function for burn 127, chamise, over range of index of refraction. Minimum merit function was 0.107. The retrieved refractive index is indicated by the cross.*

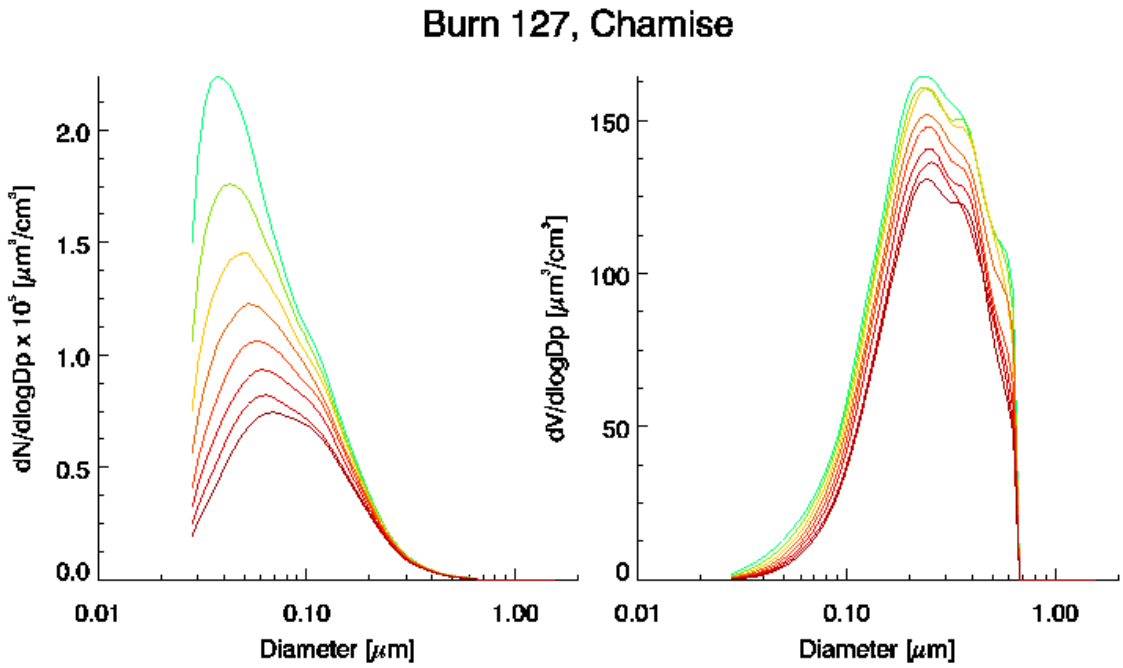

Figure 5-14 *DMA measured volume distributions for burn 127, chamise, shifted by a shape factor of 1.32.*

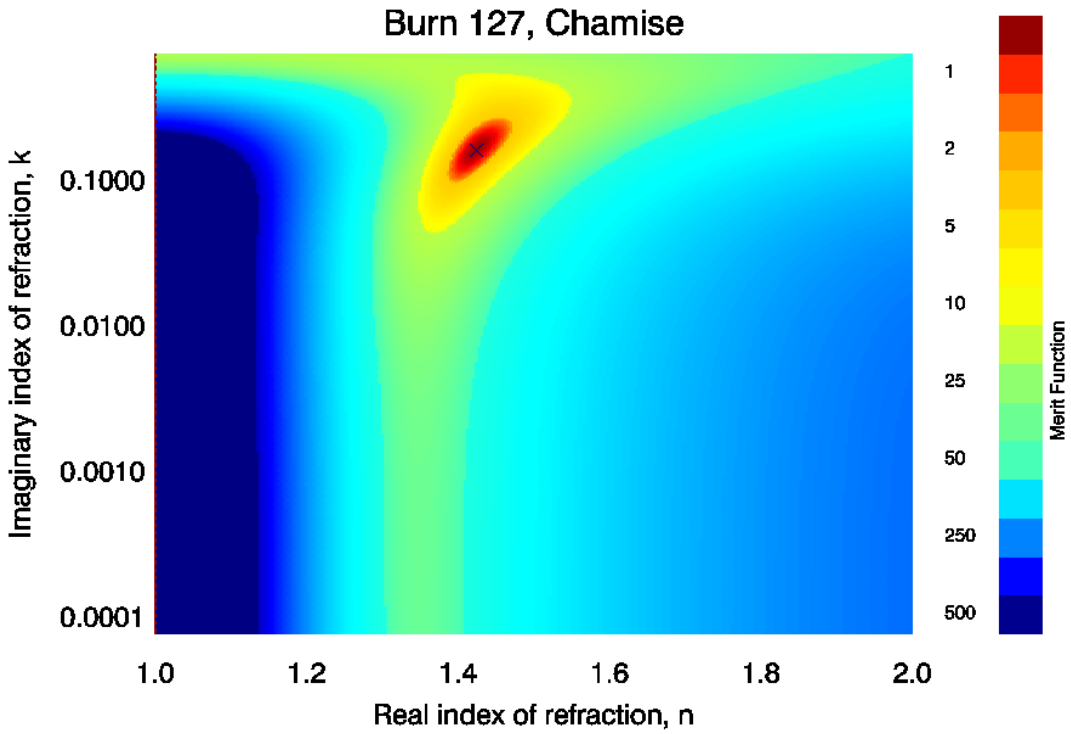

Figure 5-15 *Merit function for burn 127, chamise, using the shifted DMA measured size distribution. The minimum merit function was 0.030. The retrieved refractive index is indicated by the cross*

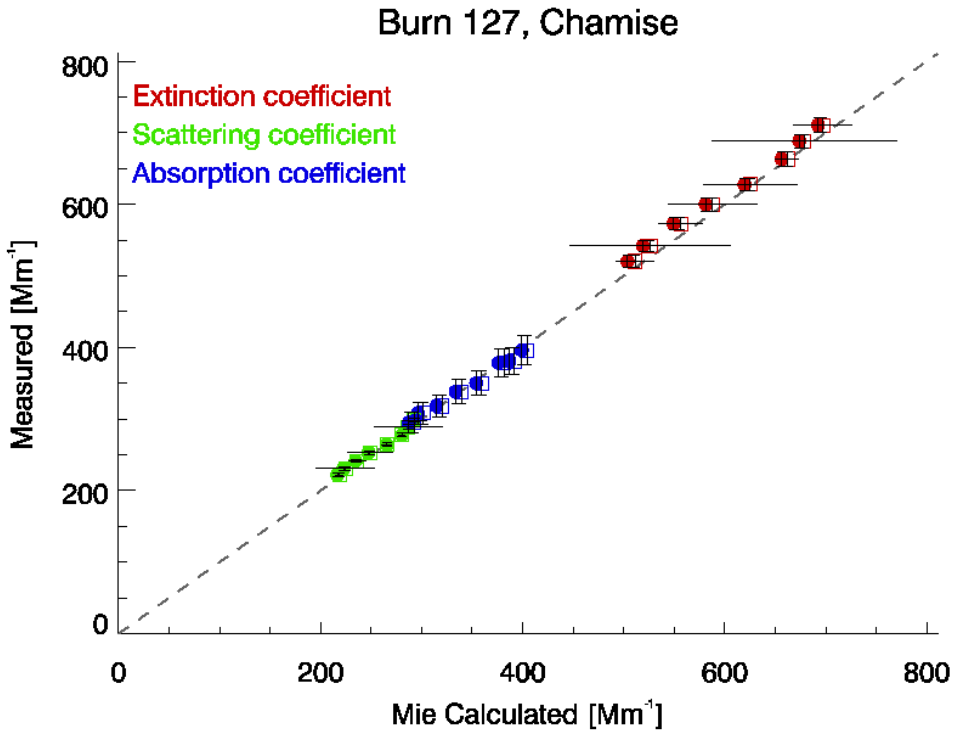

Figure 5-16 *Comparison of measured and calculated values of extinction, scattering and absorption coefficient for burn 127, chamise. Calculated values are based on retrieved refractive indices where the solid symbols indicate refractive indices retrieved using measured size distributions, and open symbols indicate refractive indices retrieved using shifted DMA measured size distributions.*

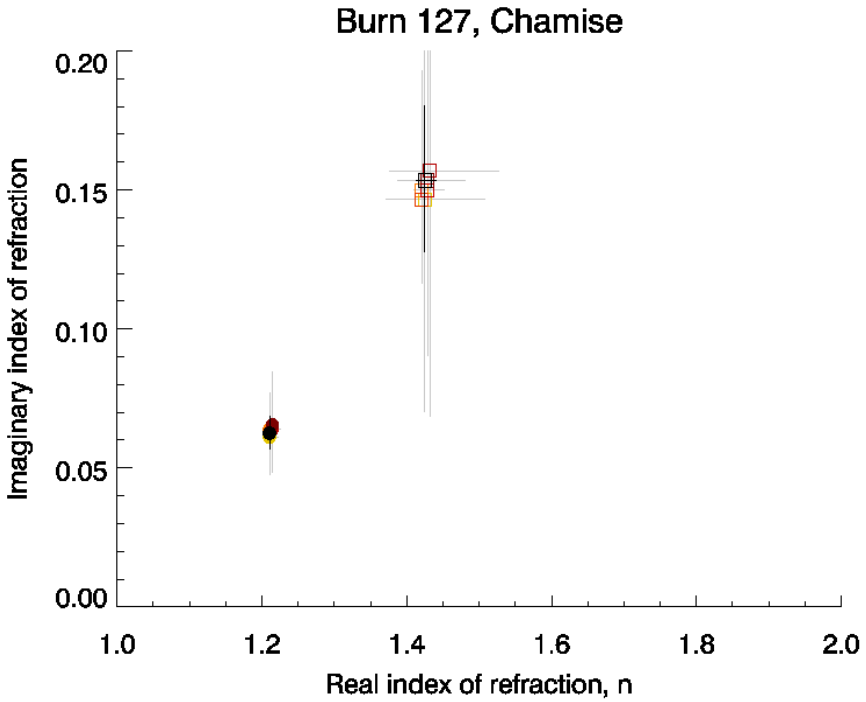

Figure 5-17 *Refractive indices retrieved for burn 127, chamise. The black points indicate the refractive indices retrieved minimizing the error over the entire burn. The colored points indicated refractive indices retrieved for each time period of the burn. Colors indicate time during the burn where blue is the beginning and red the end. Solid symbols indicate refractive indices retrieved using measured size distributions. Open symbols indicate refractive indices retrieved using shifted DMA measured size distributions.*

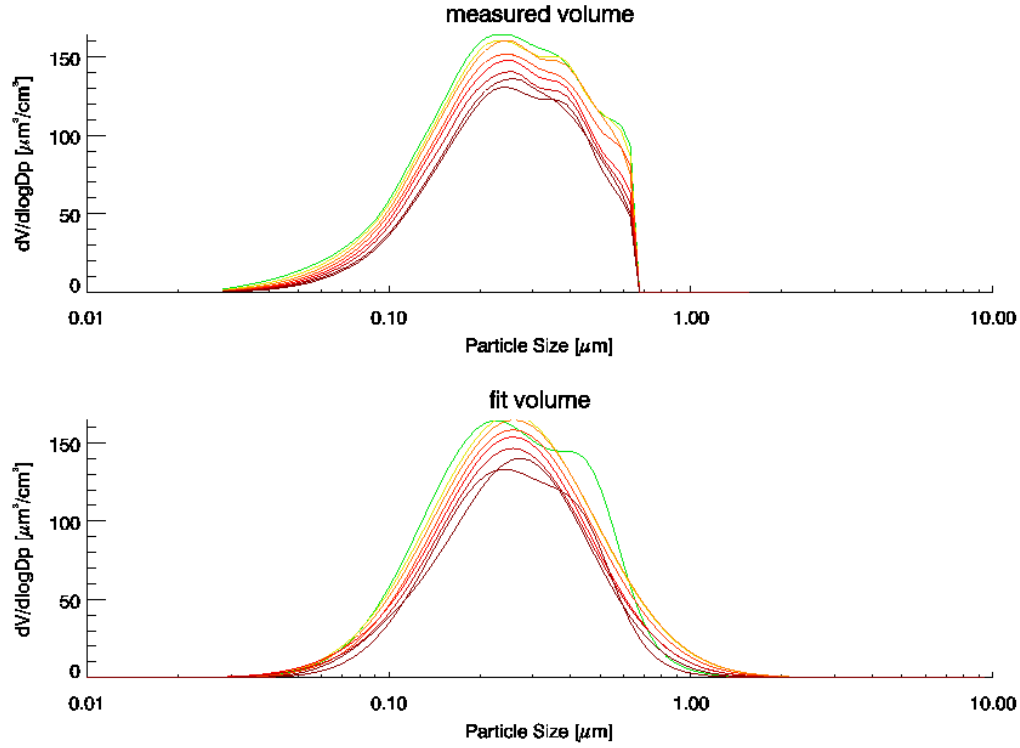

Figure 5-18 *Measured and lognormal fit size distributions for burn 127, chamise.*

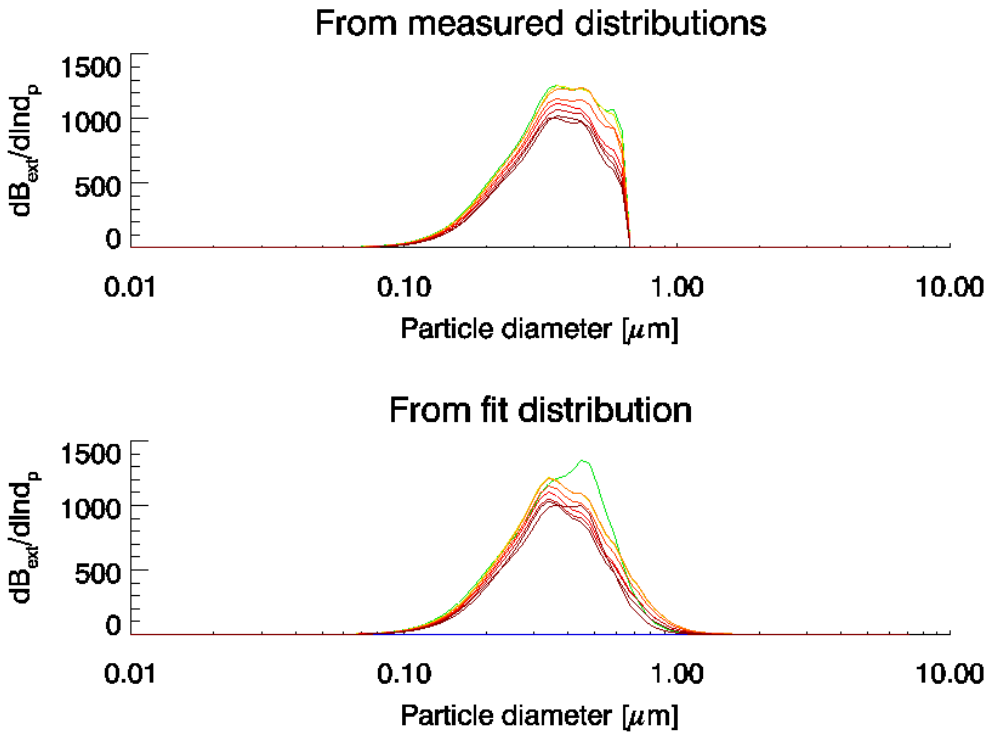

Figure 5-19 *Calculated extinction distributions for burn 127, chamise.*

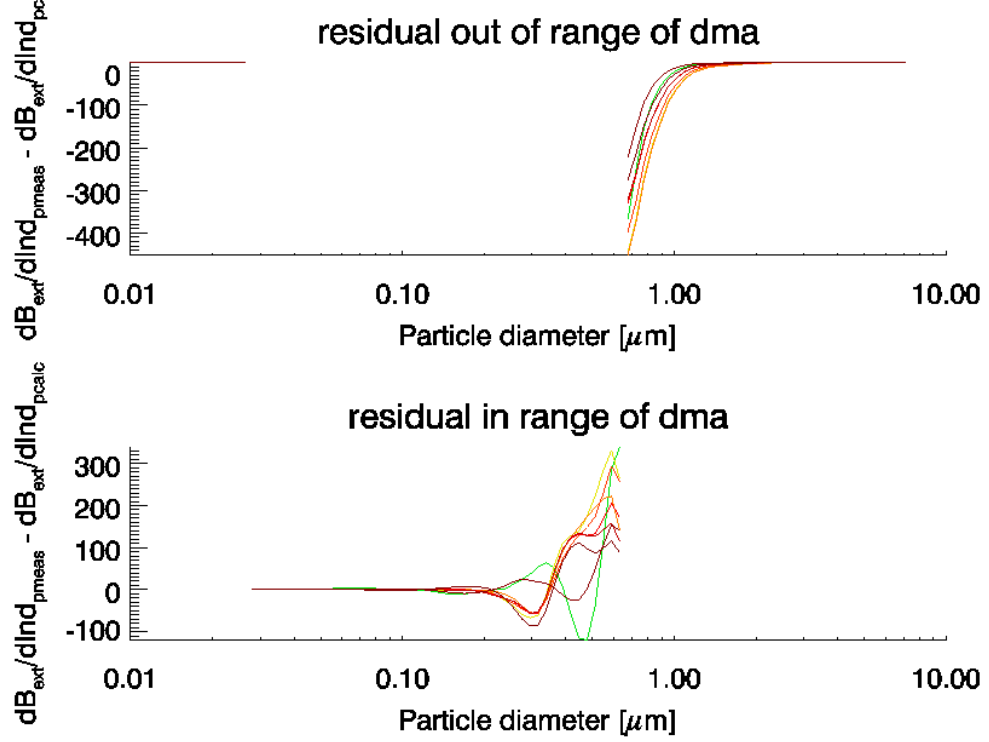

Figure 5-20 *Residual of extinction distribution for burn 127, chamise. The top plot indicates the extra extinction information gained by the fit distribution; the lower plot indicates the error between the fit and measured distributions.*

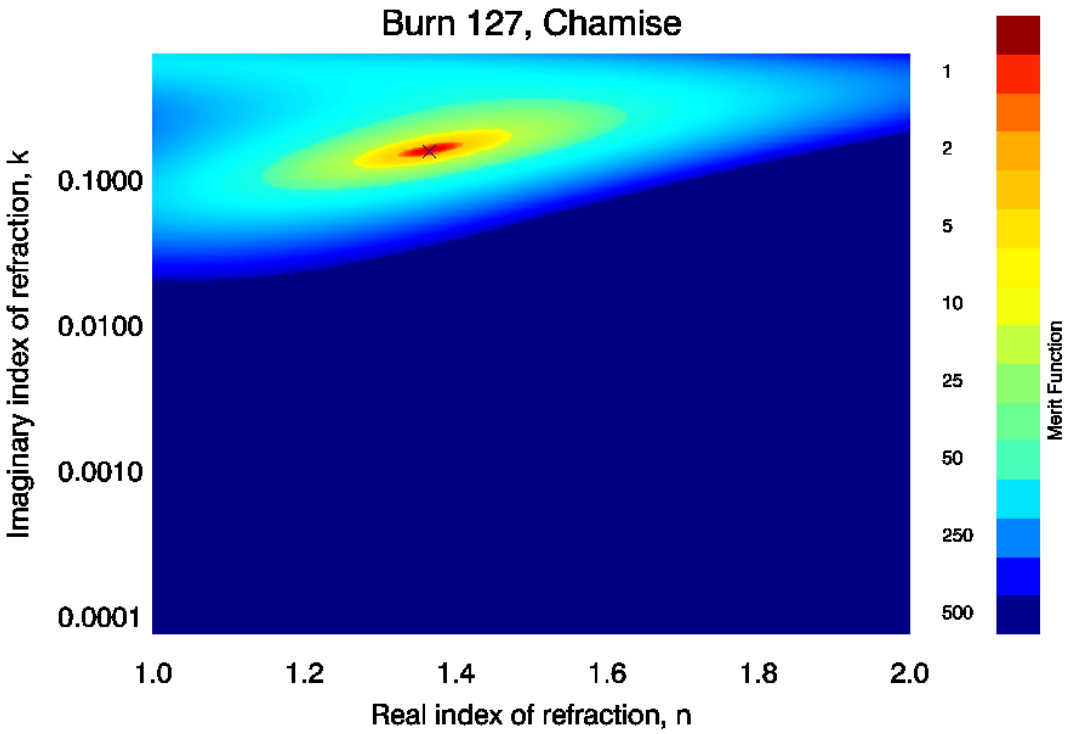

Figure 5-21 *Merit function for burn 127, chamise, using the fit lognormal size distribution. The minimum merit function was 0.370. The retrieved refractive index is indicated by the cross.*

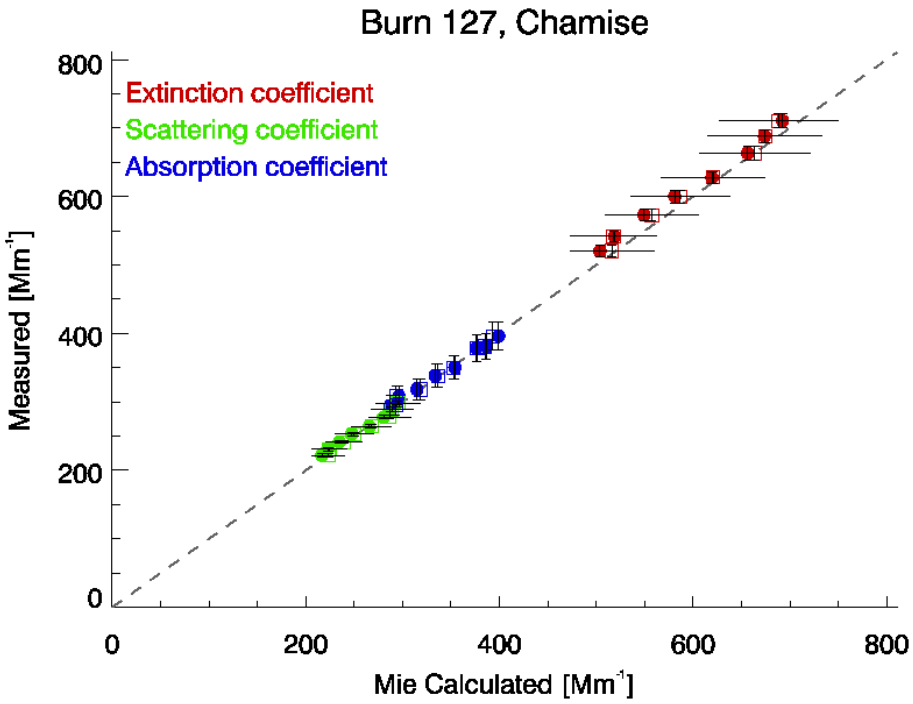

Figure 5-22 *Comparison of measured and calculated values of extinction, scattering and absorption coefficient for burn 127, chamise. Calculated values are based on retrieved refractive indices where the solid symbols indicate refractive indices retrieved using measured size distributions and open symbols indicate refractive indices retrieved using fit lognormal size distributions.*

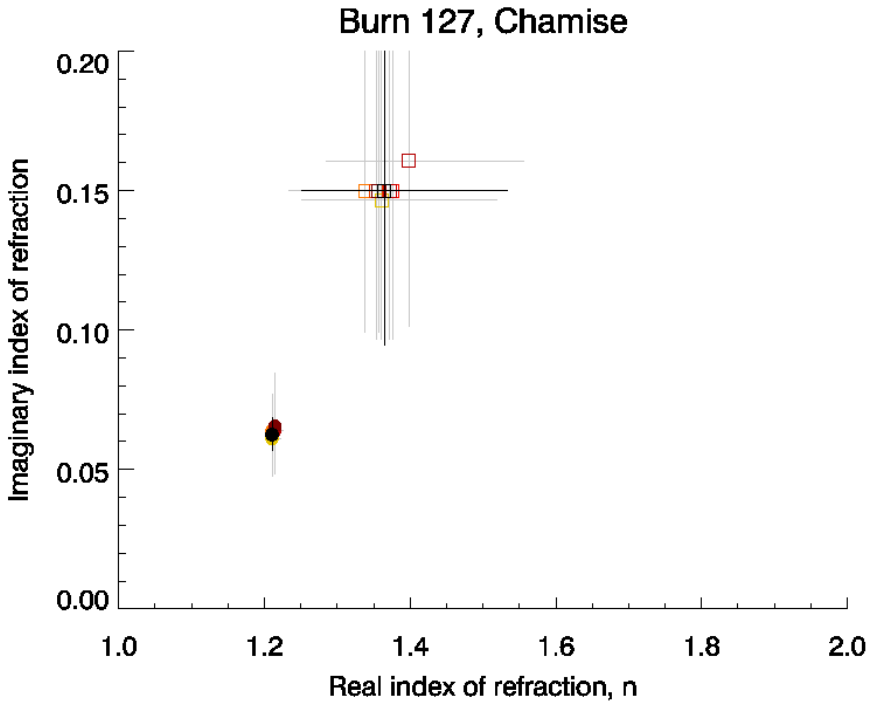

Figure 5-23 *Refractive indices retrieved for burn 127, chamise. The black points indicate the refractive indices retrieved minimizing the error over the entire burn. The colored points indicated refractive indices retrieved for each time period of the burn. Colors indicate time during the burn where blue is the beginning and red the end. Solid symbols indicate refractive indices retrieved using measured size distributions, open symbols indicate refractive indices retrieved using fit lognormal size distributions.*

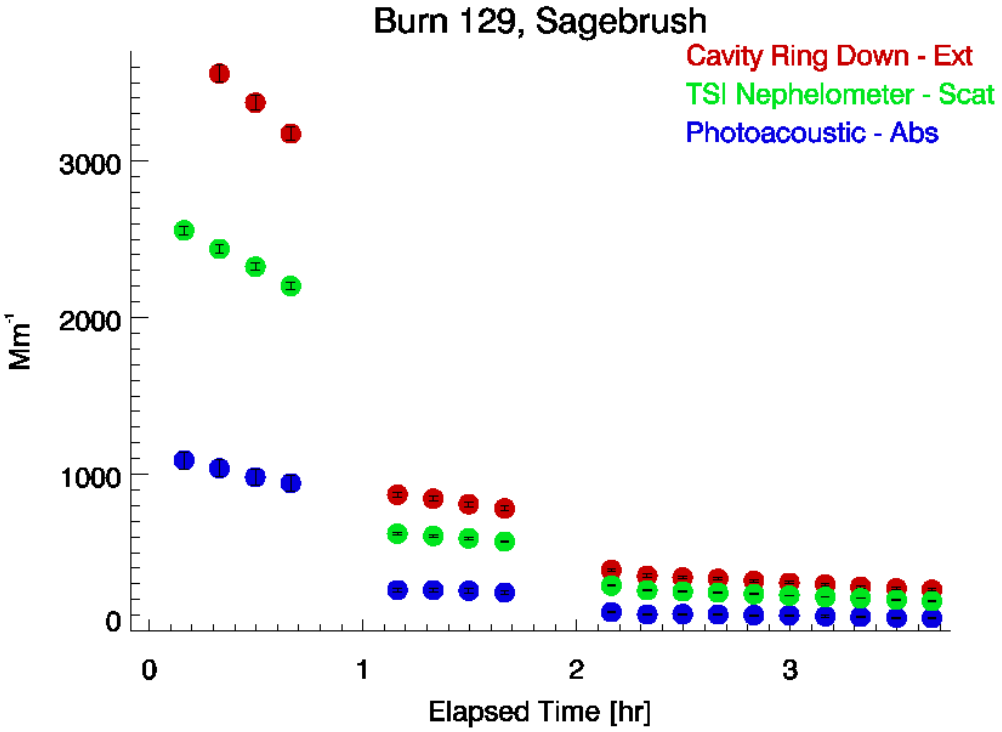

Figure 5-24 *Timeline of extinction, scattering and absorption coefficients for burn 129, sagebrush.*

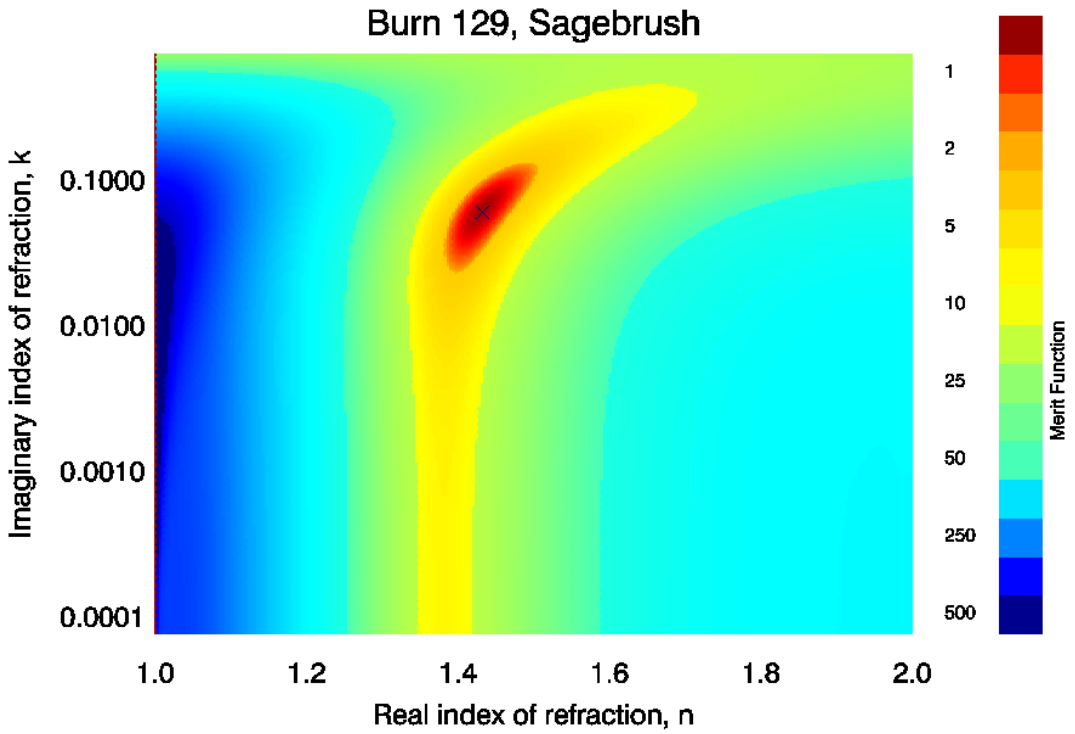

Figure 5-25 *Merit function for burn 129, sagebrush, over range of index of refraction. Minimum merit function was 0.102. The retrieved refractive index is indicated by the cross.*

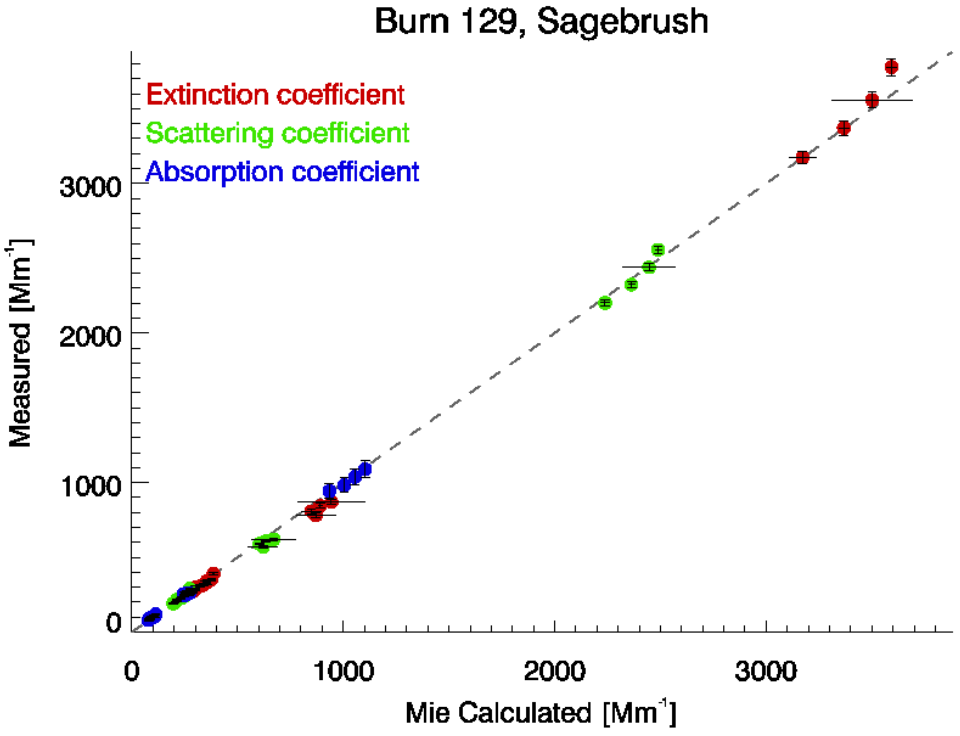

Figure 5-26 *Comparison of measured and calculated values of extinction, scattering and absorption coefficient for burn 129, sagebrush. Calculated values are based on retrieved refractive index.*

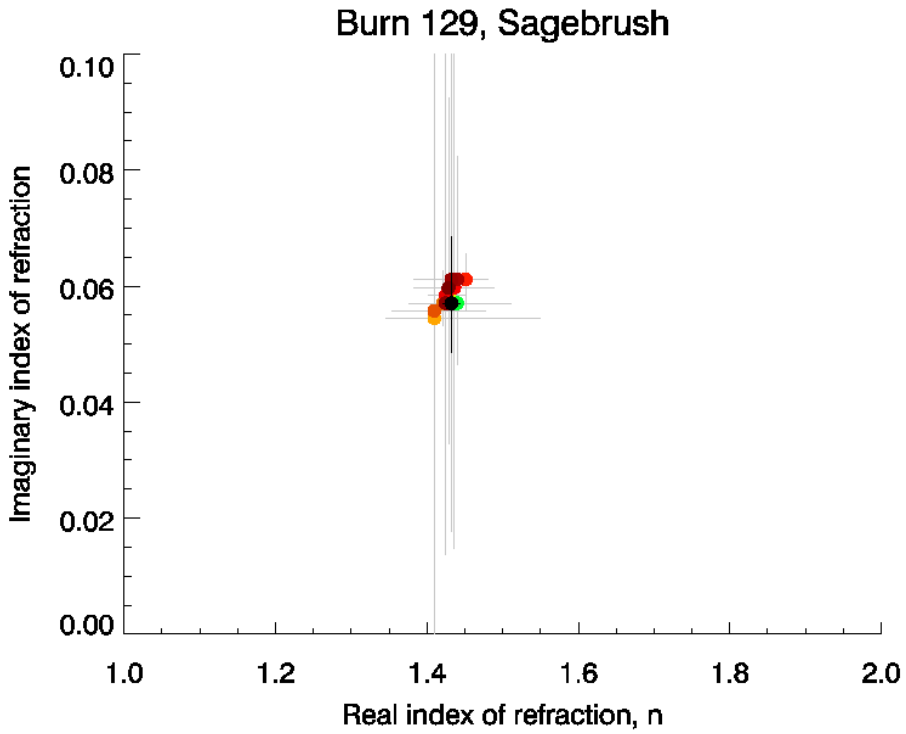

Figure 5-27 *Refractive indices retrieved for burn 129, sagebrush. The black point indicates the refractive index retrieved minimizing the error over the entire burn. The colored points indicated refractive indices retrieved for each time period of the burn. Colors indicate time during the burn where blue is the beginning and red the end.*

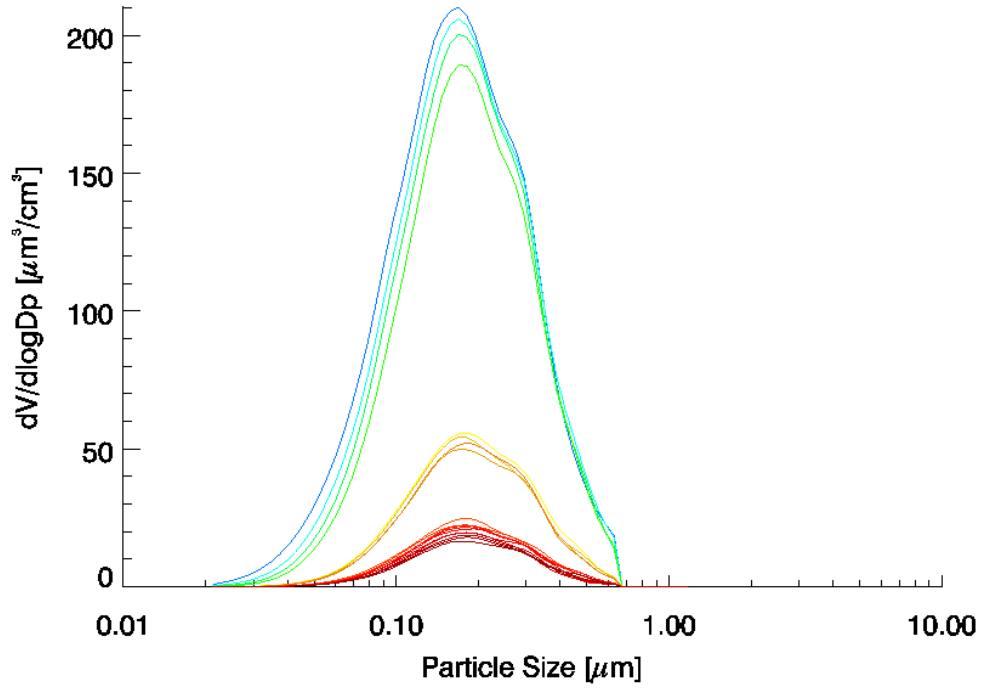

Figure 5-28 *DMA measured volume distributions for burn 129, sagebrush, shifted by a shape factor of 1.32.*

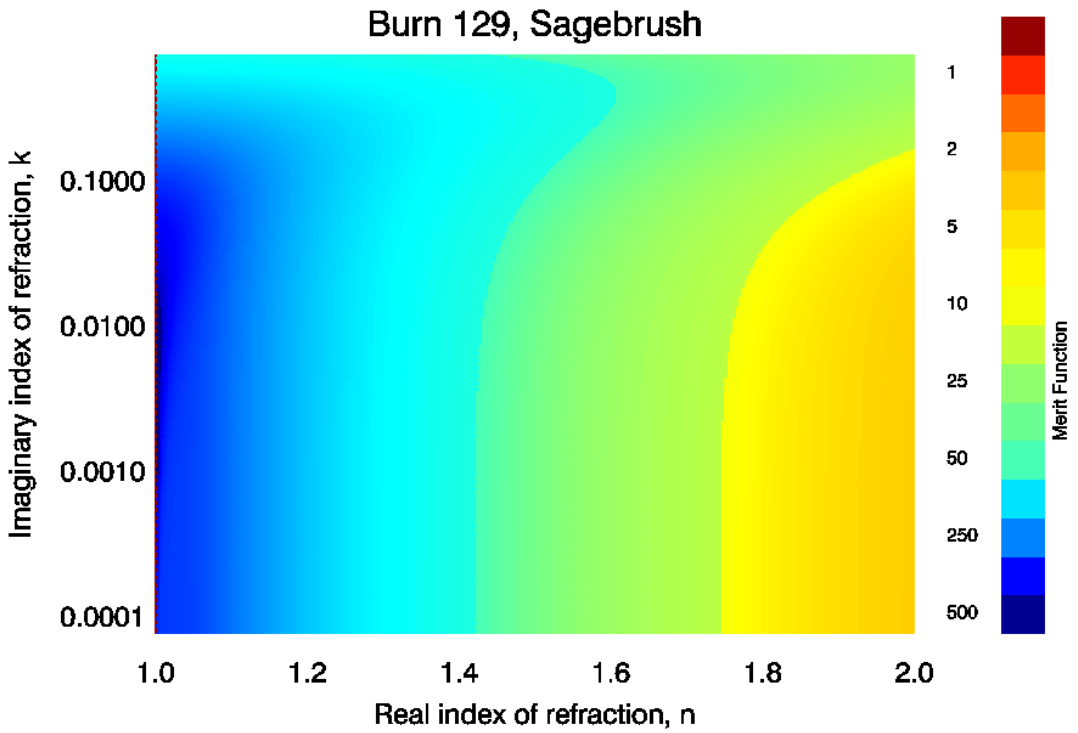

Figure 5-29 *Merit function for burn 129, sagebrush, using the shifted DMA measured size distribution. The minimum merit function was 0.365.*

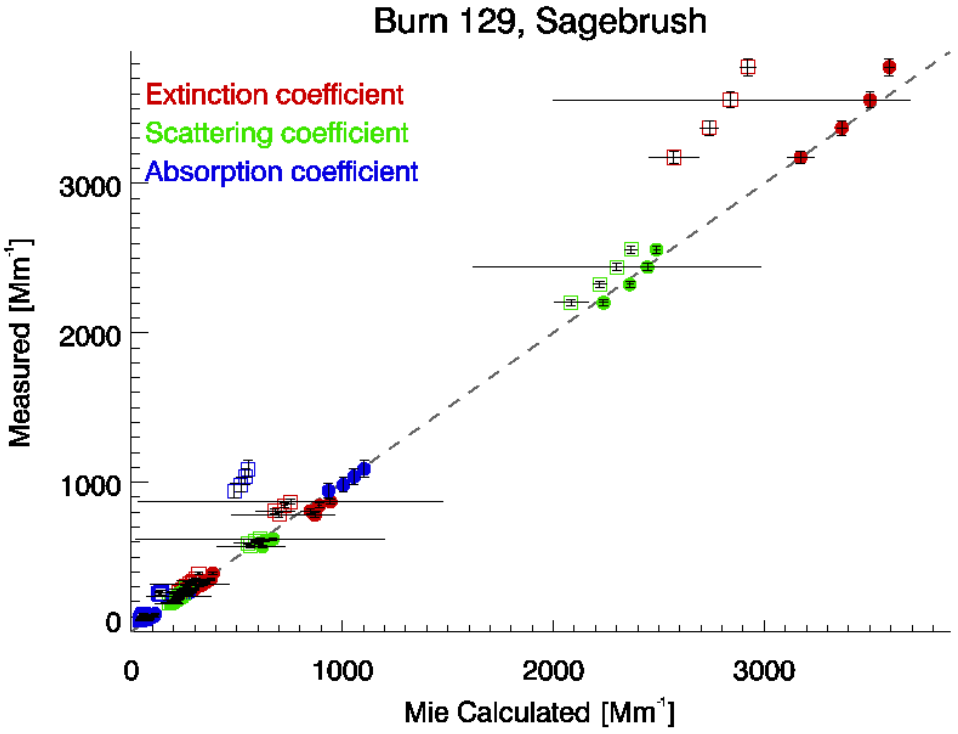

Figure 5-30 *Comparison of measured and calculated values of extinction, scattering and absorption coefficient for burn 129, sagebrush. Calculated values are based on retrieved refractive indices where the solid symbols indicate refractive indices retrieved using measured size distributions, and open symbols indicate refractive indices retrieved using shifted measured size distributions.*

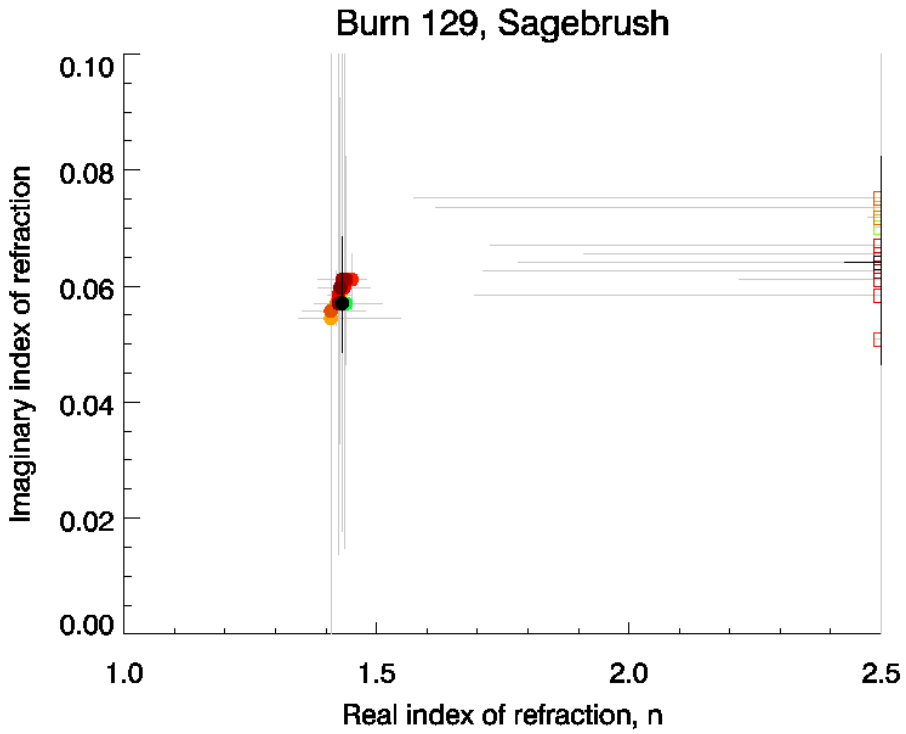

Figure 5-31 *Refractive indices retrieved for burn 129, sagebrush. The black points indicate the refractive indices retrieved minimizing the error over the entire burn. The colored points indicated refractive indices retrieved for each time period of the burn. Colors indicate time during the burn where blue is the beginning and red the end. Solid symbols indicate refractive indices retrieved using measured size distributions, open symbols indicate refractive indices retrieved using shifted measured size distributions.*

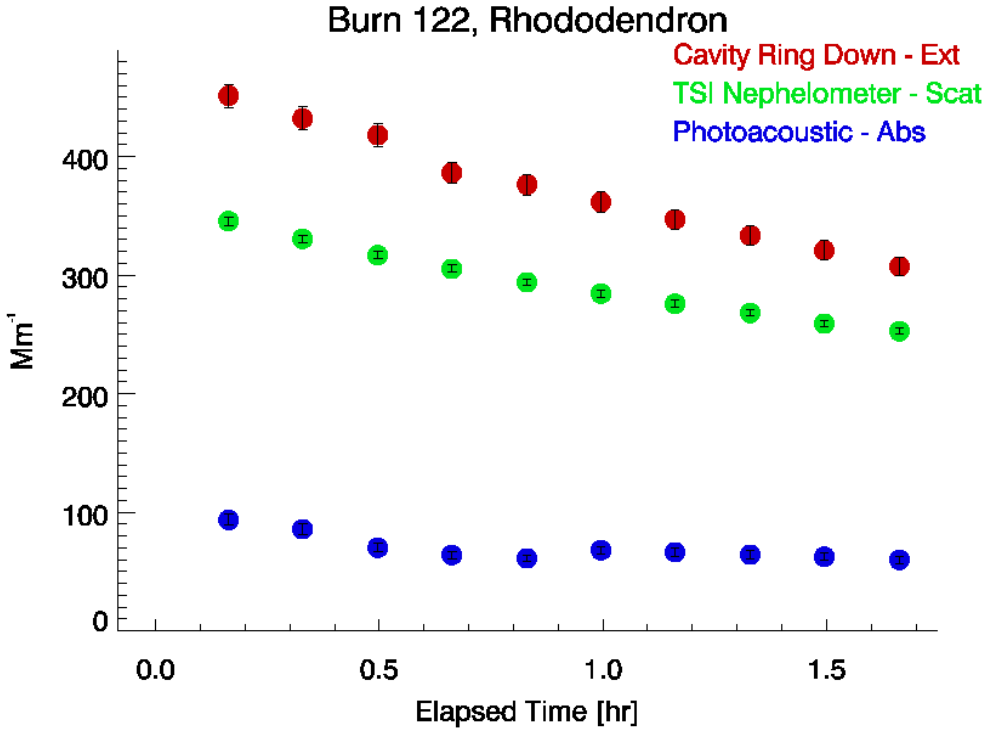

Figure 5-32 *Timeline of extinction, scattering and absorption coefficients for burn 122, rhododendron.*

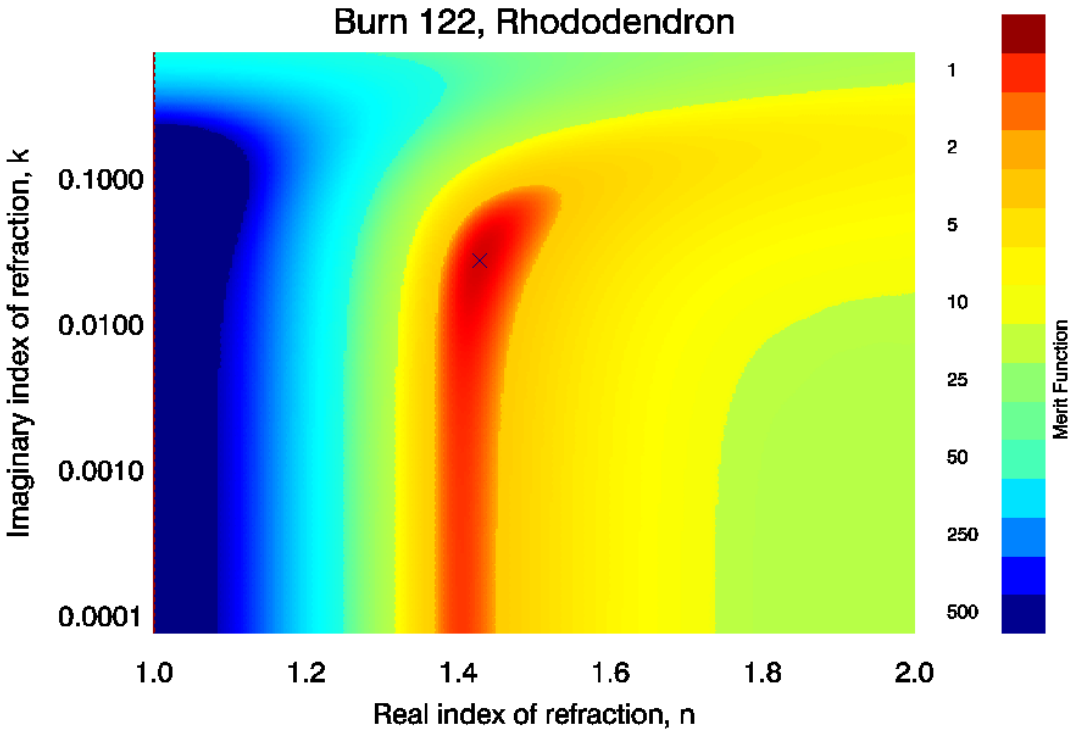

Figure 5-33 *Merit function for burn 122, rhododendron, over range of index of refraction. Minimum merit function was 0.74. The retrieved refractive index is indicated by the cross.*

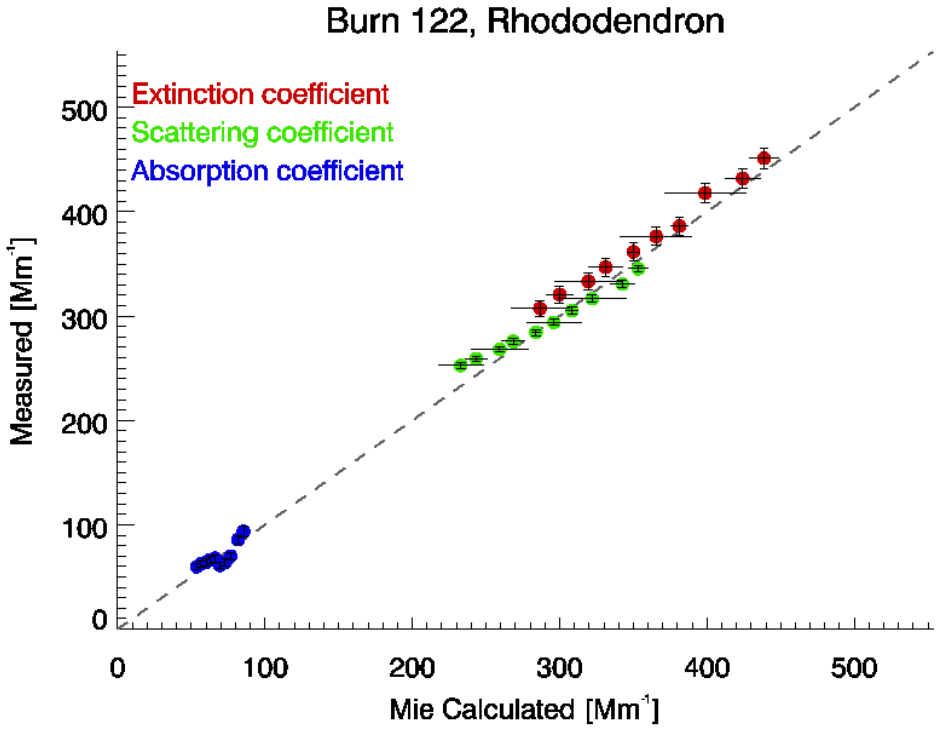

Figure 5-34 *Comparison of measured and calculated values of extinction, scattering and absorption coefficient for burn 122, rhododendron. Calculated values are based on retrieved refractive index.*

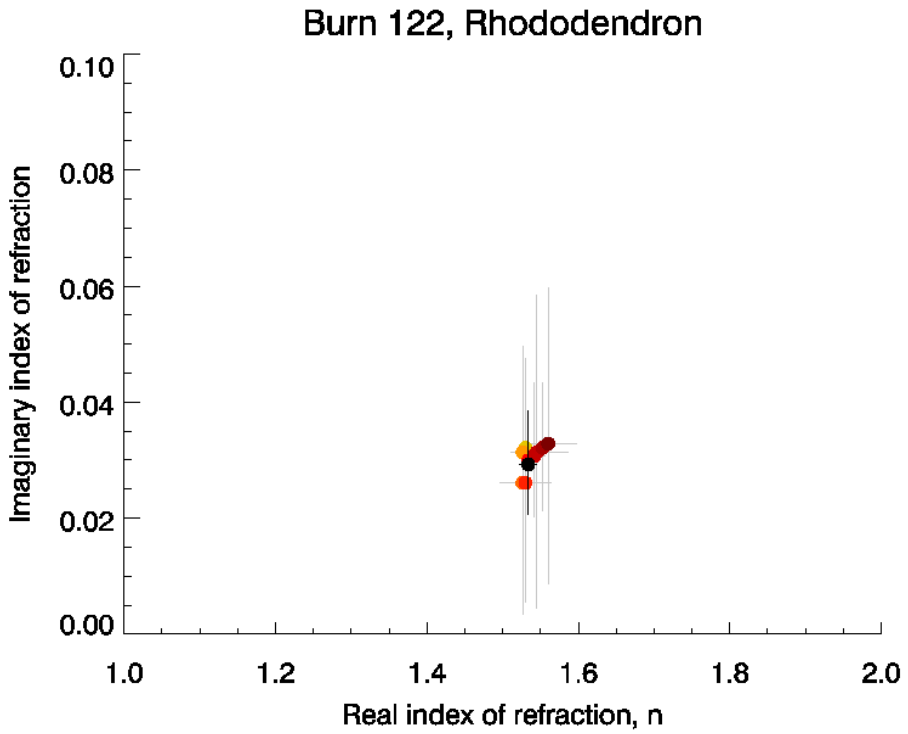

Figure 5-35 *Refractive indices retrieved for burn 122 rhododendron. The black point indicates the refractive index retrieved minimizing the error over the entire burn. The colored points indicated refractive indices retrieved for each time period of the burn. Colors indicate time during the burn where blue is the beginning and red the end.*

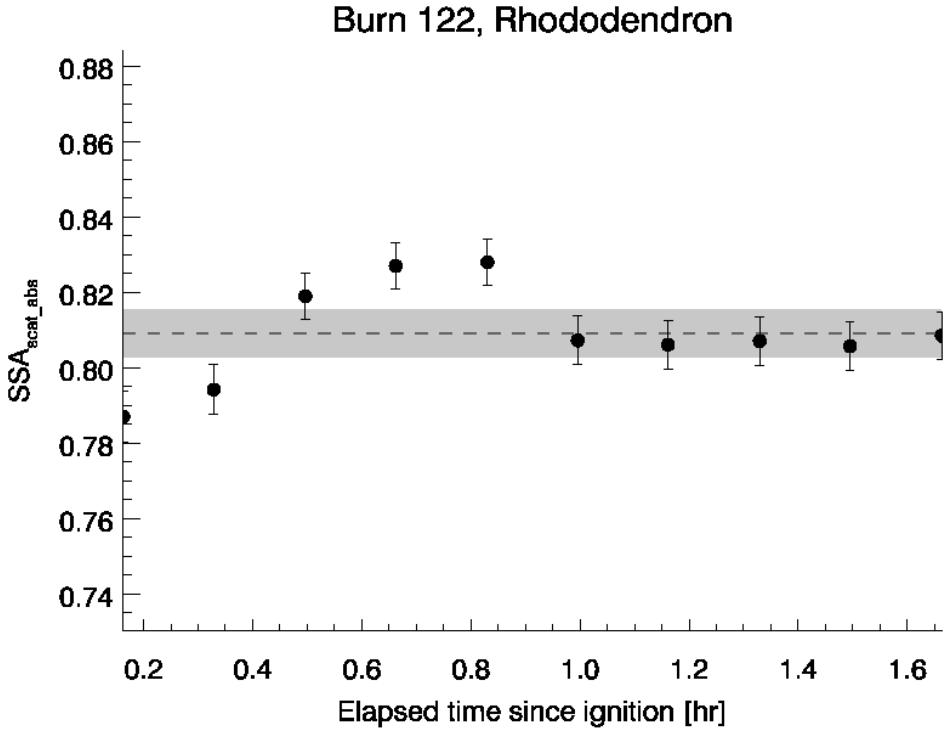

Figure 5-36 *Timeline of SSA_{scat_abs} for burn 122, rhododendron. The dashed line and grey shaded area indicate the average SSA and uncertainty.*

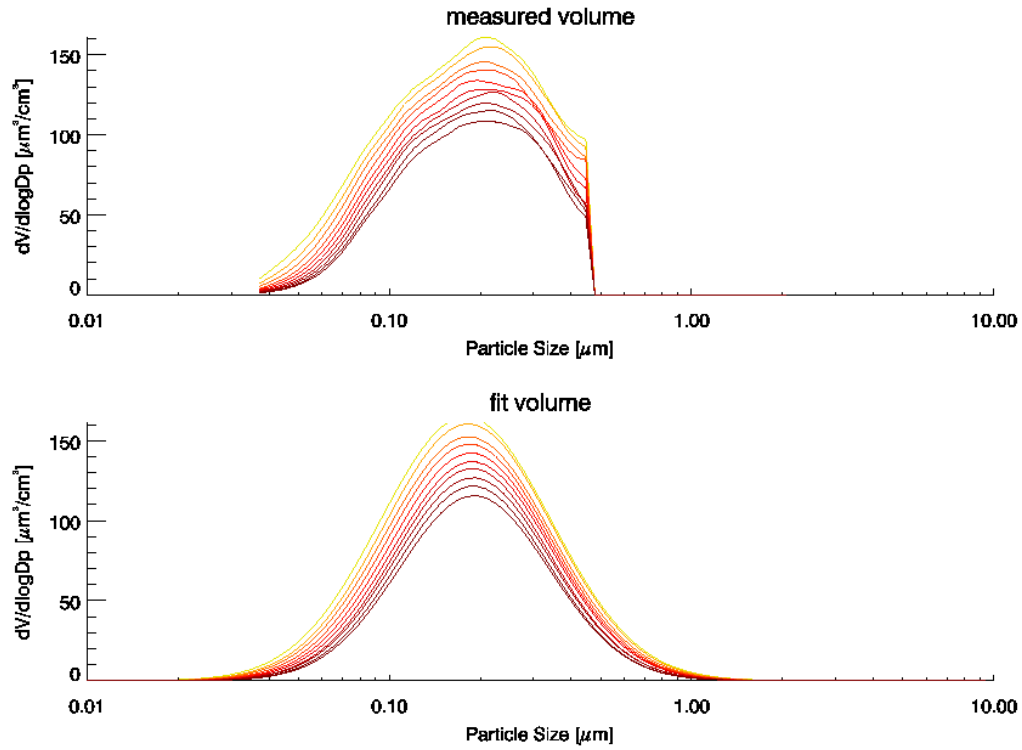

Figure 5-37 *Measured and lognormal fit size distributions for burn 122, rhododendron.*

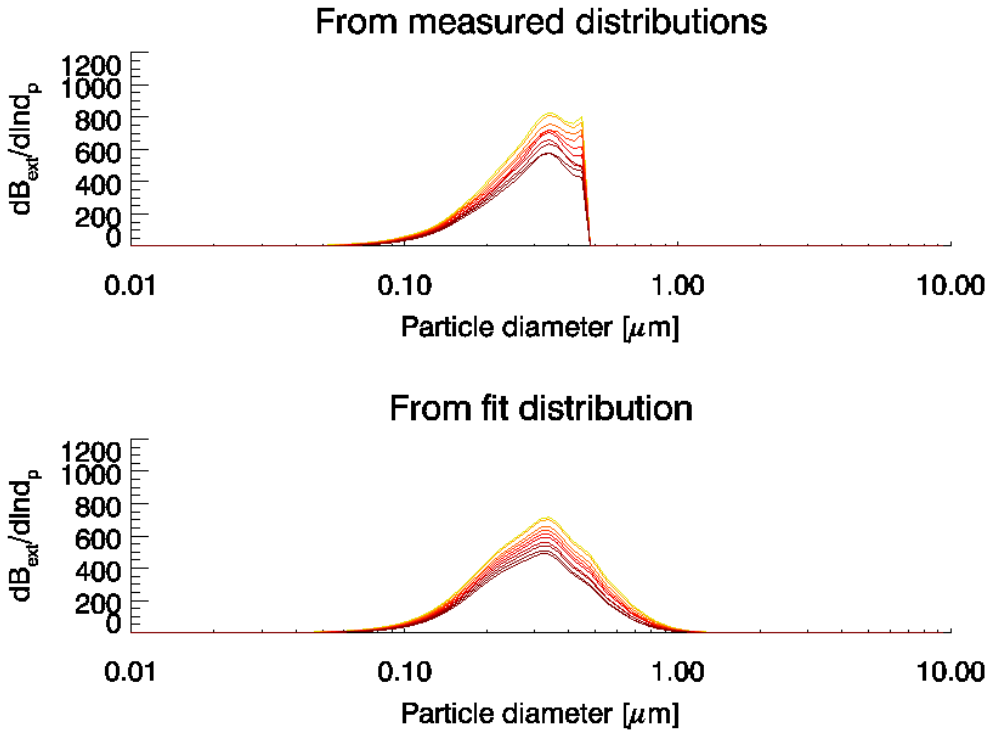

Figure 5-38 *Calculated extinction distributions for burn 122, rhododendron.*

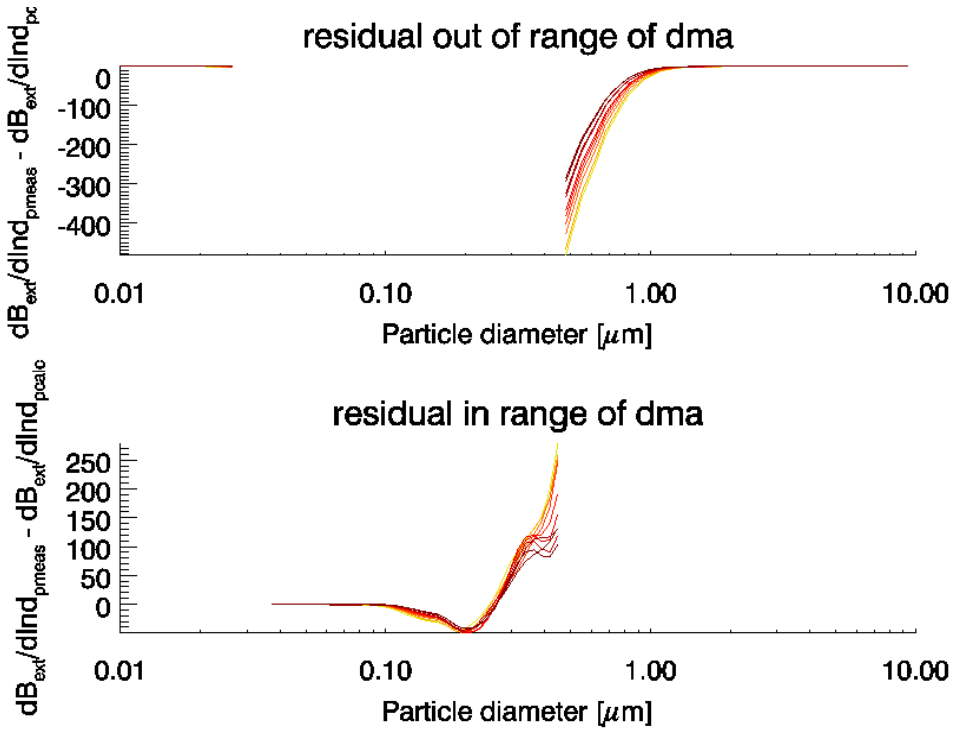

Figure 5-39 *Residual of extinction distribution for burn 122, rhododendron. The top plot indicates the extra extinction information gained by the fit distribution; the lower plot indicates the error between the fit and measured distributions.*

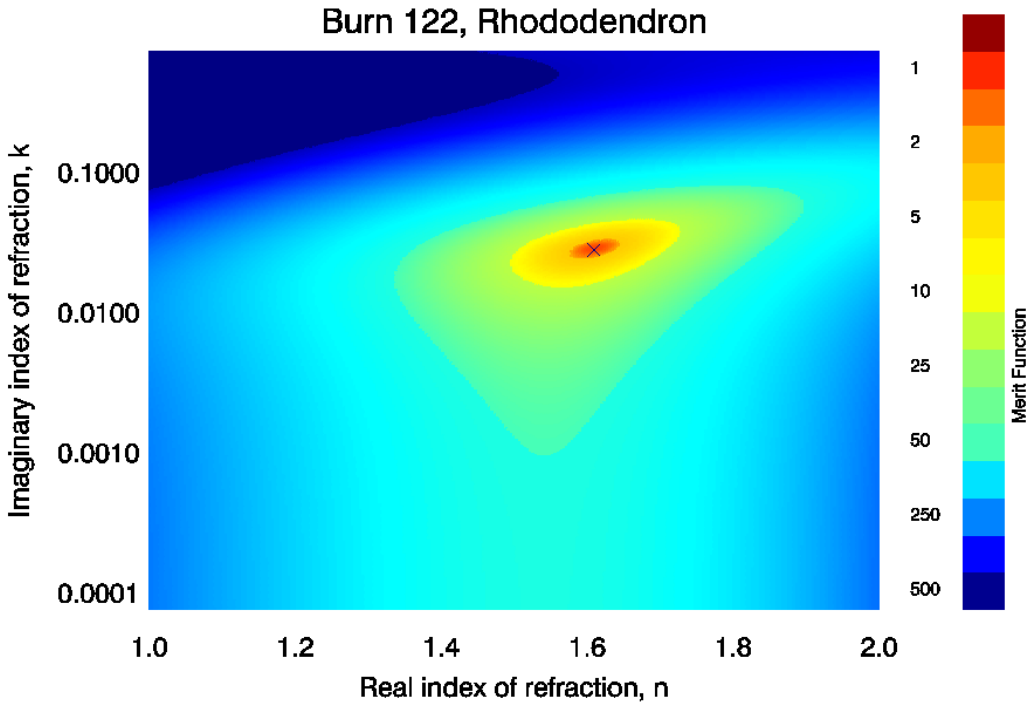

Figure 5-40 *Merit function for burn 122, rhododendron, using the fit lognormal size distribution. The minimum merit function was 1.217. The retrieved refractive index is indicated by the cross.*

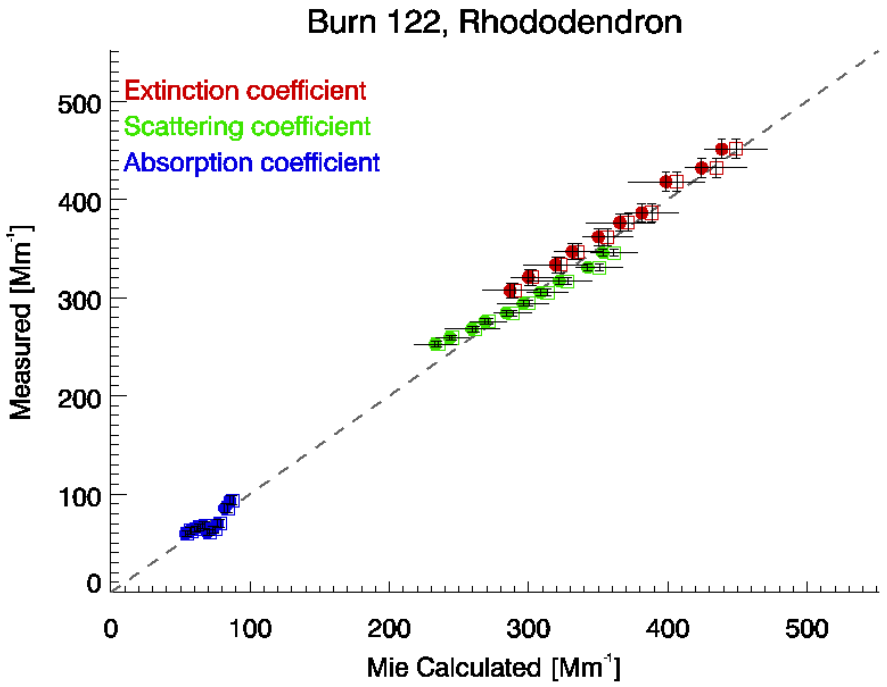

Figure 5-41 *Comparison of measured and calculated values of extinction, scattering and absorption coefficient for burn 122, rhododendron. Calculated values are based on retrieved refractive indices where the solid symbols indicate refractive indices retrieved using measured size distributions, open symbols indicate refractive indices retrieved using fit lognormal size distributions.*

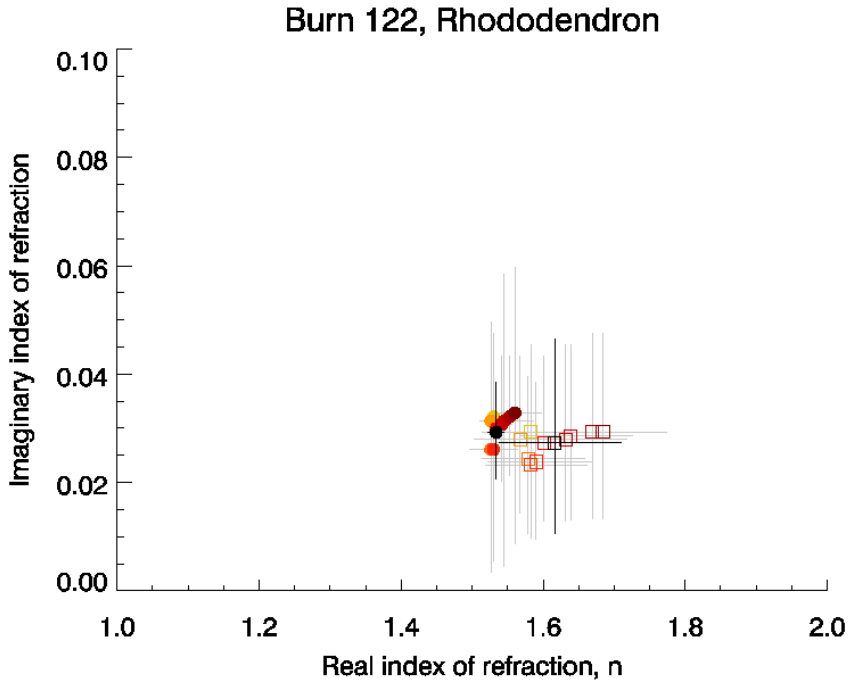

Figure 5-42 *Refractive indices retrieved for burn 122, rhododendron. The black points indicate the refractive indices retrieved minimizing the error over the entire burn. The colored points indicated refractive indices retrieved for each time period of the burn. Colors indicate time during the burn where blue is the beginning and red the end. Solid symbols indicate refractive indices retrieved using measured size distributions, open symbols indicate refractive indices retrieved using fit lognormal size distributions.*

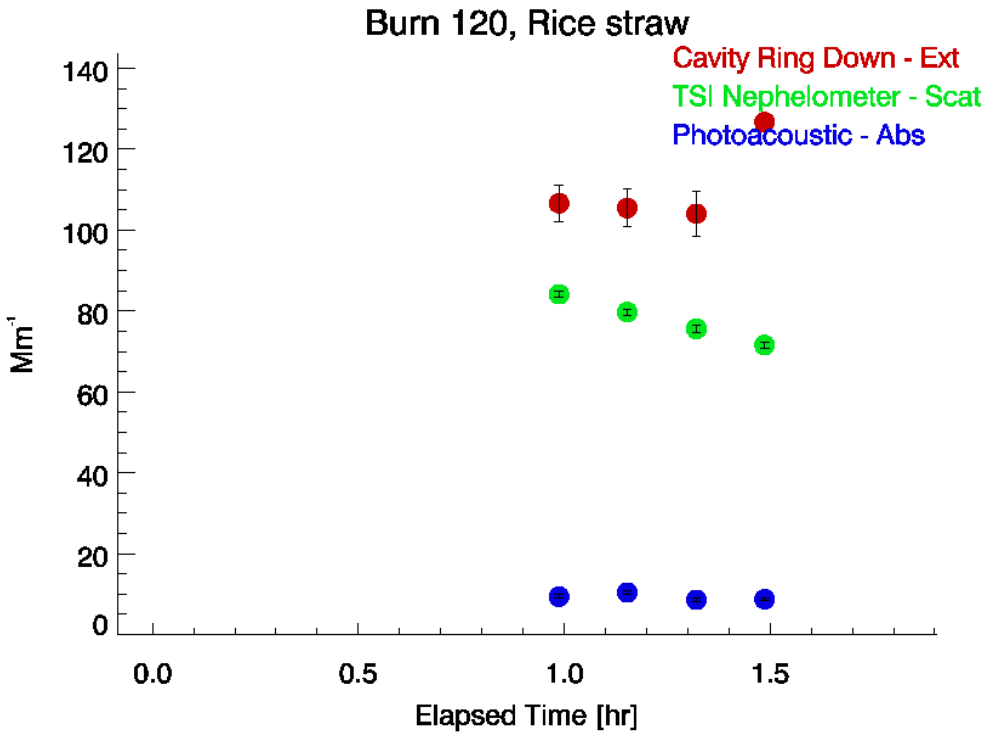

Figure 5-43 *Timeline of extinction, scattering and absorption coefficients for burn 120, rice straw.*

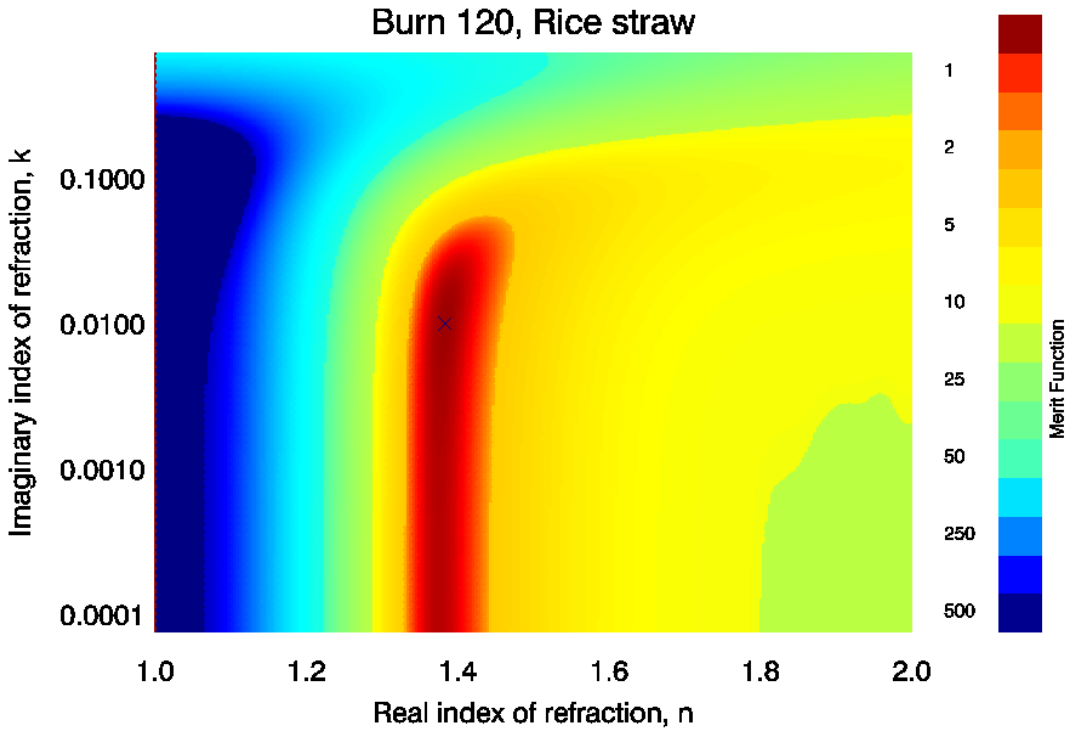

Figure 5-44 *Merit function for burn 120, rice straw, over range of index of refraction. Minimum merit function was 0.036. The retrieved refractive index is indicated by the cross.*

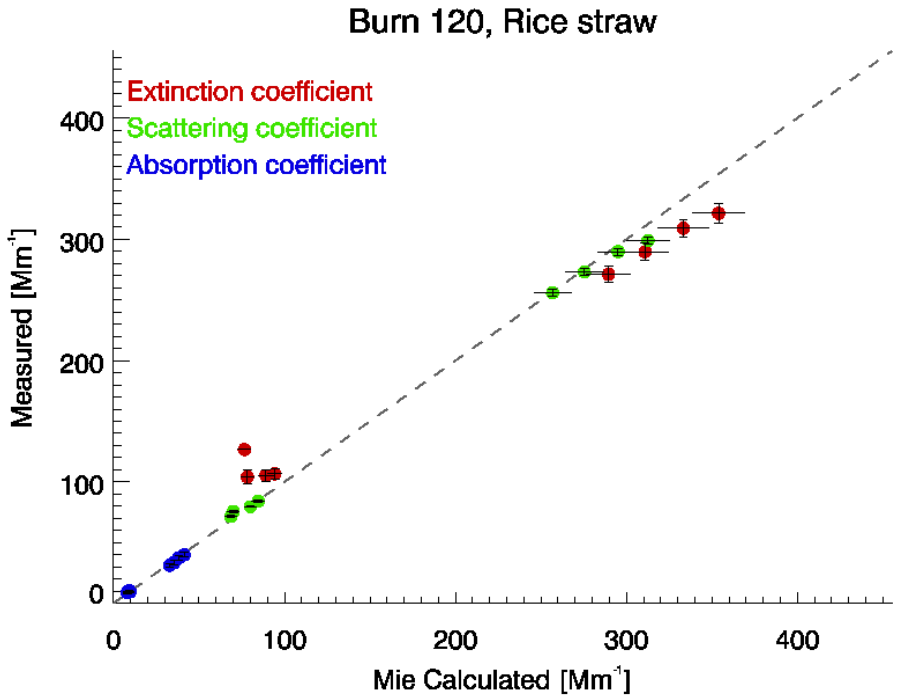

Figure 5-45 *Comparison of measured and calculated values of extinction, scattering and absorption coefficient for burn 120, rice straw. Calculated values are based on retrieved refractive index.*

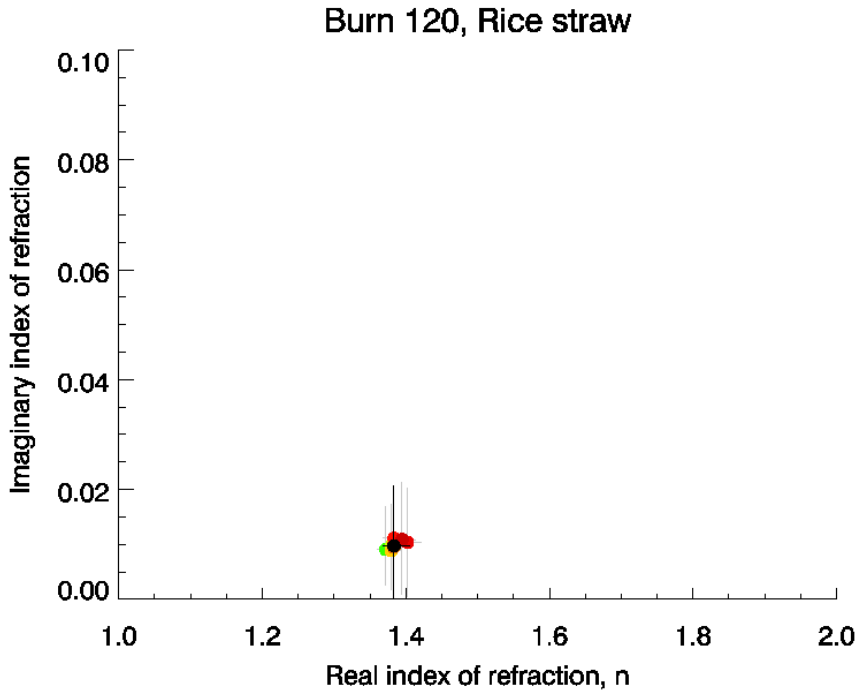

Figure 5-46 *Refractive indices retrieved for burn 120, rice straw. The black point indicates the refractive index retrieved minimizing the error over the entire burn. The colored points indicated refractive indices retrieved for each time period of the burn. Colors indicate time during the burn where blue is the beginning and red the end.*

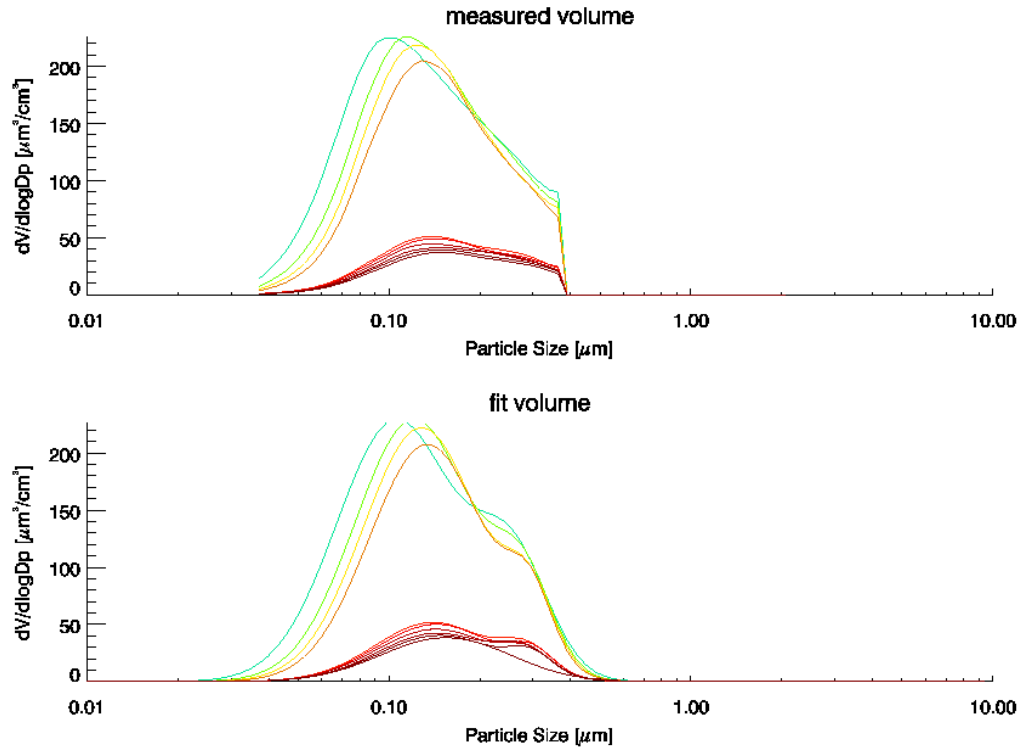

Figure 5-47 *Measured and lognormal fit size distributions for burn 120, rice straw.*

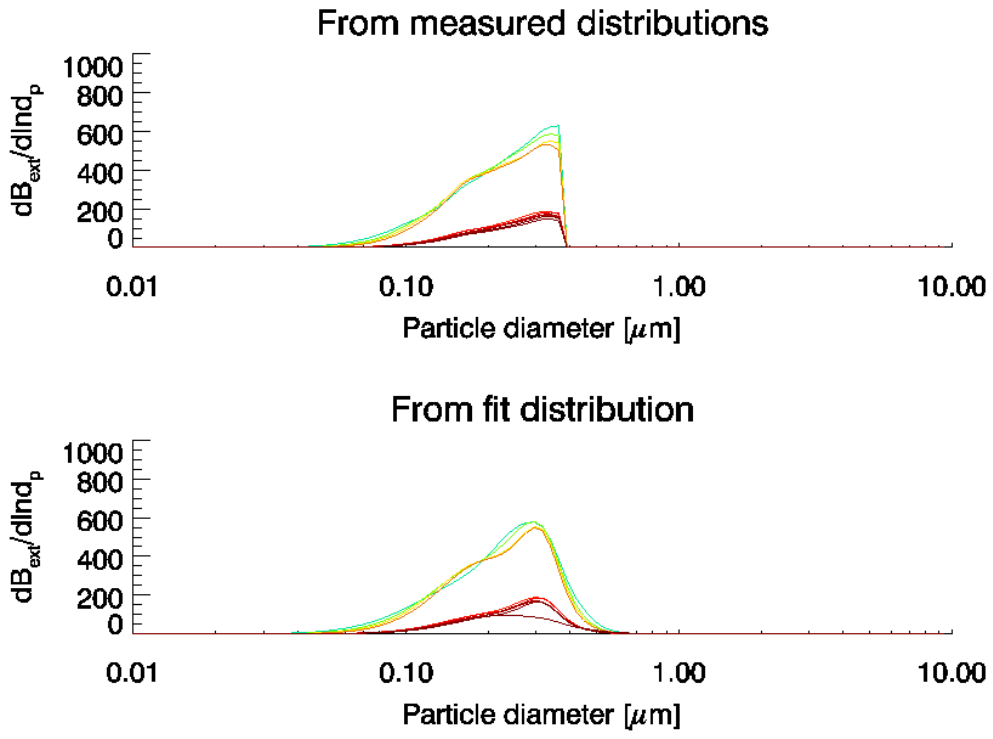

Figure 5-48 *Calculated extinction distributions for burn 120, rice straw.*

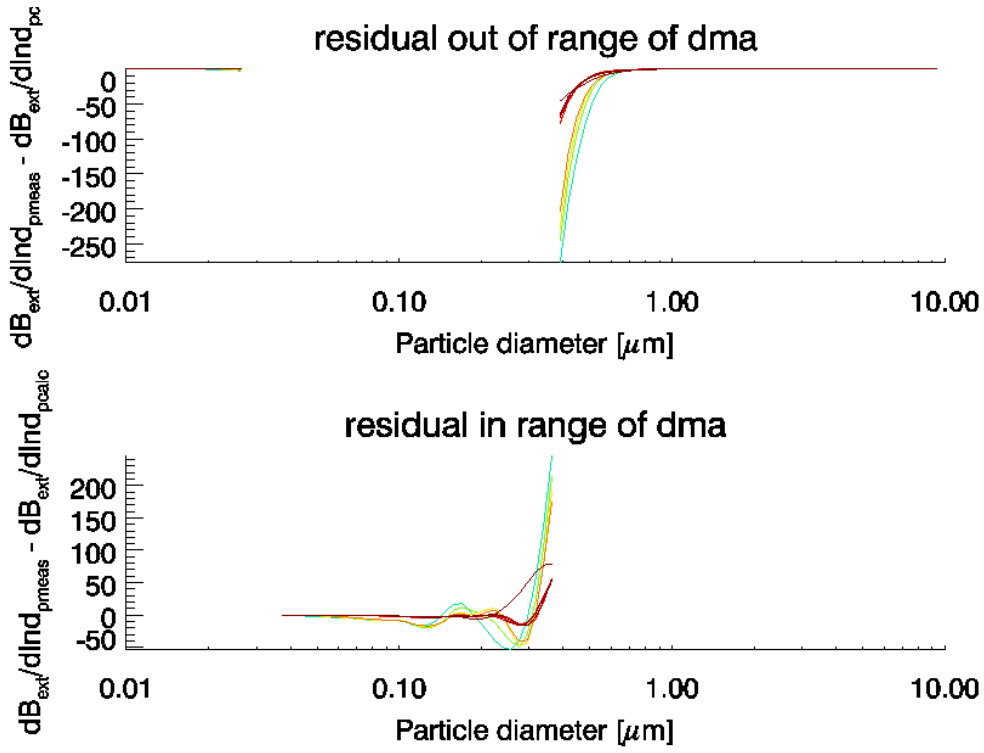

Figure 5-49 *Residual of extinction distribution for burn 120, rice straw. The top plot indicates the extra extinction information gained by the fit distribution; the lower plot indicates the error between the fit and measured distributions.*

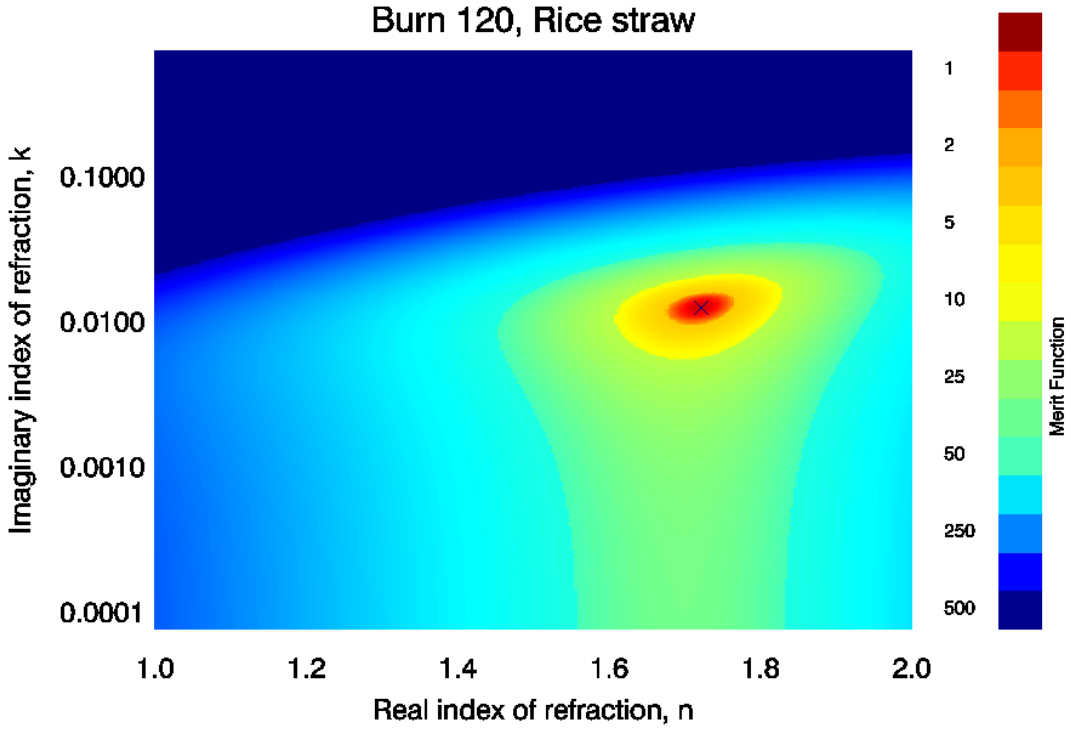

Figure 5-50 *Merit function for burn 120, rice straw, using the fit lognormal size distribution. The minimum merit function was 0.383. The retrieved refractive index is indicated by the cross.*

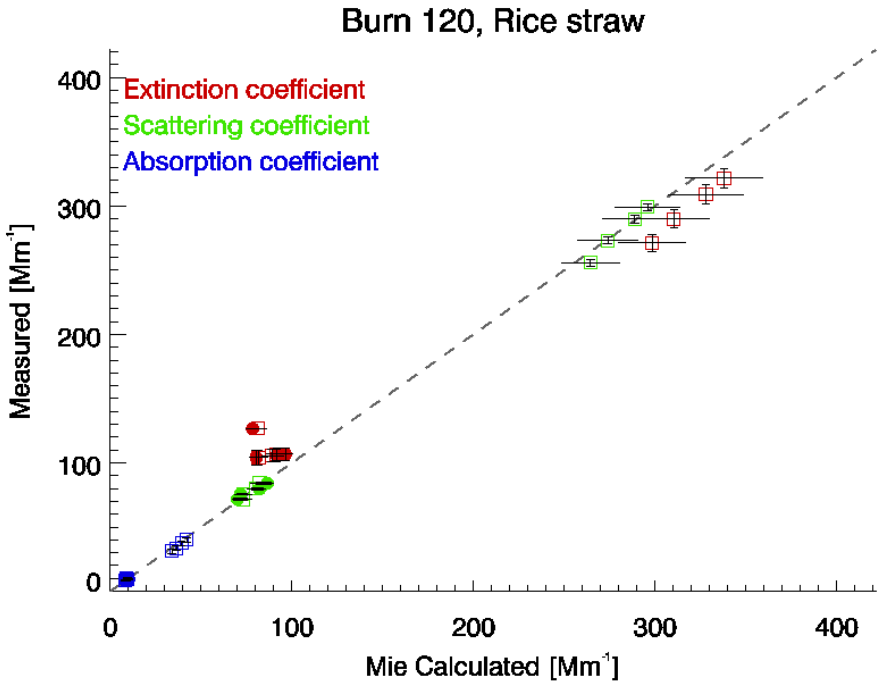

Figure 5-51 *Comparison of measured and calculated values of extinction, scattering and absorption coefficient for burn 120, rice straw. Calculated values are based on retrieved refractive indices where the solid symbols indicate refractive indices retrieved using measured size distributions and open symbols indicate refractive indices retrieved using fit lognormal size distributions.*

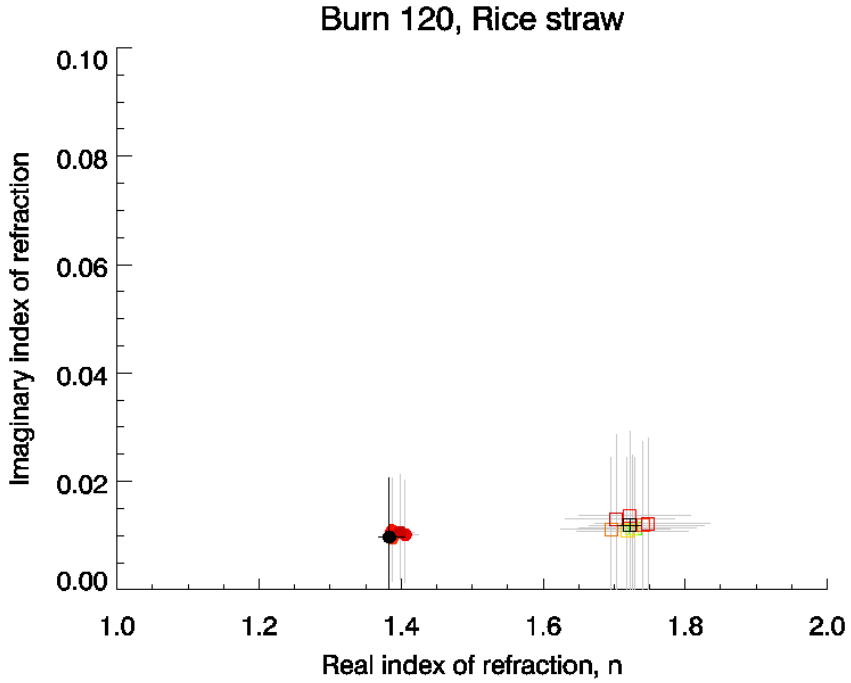

Figure 5-52 *Refractive indices retrieved for burn 120, rice straw. The black points indicate the refractive indices retrieved minimizing the error over the entire burn. The colored points indicated refractive indices retrieved for each time period of the burn. Colors indicate time during the burn where blue is the beginning and red the end. Solid symbols indicate refractive indices retrieved using measured size distributions and open symbols indicate refractive indices retrieved using fit lognormal size distributions.*

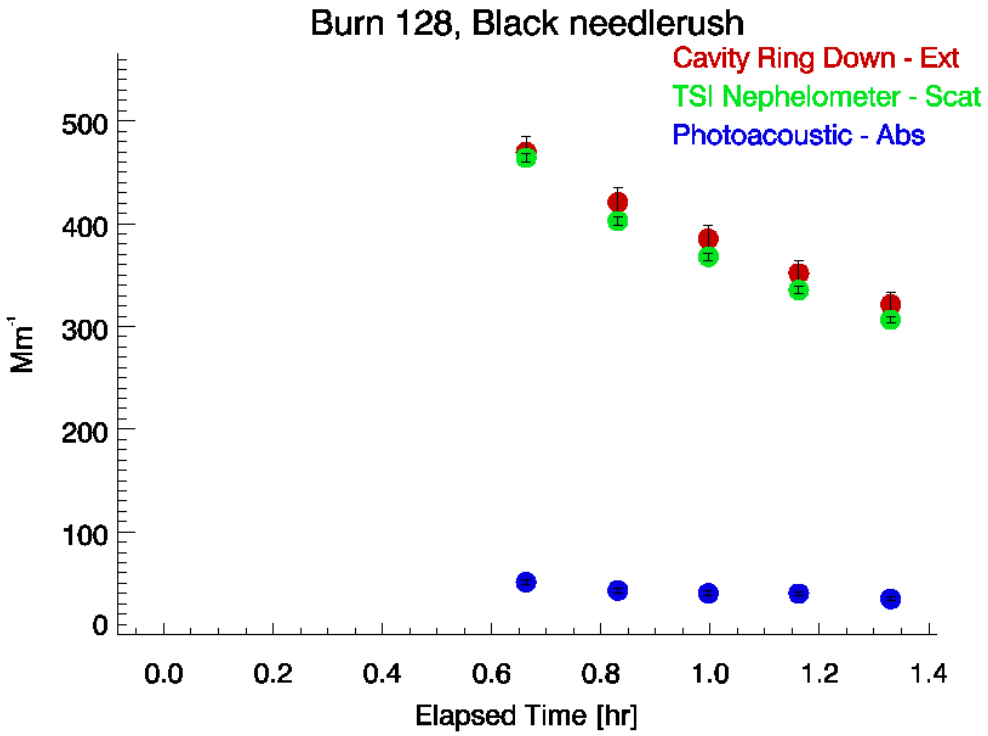

Figure 5-53 *Timeline of extinction, scattering and absorption coefficients for burn 128, black needlerush.*

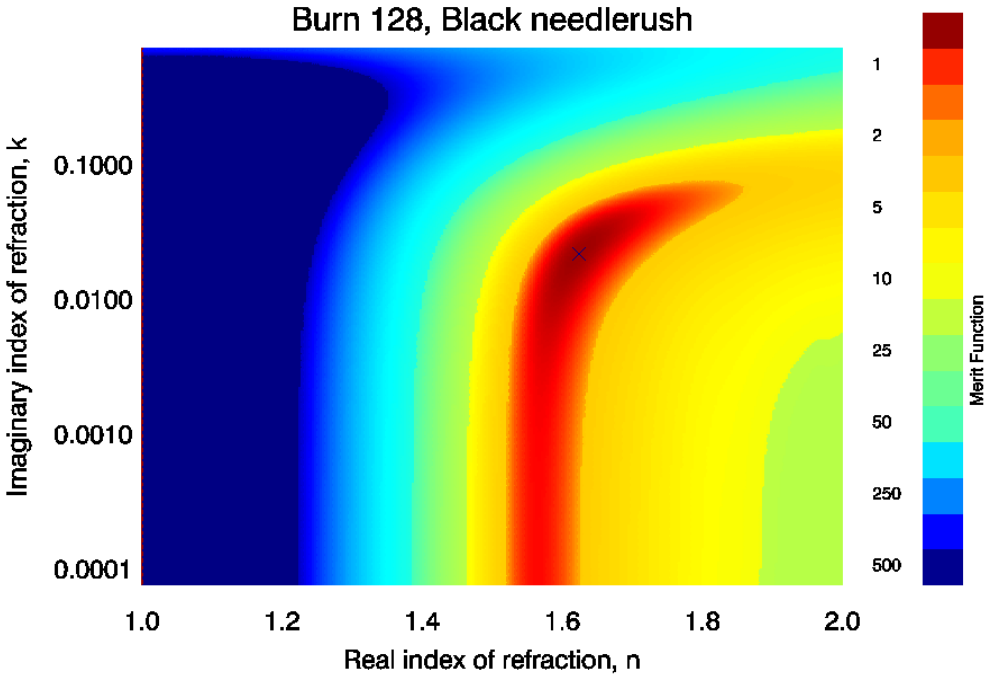

Figure 5-54 *Merit function for burn 128, black needlerush, over range of index of refraction. Minimum merit function was 0.030. The retrieved refractive index is indicated by the cross.*

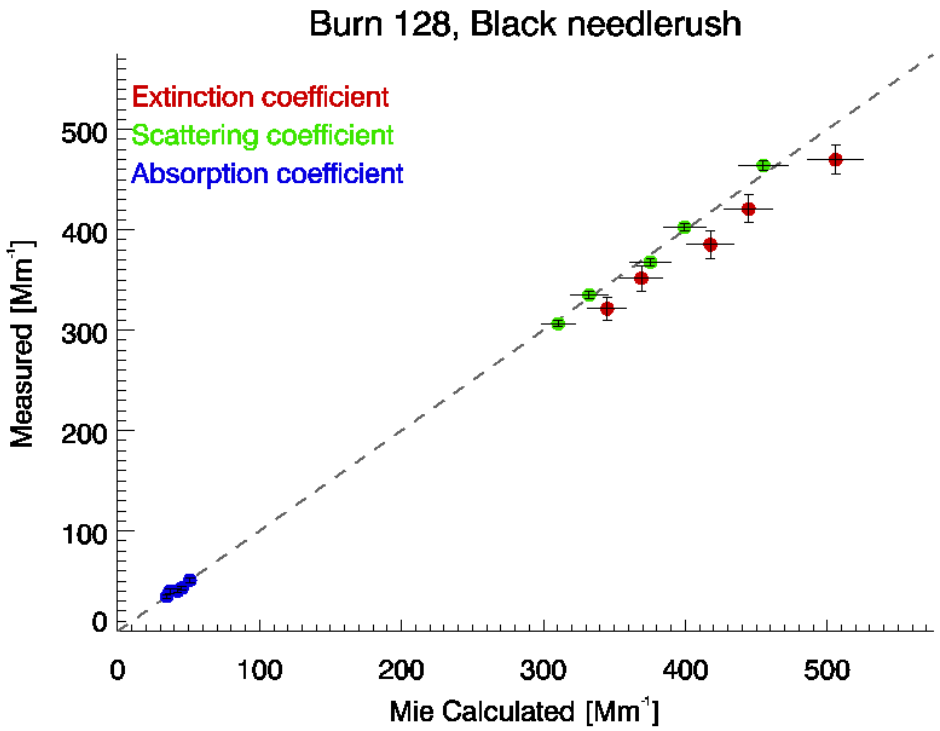

Figure 5-55 *Comparison of measured and calculated values of extinction, scattering and absorption coefficient for burn 128, black needlerush. Calculated values are based on retrieved refractive index.*

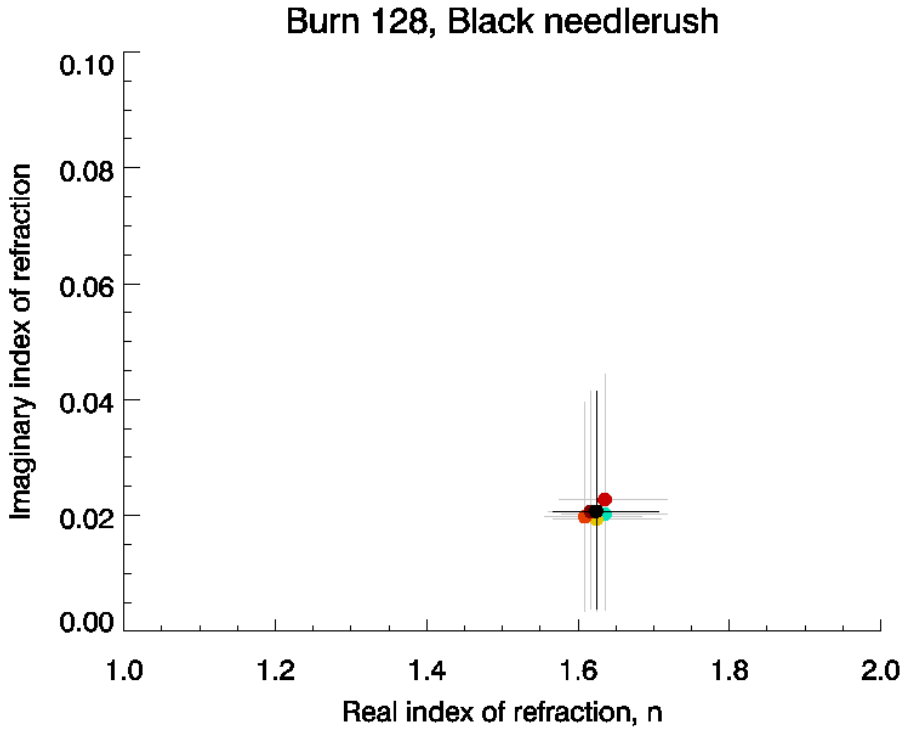

Figure 5-56 *Refractive indices retrieved for burn 128, needlerush. The black point indicates the refractive index retrieved minimizing the error over the entire burn. The colored points indicated refractive indices retrieved for each time period of the burn. Colors indicate time during the burn where blue is the beginning and red the end.*

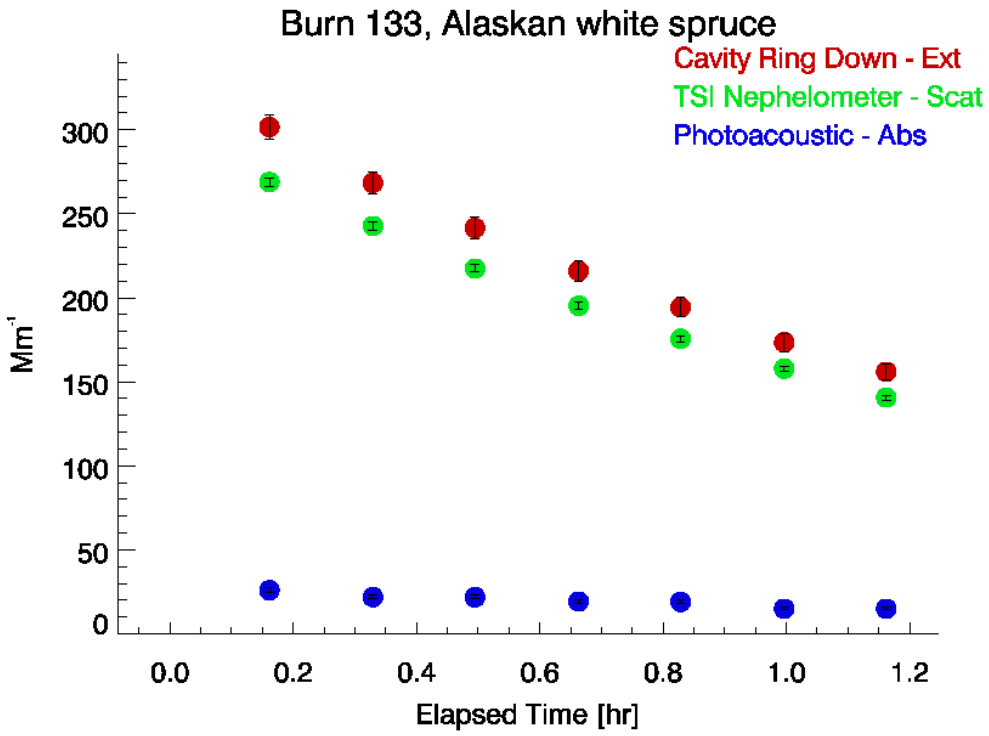

Figure 5-57 *Timeline of extinction, scattering and absorption coefficients for burn 133, Alaskan white spruce.*

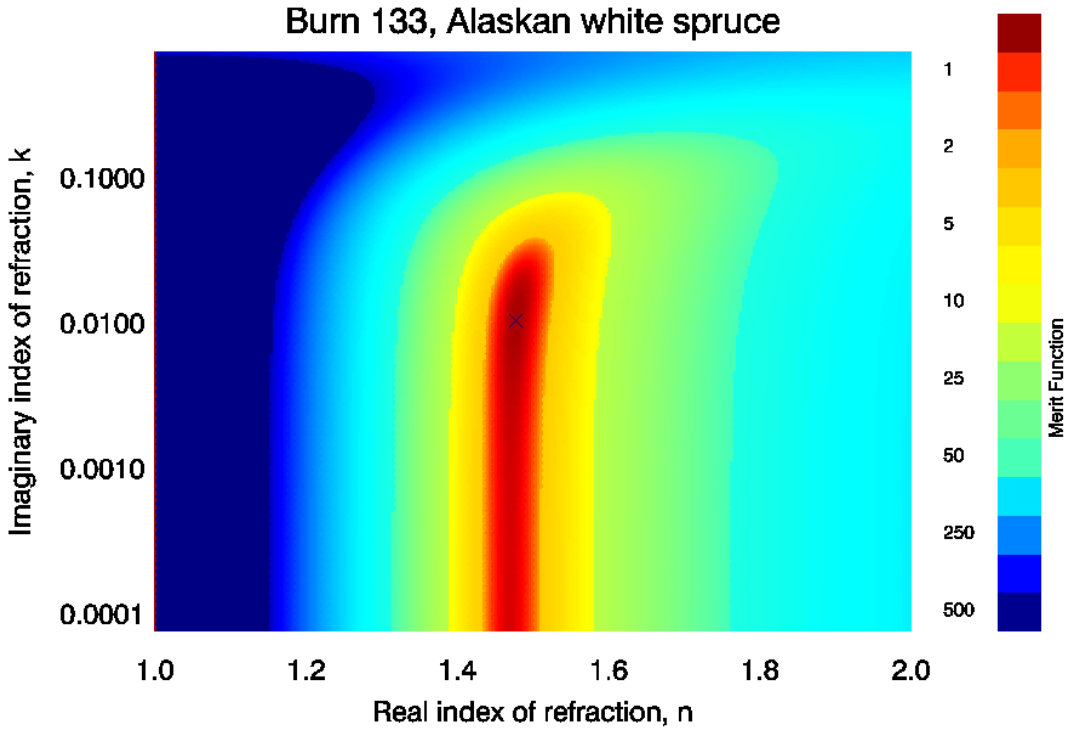

Figure 5-58 *Merit function for burn 133, Alaskan white spruce, over range of index of refraction. Minimum merit function was 0.098. The retrieved refractive index indicated by the cross.*

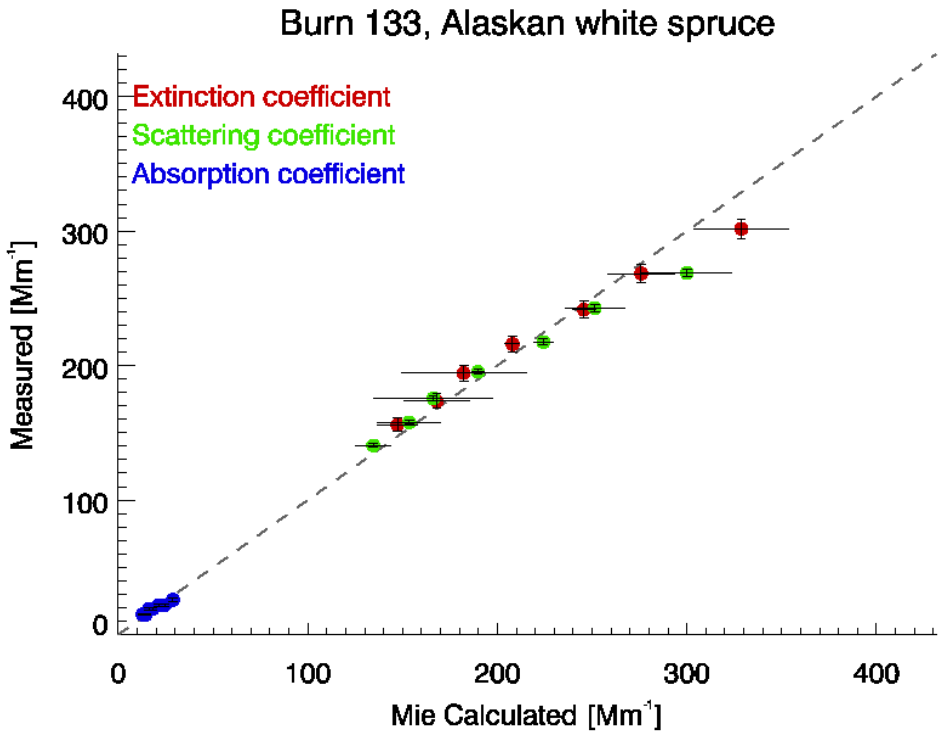

Figure 5-59 *Comparison of measured and calculated values of extinction, scattering and absorption coefficient for burn 133, Alaskan white spruce. Calculated values are based on retrieved refractive index.*

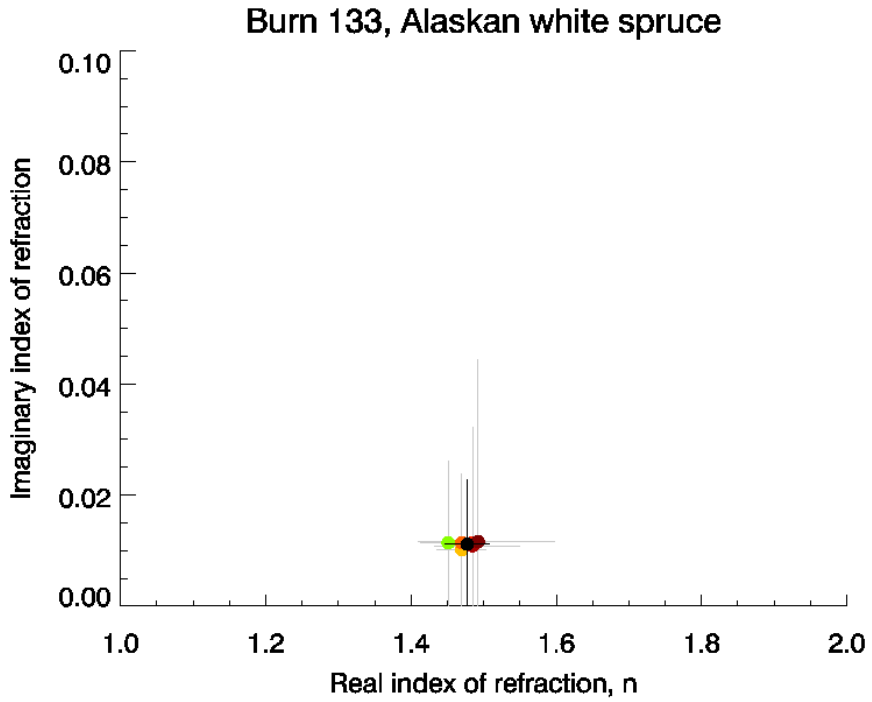

Figure 5-60 *Refractive indices retrieved for burn 133, Alaskan white spruce. The black point indicates the refractive index retrieved minimizing the error over the entire burn. The colored points indicated refractive indices retrieved for each time period of the burn. Colors indicate time during the burn where blue is the beginning and red the end.*

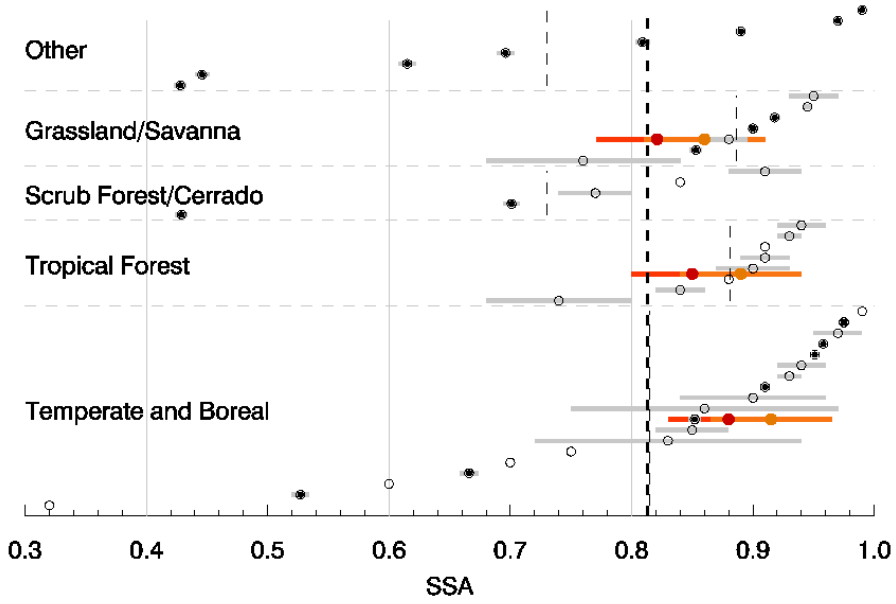

Figure 5-61 *Comparison of SSA values listed Table 5.2 and Table 5.3 for each fuel type, values are indicated by open and filled circles respectively; grey shaded areas indicate uncertainty. Suggested fresh and aged values of SSA listed in Table 5.4 are indicated by the red (fresh) and orange (aged) points. Average measured values of SSA for each fuel type are indicated by the dashed lines and the solid dashed line indicates the average of all SSA values. Fuel type "other" indicates FLAME2 measured SSAs for the southeastern shrubs, Asian fuels and AK duff.*

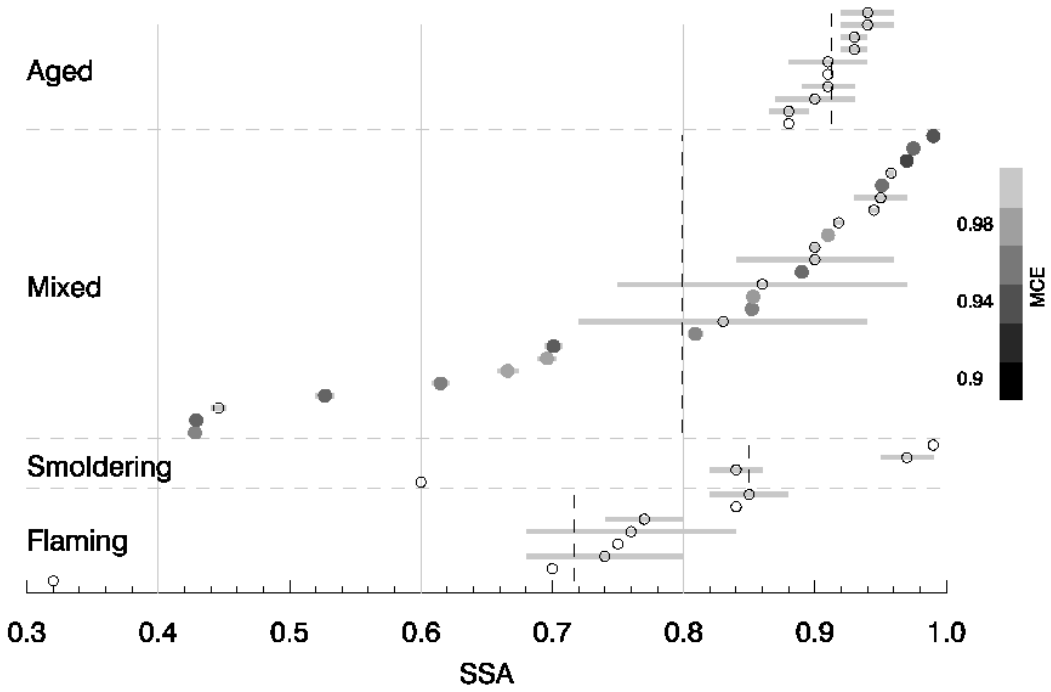

Figure 5-62 *Literature and FLAME2 values of SSA categorized by combustion type. FLAME2 results are shaded by MCE where lower MCE, smoldering type combustion, is black and high MCE, flaming type combustion is light grey. Literature values of SSA are indicated by hollow circles.*

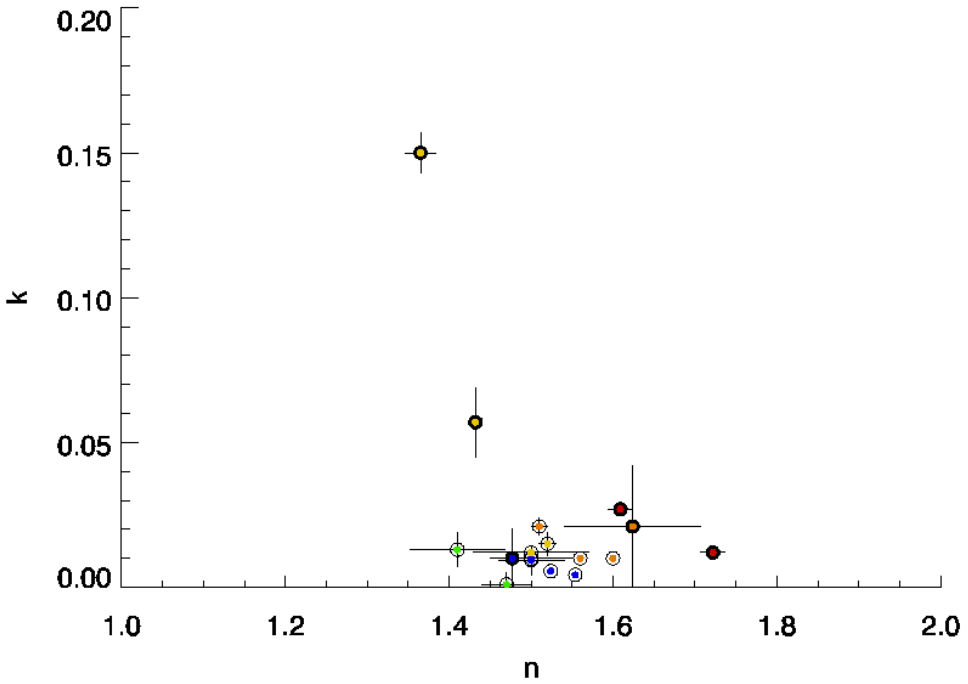

Figure 5-63 *Literature and FLAME2 retrieved values of refractive index plotted as open and closed circles respectively. Colors indicate fuel type where blue – temperate/boreal, green – tropical forest, yellow – scrub forest/cerrado, orange – grassland/savanna and red – other.*

Chapter 6 SUMMARY AND FUTURE WORK

6.1 Summary

FLAME2 provided a unique forum where measurements of aerosol extinction, scattering and absorption could be made for various magnitudes of absorption to test for optical closure between measurements. Measurements of absorption coefficients are0020often difficult to obtain accurately via traditional filter based methods because of artifacts introduced by the substrate. Because of the difficulty in obtaining accurate independent absorption coefficient measurements, a difference technique (absorption coefficient = extinction – scattering coefficient), is often used to obtain values of the absorption coefficient. For the FLAME2 study our plans were to accurately measure extinction, scattering and absorption coefficients at a common wavelength of λ = 532 nm using a cavity ring-down spectrometer (CRD), TSI nephelometer and photo-acoustic spectrometer (PAS). Because of the large range of absorption coefficients measured, it would be possible to determine how accurate the difference technique was for various magnitudes of absorption coefficient.

Tests were performed on the CSU CRD instrument after deployment in FLAME2 to determine accuracy, uncertainty, particle loss and stability of the filtered air measurements. Extinction coefficients due to PSL particles 0.3, 0.4 and 0.5 μm in diameter were measured by the CRD and an accuracy of ±10% was found by comparing measured extinction coefficients and extinction coefficients calculated using measured

particle concentrations, size distributions and Mie theory. The theoretical uncertainty of the instrument was found to be 0.011 Mm^{-1} while measurement uncertainty was determined using the standard deviation of measurements of a 5 second average; measurement uncertainty was ~ 5% for values measured during the FLAME2 study. A particle loss of 3% through the CRD valve system, inlet, cell and sample outlets for the particle size range of 0.2 - 0.5 μm in diameter was determined. Theoretical calculations indicate that for particles > 1.1 μm losses would be much larger. Measurements of filtered air extinction coefficients indicated that drift in the filtered air extinction measurement due to environmental parameters, mirror cleanliness and mirror alignment drift are negligible. Drift in filtered air extinction measurements is largely due to changes in concentrations of ambient absorbing and scattering gasses. Filtered air extinction measurements should be made before and after every sample or every hour during an extended sample to account for possible changes in levels of absorbing and scattering gasses.

During FLAME2, an ammonium sulfate calibration was performed on the CRD, TSI nephelometer and CSU sizing rack. Subsequent comparisons demonstrated good agreement between TSI nephelometer measured scattering coefficients and scattering coefficients predicted from theory. CRD measured extinction coefficients demonstrated a need for a constant correction of 1.353 inconsistent with the ±10% accuracy determined from the PSL tests. Upon further investigation it was found that the raw CRD signal decay was contaminated by exponential decays likely due to the PMT and PMT

electronics. FLAME2 CRD extinction coefficient measurements corrected using the factor detected in the ammonium sulfate calibrations yielded good instrument closure (CRD extinction coefficients = TSI nephelometer scattering + PAS absorption coefficients) throughout the study with an $r^2 = 0.998$.

We used measurements of extinction, scattering and absorption coefficients in FLAME2, together with size distribution information to estimate SSA and to retrieve the complex refractive index for each burn. Optical closure was demonstrated between the CRD, TSI nephelometer and PAS. Good closure was found between measurements of extinction coefficient and scattering + absorption coefficients with an $r^2 = 0.999$; similarly. Although an $r^2 = 0.443$ was obtained between measurements of absorption and extinction – scattering measurements, good closure for all magnitudes of absorption was found with a regression of 0.972. A broad range of SSA values was measured during this study, with values from ranging 0.43 to 1. Fuels burned multiple times produced measured SSAs very close in value indicating consistency between replicates. A strong relationship between SSA and EC_a mass fraction was found, with a correlation of $r^2 = -0.942$, in agreement with suggestions that EC_a is a good indicator of the mass fraction of absorbing material present in the sample. FLAME2 SSA values were bounded by values reported in the literature. It was also demonstrated that the combustion conditions (flaming, smoldering or aged) are a better indicator of the expected SSA than fuel type, despite prior attempts at relating SSA only to the fuel type.

Refractive indices were retrieved for six burns after various corrections were made to the measured size distributions. Measured size distributions required corrections because non-spherical particles were likely present for burns with large contributions from absorption, or the measured size distributions did not capture the full aerosol size distribution. FLAME2 retrieved refractive indices were in the same general range as literature values for similar fuels. FLAME2 retrieved refractive indices covered a wider range of real, n, and imaginary, k, parts of the refractive index. Many of the literature reported values of refractive index were retrieved for ambient, aged smokes. Differences in combustion conditions between fresh FLAME2 aerosols and aged plumes could reflect the uptake of water and atmospheric gasses and aerosols depositing onto the biomass smoke, altering the refractive index.

6.2 Future work

The work presented here brought up several issues that should be investigated. Before the CRD is used in more studies it is important that the accuracy of the instrument and the data processing algorithms be further studied. The cause of error in the FLAME2 data was found to most likely be due to the PMT used in the CRD during the study. A SUVA gas calibration performed using a different PMT indicated accuracy within 1%, but the accuracy over the full range of the CRD should be tested. This could be accomplished by repeating the PSL or ammonium sulfate calibrations or by comparison with another CRD which is known to be accurate. Measurements should be made so that

the full range of the CRD is tested. Signal decays should also be saved and examined to determine whether noise is present in the signal or whether the exact magnitude of the noise can be determined.

The method used in this work to retrieve refractive index has good potential, but was found to be best for highly idealized cases, i.e. spherical particles with SSA > 0.85. It was severely limited by the measured size distributions which did not cover all of the relevant diameters. Large uncertainties in the volume distributions due to multiply charged particles and shape factor also had a large influence on the retrieved index of refraction, *n*. An alternative approach, similar to how [*Dinar et al.*, 2008] retrieved refractive indices for HUmic-Like Substances (HULIS), would eliminate many of the problems encountered with size distributions. Using this method, aerosols produced by biomass burning would be size selected by a DMA and the monodisperse particles measured for number concentration, extinction, scattering and/or absorption coefficients. Using the measured particle size, number concentrations and Mie theory, the refractive index would be varied in the model until the calculated extinction, scattering and/or absorption coefficients agreed with measured values. This process could be repeated for a range of particle sizes and the best fit refractive index found for all particle sizes. For real time measurements, this could be performed rapidly as only a few minutes are needed to measure at each particle diameter. For samples of up to 10 separate diameters, this might be accomplished in time scales of under 20 minutes, where individual estimates of refractive index at each diameter could be obtained every several minutes.

This process could be performed for fresh aerosols samples or samples collected onto a filter. Samples collected on filters could be extracted and re-aerosolized and the experiment could be performed in the laboratory with a constant aerosol supply. With a good extraction technique this process might be able to be used for filters collected during the stack and chamber burns performed during FLAME2. This alternative technique for refractive index measurements would eliminate size distribution problems associated with the optical response of the OPC and would not require that the full size distribution be measured. However, the extraction and re-aerosolization process would likely alter the shape and composition of the particles causing large uncertainty for highly absorbing aerosols where non-spherical particles are likely. If this technique were to work accurately on samples from filters obtained from FLAME2, a more complete list of refractive indices could be obtained as well as comparisons made with refractive indices reported here.

Absorption caused by aerosols produced by biomass burning is often attributed to only black carbon (BC) or soot carbon (C_{soot}). Recent studies have demonstrated that there is in fact organic carbon (OC), originally thought to cause no absorption, in many samples that causes absorption in the visible and UV and this has been called brown carbon, C_{brown}. Brown carbon is unique because it causes absorption with a strong spectral dependence such that absorption is much greater in the ultra-violet (UV) than the visible [*Andreae and Gelencser*, 2006; *Kirchstetter et al.*, 2004]. Absorption caused by C_{brown} might cause modeled absorption due to biomass burning to be larger than

previously predicted. Because of the strong wavelength dependence of C_{brown}, it would be possible to detect its presence in samples with measurement of the optical properties at both visible and UV wavelengths. With the addition of a second CRD in the UV, it might be possible see evidence of C_{brown} in aerosol samples as well as determine the optical properties of C_{brown}. The index of refraction retrieval might then be repeated with measurements of extinction in the UV.

REFERENCES

Abel, S. J., et al. (2003), Evolution of biomass burning aerosol properties from an agricultural fire in southern Africa, *Geophysical Research Letters*, *30*(15).

Anderson, T. L., et al. (1996), Performance characteristics of a high-sensitivity, three-wavelength, total scatter/backscatter nephelometer, *Journal of Atmospheric and Oceanic Technology*, *13*(5), 967-986.

Anderson, T. L., and J. A. Ogren (1998), Determining aerosol radiative properties using the TSI 3563 integrating nephelometer, *Aerosol Science and Technology*, *29*(1), 57-69.

Andreae, M. O., and A. Gelencser (2006), Black carbon or brown carbon? The nature of light-absorbing carbonaceous aerosols, *Atmospheric Chemistry and Physics*, *6*, 3131-3148.

Arnott, W. P., et al. (1999), Photoacoustic spectrometer for measuring light absorption by aerosol: instrument description, *Atmospheric Environment*, *33*(17), 2845-2852.

Arnott, W. P., et al. (2000), Nitrogen dioxide and kerosene-flame soot calibration of photoacoustic instruments for measurement of light absorption by aerosols, *Review of Scientific Instruments*, *71*(12), 4545-4552.

Baron, P. A., and K. Willeke (2001), *Aerosol measurement : principles, techniques, and applications*, 2nd ed., xxiii, 1131 p. pp., Wiley-Interscience, New York.

Baynard, T., et al. (2007), Design and application of a pulsed cavity ring-down aerosol extinction spectrometer for field measurements, *Aerosol Science and Technology*, *41*(4), 447-462.

Berden, G., et al. (2000), Cavity ring-down spectroscopy: Experimental schemes and applications, *International Reviews in Physical Chemistry*, *19*(4), 565-607.

Bohren, C. F., and D. R. Huffman (1983), *Absorption and Scattering of Light by Small Particles*, J.Wiley & Sons, New York.

Bond, T. C., et al. (1999), Calibration and intercomparison of filter-based measurements of visible light absorption by aerosols, *Aerosol Science and Technology*, *30*(6), 582-600.

Bond, T. C., and R. W. Bergstrom (2006), Light absorption by carbonaceous particles: An investigative review, *Aerosol Science and Technology*, *40*(1), 27-67.

Bucholtz, A. (1995), Rayleigh-scattering calculations for the terrestrial atmosphere, *Applied Optics*, *34*(15), 2765-2773.

Bulatov, V., et al. (2002), Aerosol analysis by cavity-ring-down laser spectroscopy, *Analytica Chimica Acta*, *466*(1), 1-9.

Chen, L. W. A., et al. (2006), Particle emissions from laboratory combustion of wildland fuels: In situ optical and mass measurements, *Geophysical Research Letters*, *33*(4).

Colarco, P. R., et al. (2004), Transport of smoke from Canadian forest fires to the surface near Washington, D. C.: Injection height, entrainment, and optical properties, *Journal of Geophysical Research-Atmospheres*, *109*(D6).

Crutzen, P. J., and M. O. Andreae (1990), Biomass burning in the tropics - impact on atmospheric chemistry and biogeochemical cycles, *Science*, *250*(4988), 1669-1678.

Dinar, E., et al. (2008), The complex refractive index of atmospheric and model humic-like substances (HULIS) retrieved by a cavity ring down aerosol spectrometer (CRD-AS), *Faraday Discussions*, *137*, 279-295.

Dubovik, O., et al. (2002), Variability of absorption and optical properties of key aerosol types observed in worldwide locations, *Journal of the Atmospheric Sciences*, *59*(3), 590-608.

Garland, R. M., et al. (2007), Parameterization for the relative humidity dependence of light extinction: Organic-ammonium sulfate aerosol, *Journal of Geophysical Research-Atmospheres*, *112*.

Giglio, L., et al. (2006), Global estimation of burned area using MODIS active fire observations, *Atmospheric Chemistry and Physics*, *6*, 957-974.

Guyon, P., et al. (2003), Refractive index of aerosol particles over the Amazon tropical forest during LBA-EUSTACH 1999, *Journal of Aerosol Science*, *34*(7), 883-907.

Hand, J. L. (2001), A New Tecnhique for Obtaining Aerosol Size Distributions with Applications to Estimates of Aerosol Properties, 245 pp, Colorado State University, Fort Collins.

Hand, J. L., et al. (2002), Comparisons of aerosol properties measured by impactors and light scattering from individual particles: refractive index, number and volume concentrations, and size distributions, *Atmospheric Environment*, *36*(11), 1853-1861.

Hansen, J., et al. (1981), Climate impact of increasing atmospheric carbon-dioxide, *Science*, *213*(4511), 957-966.

Hinds, W. C. (1982), *Aerosol technology : properties, behavior, and measurement of airborne particles*, xix, 424 p. pp., J. Wiley, New York.

Hobbs, P. V., et al. (1996), Particle and trac-egas measurements in smoke from prescribed burns of forest products in the Pacific Northest, in *Biomass Burning and Global Change*, edited by J. S. Levine, pp. 697-715, MIT Press, New York.

Holden, A. (2008), Estimating contributions of primary biomass burning to fine particulates in ambient aerosol in the western United States, Colorado State University.

Hungershoefer, K., et al. (2008), Modelling the optical properties of fresh biomass burning aerosol produced in a smoke chamber: results from the EFEU cambaign, *Atmospheric Chemistry and Physics*, 3427 - 3439.

Kirchstetter, T. W., et al. (2004), Evidence that the spectral dependence of light absorption by aerosols is affected by organic carbon, *Journal of Geophysical Research-Atmospheres*, *109*(D21).

Kuzmanoski, M., et al. (2007), Case study of modeled aerosol optical properties during the SAFARI 2000 campaign, *Applied Optics*, *46*(22), 5263-5275.

Lack, D. A., et al. (2006), Aerosol absorption measurement using photoacoustic spectroscopy: Sensitivity, calibration, and uncertainty developments, *Aerosol Science and Technology*, *40*, 697-708.

Levin, E. J. T. (2008), The role of aerosols on visibility degredation during two field campaigns, Colorado State University, Fort Collins.

Lewis, K. (2007), Development of a Dual-Wavelength Photoacoustic Instrument for Measurement of Light Absorption and Scattering by Aerosol and Gases, 156 pp, University of Nevada, Reno.

Lewis, K., et al. (2008), Strong spectral variation of biomass smoke light absorption and single scattering albedo observed with a novel dual-wavelength photoacoustic instrument, *Journal of Geophysical research*, *113*(D16203).

Liousse, C., et al. (1996), A global three-dimensional model study of carbonaceous aerosols, *Journal of Geophysical Research-Atmospheres*, *101*(D14), 19411-19432.

Martins, J. V., et al. (1998), Sphericity and morphology of smoke particles from biomass burning in Brazil, *Journal of Geophysical Research-Atmospheres*, *103*(D24), 32051-32057.

McMeeking, G. (2008), The optical, chemical, and physical properties of aerosols and gases emitted by the laboratory combustion of wildland fuels, Colorado State University.

McMeeking, G. R., et al. (2005), Observations of smoke-influenced aerosol during the Yosemite Aerosol Characterization Study: Size distributions and chemical composition, *Journal of Geophysical Research-Atmospheres*, *110*(D9).

Miller, J. R., and N. T. O'Neill (1997), Multialtitude airborne observations of insolation effects of forest fire smoke aerosols at BOREAS: Estimates of aerosol optical parameters, *Journal of Geophysical Research-Atmospheres*, *102*(D24), 29729-29736.

Moosmuller, H., et al. (2005), Cavity ring-down and cavity-enhanced detection techniques for the measurement of aerosol extinction, *Aerosol Science and Technology*, *39*(1), 30-39.

Okeefe, A., and D. A. G. Deacon (1988), Cavity ring-down optical spectrometer for absorption-measurements using pulsed laser sources, *Review of Scientific Instruments*, *59*(12), 2544-2551.

Patterson, E. M., and C. K. McMahon (1984), Absorption characteristics of forest fire particulate matter, *Atmospheric Environment*, *18*(11), 2541-2551.

Pettersson, A., et al. (2004), Measurement of aerosol optical extinction at 532nm with pulsed cavity ring down spectroscopy, *Journal of Aerosol Science*, *35*(8), 995-1011.

Procopio, A. S., et al. (2003), Modeled spectral optical properties for smoke aerosols in Amazonia, *Geophysical Research Letters*, *30*(24).

Radke, L. F., et al. (1988), Airborne measurements on smokes from biomass burning, in *Aerosols and climate*, edited by P. V. Hobbs and M. P. McCormick, pp. 411-422, Deepak Publishing, Hampton, VA.

Radke, L. F., et al. (1991), Particulate and trace emissions from large biomass fires in North America, in *Global Biomass Burning: Atmospheric, Climatic, and Biospheric Implications*, edited by J. S. Levine, pp. 209-224, MIT Press, Cambridge, MA.

Reid, J. S., and P. V. Hobbs (1998), Physical and optical properties of young smoke from individual biomass fires in Brazil, *Journal of Geophysical Research-Atmospheres*, *103*(D24), 32013-32030.

Reid, J. S., et al. (2005), A review of biomass burning emissions part III: intensive optical properties of biomass burning particles, *Atmospheric Chemistry and Physics*, *5*, 827-849.

Riziq, A. A., et al. (2007), Optical properties of absorbing and non-absorbing aerosols retrieved by cavity ring down (CRD) spectroscopy, *Atmospheric Chemistry and Physics*, *7*(6), 1523-1536.

Sappey, A. D., et al. (1998), Fixed-frequency cavity ringdown diagnostic for atmospheric particulate matter, *Optics Letters*, *23*(12), 954-956.

Schkolnik, G., et al. (2007), Constraining the density and complex refractive index of elemental and organic carbon in biomass burning aerosol using optical and chemical measurements, *Atmospheric Environment*, *41*(5), 1107-1118.

Seinfeld, J. H., and S. N. Pandis (2006), *Atmospheric chemistry and physics : from air pollution to climate change*, 2nd ed., xxviii, 1203 p. pp., Wiley, Hoboken, N.J.

Sheridan, P. J., et al. (2005), The Reno Aerosol Optics Study: An evaluation of aerosol absorption measurement methods, *Aerosol Science and Technology*, *39*(1), 1-16.

Smith, J. D., and D. B. Atkinson (2001), A portable pulsed cavity ring-down transmissometer for measurement of the optical extinction of the atmospheric aerosol, *Analyst*, *126*(8), 1216-1220.

Strawa, A. W., et al. (2003), The measurement of aerosol optical properties using continuous wave cavity ring-down techniques, *Journal of Atmospheric and Oceanic Technology*, *20*(4), 454-465.

Thompson, J. E., et al. (2002), Monitoring atmospheric particulate matter through cavity ring-down spectroscopy, *Analytical Chemistry*, *74*(9), 1962-1967.

Thompson, J. E., et al. (2003), Atmospheric aerosol measurements by cavity ringdown turbidimetry, *Aerosol Science and Technology*, *37*(3), 221-230.

von Hoyningen-Huene, W., et al. (1999), Climate relevant aerosol parameters of South East-Asian forest fire haze, *Atmospheric Environment*, 1891 - 1909.

Watson, J. G. (2002), Visibility: Science and regulation, *Journal of the Air & Waste Management Association*, *52*(6), 628-713.

Westphal, D. L., and O. B. Toon (1991), Simulations of microphysical, radiative, and dynamic processes in a continental-scale forest-fire smoke plume, *Journal of Geophysical Research-Atmospheres*, *96*(D12), 22379-22400.

Willeke, K., and P. A. Baron (1993), *Aerosol measurement : principles, techniques, and applications*, xviii, 876 p. pp., Van Nostrand Reinhold, New York.

Yamasoe, M. A., et al. (1998), Retrieval of the real part of the refractive index of smoke particles from Sun/sky measurements during SCAR-B, *Journal of Geophysical Research-Atmospheres*, *103*(D24), 31893-31902.

APPENDIX A: MIE CODE AND CORRECTION FOR TSI NEPHELOMETER ANGULAR NON-IDEALITIES

A.1 Mie code instructions

Three inputs are needed for the Mie code listed in ***A.2 Mie Code with angular non-idealities correction***, the angular response function of the TSI 3565 nephelometer (*response_function.txt*), a file with the wavelength and refractive index (*wavelength.dat*) and the array of diameters (*dp.dat*).

The code is currently set up for a diameter array of 59 diameters, if a different number of diameters is used, the loop where file 18 is read in must be changed in the Mie code to reflect the new number of diameters. To properly read in the array of diameters, *dp.dat* must be in the form of a column.

The file *wavelength.dat* consists of: the real part of the refractive index, *n*, the imaginary part of the refractive index, *k*, and the wavelength of interest in *nm* listed in that order.

The response function of the TSI nephelometer as obtained from T. Anderson in June 2008, is shown below in ***A.3 Response function of TSI nephelometer***, column 2. For input into the Mie Code, the angular response function was extrapolated for an array of 1599 angles from 0 to π by an increment of $d\theta = \frac{\pi/2}{(800-1)}$ = 0.001965953 radians to match the choices of angles in the main program. The input file *response_function.txt* then consists of the columns: 1 – *Angle in radians, 2 – Angle in degrees, 3 – sin of the angle, 4 – extrapolated response function*.

A.2 Mie Code with angular non-idealities correction

```
C NEW PROGRAM TO CALL MIE CODE AND COMPUTE OPTICAL PROPERTIES
C SK GOT THIS CODE FROM NORM; HE FIXED IT IN AT772 TO GET PHASE FUNCTIONS
C I AM CHANGING THIS TO INTEGRATE FOR BACKSCATTER FRACTION, FROM 90 DEG TO
180
C CHANGES MADE 28 MAY 2004
C Changing number of angles from 90 to 200 20 Sept 2004
C Adding sums for neph truncation angles 16 August 2004
C Modifying to Output all variables into file 15 9 dec 2004
C
          IMPLICIT REAL*8 (A-H,O-Z)
       DOUBLE PRECISION RM1, RM2,XX, X2, Q180, QEXT, QSCA, G
       DOUBLE PRECISION PFUNC, DANG, ANG, PI, SIG_SCA, WVNM
             DOUBLE PRECISION BACKFRACTION, NEPHBACKFRACTION
             DOUBLE PRECISION QNEPH, QABS, QNEPHBACK, QBACK
        DOUBLE PRECISION IT_DOUBLE
        INTEGER NFILE
       PARAMETER (PI=3.1415927)
       PARAMETER (NFILE = 1599)
       DOUBLE PRECISION ANG2(NFILE),response(NFILE),d1(NFILE),
     &       d2(NFILE),d3(NFILE)
       INTEGER NANG
       PARAMETER(NANG = 800)
       DIMENSION S1(NANG*2-1), S2(NANG*2-1)
      COMPLEX*16 S1, S2
          OPEN(15,FILE='/home/lmack/Mie/bext.OUT', STATUS='unknown')
      OPEN(16,FILE='/home/lmack/Mie/pfunc.OUT',STATUS='unknown')
      OPEN(17,FILE='/home/lmack/Mie/sumsangles.OUT',STATUS='unknown')
      OPEN(18,FILE='/home/lmack/Mie/Dp.dat', STATUS='OLD')
      OPEN(19,FILE='/home/lmack/Mie/backscat.OUT', STATUS='unknown')
      OPEN(20,FILE='/home/lmack/Mie/wavelength.dat',STATUS='OLD')
      OPEN(21,FILE='/home/lmack/Mie/response_function.txt',
     &  STATUS='unknown')


C     READ IN TSI NEPH RESPONSE FUNCTION
      READ(21,54)
 54     format(/)
      DO i = 1, NFILE
      READ(21,55) ANG2(i), d1(i),d2(i),response(i)
 55     format(d13.11,1x,d13.11,1x,d13.11,1x,d13.11)
      ENDDO


C SET PARAMETERS

C     REAL PART OF REFRACTIVE INDEX

      READ(20,*) RM1
C     IMAGINARY PART OF REFRACTIVE INDEX

      READ(20,*) RM2
```

```
      SUMBSCA = 0.
      SUMBEXT = 0.
      SUMBACKNEPH = 0.
C
C SET UP TO SCAN SIZE PARAMETER
C
      READ(20,*) wavel

            WRITE(15,*) "DIAM RM1 RM2 WAVEL XX G Q180 QABS QEXT
     &      QSCA QNEPH QBACK QNEPHBACK"
       DO 100 I=1,59
         READ(18,*) DIAM
       XX = 2.*(3.141593)*(DIAM/2.)/WAVEL
          CALL ABFUNC(RM1,RM2,XX,X2,Q180,QEXT,QSCA,G,NANG,S1,S2)
c
c when Qsca is returned, compute sum to get Bsca and output to screen
c
      SUMBSCA = SUMBSCA + PI*QSCA*DNUM*(DIAM**2)/4.

 223    format(1x, 'sum of bsca =', e15.4)

C      CODE ADDED TO SUPPORT OUTPUT OF PHASE FUNCTION
C FOR EACH SIZE, WE WILL INTEGRATE OVER 180 DEG
C AND THEN INTEGRATE FROM 90 TO 180 DEG
C RATIO IS BACKSCATTER FRACTION
C CURRENTLY DOES APPROX INTEGRAL, CAN IMPROVE THIS LATER`
      DANG = (PI/2.)/(NANG-1)
      WVNM = 2*PI/WAVEL

      WRITE(16,*) DIAM
      WRITE(16,*)"ANGLE    PHASE FUNCTION"
      ANG=0.
      SUMALLANG=0.
            SUMNEPHTOT=0.
      SUMBACKANG=0.
            SUMNEPHBACK=0.

     DO 90 J=1,NANG*2-1
        SIG_SCA = QSCA*PI*DIAM

        RESP = response(j)
        SINANG = SIN(ANG)

        IT_DOUBLE = S1(j)*CONJG(S1(j))+S2(j)*CONJG(S2(j))

        PFUNC=(4.*PI)/(2*WVNM**2*SIG_SCA)*
     &      (S1(J)*CONJG(S1(J))+S2(J)*CONJG(S2(J)))

         WRITE(16,*) ANG*180/PI, PFUNC
      SUMALLANG=SUMALLANG+(PFUNC*SINANG*DANG)
      IF(ANG*180/PI.GE.7.0.AND.ANG*180/PI.LE.170.0) THEN
            SUMNEPHTOT=SUMNEPHTOT +(PFUNC*RESP*DANG)

            ENDIF
     IF(ANG*180/PI.GE.90.0) SUMBACKANG=SUMBACKANG+(PFUNC*SINANG*DANG)
            IF(ANG*180/PI.GE.90.0.AND.ANG*180/PI.LE.180.0) THEN
```

```
              SUMNEPHBACK=SUMNEPHBACK+(PFUNC*RESP*DANG)
             ENDIF
C  Changed this condition from j to angular degrees for backscatter sum 19 July 2004
                    If (ANG*180/PI.EQ.180.0) THEN
           write(17,*)ANG*180/PI,SUMALLANG,SUMBACKANG,SUMNEPHTOT,SUMNEPHBACK
       ENDIF

                     ANG = ANG+DANG
  90   CONTINUE
C
C NOW TAKE THE RATIO
C

      BACKFRACTION = SUMBACKANG/SUMALLANG
           NEPHBACKFRACTION = SUMNEPHBACK/SUMNEPHTOT
           QABS=QEXT-QSCA
           QBACK=QSCA*SUMBACKANG/SUMALLANG
           QNEPH=QSCA*SUMNEPHTOT/SUMALLANG
           QNEPHBACK=QNEPH*SUMNEPHBACK/SUMNEPHTOT
      WRITE(19, *) DIAM, BACKFRACTION, NEPHBACKFRACTION
          WRITE(15,10) DIAM, RM1, RM2, WAVEL, XX, G, Q180, QABS,QEXT,
   & QSCA, QNEPH, QBACK, QNEPHBACK
 10         FORMAT(6F9.5,7E13.5)


      SUMBEXT = SUMBEXT + PI*QEXT*DNUM*(DIAM**2)/4.
C       write(*,224) SUMBEXT
 224    format(1x, 'sum of bext =', e15.4)

      SUMBACKNEPH = SUMBACKNEPH +
   +    PI*QNEPHBACK*DNUM*(DIAM**2)/4.
C       write(*,225) SUMBACKNEPH
 225    format(1x, 'sum of backneph =', e15.4)


  100   CONTINUE
       CLOSE(16)
       CLOSE (19)
        STOP
           END


C ---------------------------------------------------------------------2
     SUBROUTINE ABFUNC(RM1,RM2,XX,X2,Q180,QEXT,QSCA,G,NANG,S1,S2)
C ---------------------------------------------------------------------2

      IMPLICIT REAL*8 (A-H,O-Z)
      COMPLEX*16 N1,AMIE(6000),BMIE(6000), QB
      DOUBLE PRECISION ZERO, ONE, TWO, FOUR
      PARAMETER (ZERO = 0.0, ONE = 1.0, TWO = 2.0, FOUR = 4.0)
C -- VARIABLES FOR ANGULAR SCATTERING:
      INTEGER N, RN, J, JJ, NANG, MAXANG
      PARAMETER (MAXANG = 1600)
     COMPLEX*16 S1(MAXANG), S2(MAXANG)
     DOUBLE PRECISION FN, AMU(MAXANG)
     DOUBLE PRECISION TAU(MAXANG), PI(MAXANG), PI1(MAXANG), PI0(MAXANG)
```

```
      REAL THETA(MAXANG)
      DOUBLE PRECISION RM1, RM2,XX, X2, Q180, QEXT, QSCA, G


C
C      WRITE(*,11)
  11   FORMAT(1X,'IN ABFUNC')

      X2=XX*XX
C     GRAEME SET NLIMIT TO:    NLIMIT = INT(1.2*XX + 10.)
      NLIMIT = MAX(12,INT(3*XX**(1./3.) + XX))
      IF (NLIMIT .GT. 4000) THEN
        WRITE(4,*) 'WARNING:  RESETTING NLIMIT = 4000', XX
        NLIMIT = 4000
      END IF
      N1 = DCMPLX(RM1,RM2)
      CALL LRNZMIE(0, 0, NLIMIT, N1, XX, AMIE, BMIE)
C
C      WRITE(*,12)
  12   FORMAT(1X,'BACK IN ABFUNC')

      QE=ZERO
      QS=ZERO
      QB=ZERO
      GQS=ZERO
      U = -ONE
      DO 10 N=1, NLIMIT
        ANR = DBLE(AMIE(N))
        ANI = DIMAG(AMIE(N))
        BNR = DBLE(BMIE(N))
        BNI = DIMAG(BMIE(N))
        RA = 2*N+1
        QE = QE + RA*DBLE(AMIE(N) + BMIE(N))
        QS = QS + RA*( (ANR**2+ANI**2) + (BNR**2+BNI**2) )
        QB = QB + RA*U*(AMIE(N) - BMIE(N))
        U = -U
        IF (N .GT. 1) THEN
          RA1 = DBLE(N*N - 1)/DBLE(N)
          RA2 = DBLE(2*N - 1)/DBLE(N*(N - 1))
          GQS = GQS +
     .        RA1*DBLE( AMIE(N-1)*DCONJG(AMIE(N)) +
     .                BMIE(N-1)*DCONJG(BMIE(N)) ) +
     .        RA2*DBLE( AMIE(N-1)*DCONJG(BMIE(N-1)) )
        END IF
  10    CONTINUE

C
C          WRITE(*,13)
  13       FORMAT(1X,'DONE WITH QE LOOP')

C SKIP THIS SECTION - CAUSING TROUBLE

C        GO TO 555

C -- COMPUTE FULL PHASE FUNCTION:
C      NANG = NUMBER OF ANGLES BETWEEN 0 AND 90 DEGREES.
```

```
C      MATRIX ELEMENTS CALCULATED AT 2 * NANG - 1 ANGLES
C      INCLUDING 0, 90, 180 DEGREES.
C -- TEMPORARILY HARDWIRE # OF SCATTERING ANGLES:
C     NANG = 90

      IF(NANG .LE. 0) GO TO 999
      DANG = 1.570796327/FLOAT(NANG - 1)

      DO J = 1, NANG
        THETA(J) = (FLOAT(J) - 1.)*DANG
        AMU(J) = DBLE(COS(THETA(J)) )
        PI0(J) = 0.0
        PI1(J) = 1.0
      END DO

      NN = 2 * NANG - 1
      DO J = 1, NN
        S1(J) =CMPLX(0.0,0.0)
        S2(J) =CMPLX(0.0,0.0)
      END DO

      DO 400 N = 1, NLIMIT
        RN = N
        FN = DBLE( (2.*RN + 1.)/(RN*(RN + 1.)) )
        DO 200 J = 1, NANG
          JJ = 2*NANG - J
          PI(J) = PI1(J)
          TAU(J) = RN*AMU(J)*PI(J) - (RN + 1.)*PI0(J)
          S1(J) = S1(J) + FN*(AMIE(N)*PI(J)  + BMIE(N)*TAU(J))
          S2(J) = S2(J) + FN*(AMIE(N)*TAU(J) + BMIE(N)*PI(J))
          IF (J.EQ.JJ) GO TO 200
          P = (-1.)**(N - 1)
          T = (-1.)**N
          S1(JJ) = S1(JJ) + FN*(AMIE(N)*PI(J)*P  + BMIE(N)*TAU(J)*T)
          S2(JJ) = S2(JJ) + FN*(AMIE(N)*TAU(J)*T + BMIE(N)*PI(J)*P)
 200    CONTINUE
        RN = N + 1
        DO 300 J = 1, NANG
          PI1(J) = ( (2.*RN - 1.)/(RN - 1.)*AMU(J)*PI(J) )
          PI1(J) = PI1(J) - RN*PI0(J)/(RN - 1.)
          PI0(J) = PI(J)
 300    CONTINUE
 400  CONTINUE
C     WRITE(4,*) 'S1,S2 = ', S1(1), S2(J)
 999  CONTINUE

C
C  555      WRITE(*,14)
   14      FORMAT(1X,'DONE WITH PHASE FUNCTION LOOP')

C NOTE: THE NEGATIVE SIGN IS DUE TO KIRK FULLERS CONVENTION IN COMPUTING
C  THE AN AND BN EXPANSION COEFFICIENTS.
      QEXT = -TWO*QE/X2
      QSCA = TWO*QS/X2
C     Q180 = (DBLE(QB)*DBLE(QB) + DIMAG(QB)*DIMAG(QB))/X2
      Q180 = DBLE(QB*DCONJG(QB))/X2
```

```
      G  = FOUR/X2*GQS/QSCA
C     WRITE(4,*) XX, QSCA, G

      RETURN
      END



C***********************************************************************
      SUBROUTINE LRNZMIE(IQABS,METAL,TRNCPT,N1,KA,AMIE,BMIE)
C***********************************************************************
C THIS ALGORITHM DERIVES FROM THE ONE DISCUSSED IN THE PAPER ``RAINBOWS:
C  MIE COMPUTATIONS AND THE AIRY APPROXIMATION'' BY RU T. WANG AND H. C.
C  VAN DE HULST, IN APPL. OPT. VOL. 30, 106-117(1991).
C
C  IMPLEMENTED BY KIRK FULLER:
C
      IMPLICIT NONE
      INTEGER IQABS,METAL,NMAX
      PARAMETER(NMAX=10000)
      INTEGER DWNWRD,ITEST,MODZ,N,NDOWN,TRNCPT
      REAL*4 FWIS,IMN1,MTLTST,REN1
      REAL*8 X, KA, A(NMAX),P(NMAX+1),PSI(NMAX),CHI(NMAX)
      COMPLEX*16 I,ONE,Z
      COMPLEX*16 ALPHA,N1,TMP
      COMPLEX*16 AMIE(6000),BMIE(6000),CMIE(6000),DMIE(6000)
      COMPLEX*16 ZA(NMAX),ZP(NMAX),PI1,PI2,R1,Y1,Y2,ZPSI(NMAX)

      DATA I,ONE /(0.0D0,1.0D0),(1.0D0,0.0D0)/
      MTLTST=CDABS(N1)
C
C       WRITE(*,11)
  11   FORMAT(1X,'IN LRNZMIE')

C FIX:      MTLTST=CABS(CMPLX(N1))
      IF(MTLTST.GE.500000) METAL=1
      X=KA
      Z=N1*KA
C   TEST FOR THE NEED OF DOWNWARD RECURSION USING WISCOMBES CRITERIA.
      DWNWRD=0
      REN1=SNGL(DBLE(N1))
C      REN1=REAL(N1)
      IMN1=DIMAG(N1)
      FWIS=13.78*REN1**2 - 10.8*REN1 + 3.9
      ITEST=NINT(IMN1*KA)
      IF(ITEST.GT.INT(FWIS)) DWNWRD=1
C     IF(METAL.EQ.1) DWNWRD=1
C    END OF DOWNWARD RECURSION TESTS.

C     WRITE(4,*) 'METAL=',METAL
      IF(METAL.EQ.1) GO TO 50

      IF(DWNWRD.EQ.1)THEN
        WRITE(4,*) 'DOWNWARD RECURSION HAS BEEN SELECTED IN LRNZMIE.'
        MODZ=IDNINT(CDABS(Z))
        IF (MODZ.LE.10000) NDOWN=1.10*INT(CDABS(Z))+10
```

```
        IF (MODZ.GT.10000) NDOWN=1.01*INT(CDABS(Z))+10
        ZP(NDOWN+1)=Z/(2*NDOWN+3)
        DO N=NDOWN,1,-1
          ZP(N)=(2*N+1)/Z - ZP(N+1)
          ZP(N)=1./ZP(N)
          ZA(N)=-N/Z + 1/ZP(N)
        ENDDO
      ELSEIF(DWNWRD.EQ.0)THEN
        IF(CDABS(Z).LT.1.0D-4)THEN
          ZP(1)=Z/3 +Z**3/45
        ELSE
          ZP(1)=1/Z - CDCOS(Z)/CDSIN(Z)
C FIX:    ZP(1)=1/Z - CCOS(CMPLX(Z))/CSIN(CMPLX(Z))
        ENDIF
        ZA(1)=-1/Z + 1/ZP(1)
        DO N=2,TRNCPT
          ZP(N)=(2*N-1)/Z - 1/ZP(N-1)
          ZA(N)=-N/Z + 1/ZP(N)
        ENDDO
      ENDIF

 50   IF(DABS(X).LT.1.0D-4)THEN
        P(1)=X/3 +X**3/45
      ELSE
        P(1)=1/X - 1/DTAN(X)
      ENDIF

      PSI(1)=DSIN(X)/X - DCOS(X)
      PSI(2)=DSIN(X)*(3/X**2 - 1) - 3*DCOS(X)/X
      IF(IQABS.EQ.1)THEN
      WRITE(4,*) 'IT IS ASSUMED THAT IM(NDX) IS SMALL ENOUGH TO ALLOW
     . CALCULATION OF PSI(Z) BY FORWARD RECURSION.'
        ZPSI(1)=CDSIN(Z)/Z - CDCOS(Z)
        ZPSI(2)=CDSIN(Z)*(3/Z**2 - 1) - 3*CDCOS(Z)/Z
      ENDIF
      CHI(1)=-DCOS(X)/X - DSIN(X)
      CHI(2)=-DCOS(X)*(3/X**2 - 1) - 3*DSIN(X)/X

      DO N=1,TRNCPT
        IF (N.GT.1) P(N)=(2*N-1)/X - 1/P(N-1)
        IF(N.GT.2)THEN
           PSI(N)=(2*N-1)*PSI(N-1)/X - PSI(N-2)
           IF(IQABS.EQ.1) ZPSI(N)=(2*N-1)*ZPSI(N-1)/Z - ZPSI(N-2)
           CHI(N)=(2*N-1)*CHI(N-1)/X - CHI(N-2)
        ENDIF
          A(N)=-N/X + 1/P(N)
          R1=CHI(N)/PSI(N)
          PI1=CHI(N)*PSI(N)
          Y1=ZA(N)-N1*A(N)
          Y2=N1*ZA(N)-A(N)
        IF(METAL.NE.1)THEN
          AMIE(N)=1+I*R1*(1 - N1/(PI1*Y1))
          BMIE(N)=1+I*R1*(1 - 1/(PI1*Y2))
          AMIE(N)=-1/AMIE(N)
          BMIE(N)=-1/BMIE(N)
        ELSE
```

```
        TMP=R1*(1+1/(A(N)*PI1))
        AMIE(N)=-1/(1+I*TMP)
        BMIE(N)=-1/(1+I*R1)
       ENDIF
       IF(IQABS.EQ.1)THEN
        PI2=ZPSI(N)*PSI(N)
        ALPHA=I/PI2
        CMIE(N)=N1*ALPHA*AMIE(N)/Y1
        DMIE(N)=N1*ALPHA*BMIE(N)/Y2
       ENDIF
      ENDDO

C  EXAMINE THE COEFFICIENTS.
C     DO N=1,TRNCPT
C       WRITE(4,100)  N, BMIE(N)
C       WRITE(4,101)  AMIE(N)
C     ENDDO

 100   FORMAT(4X,I5,4X,2(D24.16,1X))
 101   FORMAT(4X,5X,4X,2(D24.16,1X))

      RETURN
      END
```

A.3 Response function of TSI nephelometer

```
# TSI 3563 neph angular sensitivity functions for total scatter (ts)
#   and backscatter (bs)
# normalized to integrate to 2pi (for ts) and pi (for bs), just like
sine function
# sine function also included for reference
# includes opal glass transmission, backscatter shutter and forward and
#   backward truncation
# note that backward truncation was measured; forward truncation was
#   scaled off the mechanical drawings
# measured by goniometer in June, 1994 at the Nephelometer Workshop
#   at TSI (St Paul, Minnesota)
# angular sensitivity was identical (within measurement accuracy) for
#   all four units tested
# column 1 angle (degrees)
# column 2 neph angular sensitivity for total scatter
# column 3 reference sine function for total scatter
# column 4 neph angular sensitivity for backscatter
# column 5 reference sine function for backscatter
  0.00  0.00000e+00  0.00000e+00  0.00000e+00  0.00000e+00
  6.65  0.00000e+00  1.15804e-01  0.00000e+00  0.00000e+00
  6.94  3.89178e-02  1.20830e-01  1.73080e-05  0.00000e+00
  7.15  8.11842e-02  1.24467e-01  3.46890e-05  0.00000e+00
  8.10  9.63328e-02  1.40901e-01  3.50160e-05  0.00000e+00
 10.80  1.41221e-01  1.87381e-01  3.74510e-05  0.00000e+00
 13.50  1.86686e-01  2.33445e-01  4.05830e-05  0.00000e+00
 18.00  2.63154e-01  3.09017e-01  3.69870e-05  0.00000e+00
 27.00  4.16779e-01  4.53991e-01  2.53890e-05  0.00000e+00
 36.00  5.63933e-01  5.87785e-01  2.26050e-05  0.00000e+00
```

45.00	7.00587e-01	7.07107e-01	2.60850e-05	0.00000e+00
54.00	8.19514e-01	8.09017e-01	3.79150e-05	0.00000e+00
63.00	9.18703e-01	8.91007e-01	6.71440e-05	0.00000e+00
64.80	9.35308e-01	9.04827e-01	7.44520e-05	0.00000e+00
66.60	9.51582e-01	9.17755e-01	8.43110e-05	0.00000e+00
68.40	9.65857e-01	9.29776e-01	9.45180e-05	0.00000e+00
70.20	9.79834e-01	9.40881e-01	1.10290e-04	0.00000e+00
72.00	9.92678e-01	9.51057e-01	1.78730e-04	0.00000e+00
73.80	1.00410e+00	9.60294e-01	8.30337e-03	0.00000e+00
75.60	1.01445e+00	9.68583e-01	5.30383e-02	0.00000e+00
77.40	1.02380e+00	9.75917e-01	1.06910e-01	0.00000e+00
79.20	1.03143e+00	9.82287e-01	1.60947e-01	0.00000e+00
81.00	1.03853e+00	9.87688e-01	2.20443e-01	0.00000e+00
82.80	1.04452e+00	9.92115e-01	2.78504e-01	0.00000e+00
84.60	1.04918e+00	9.95562e-01	3.40825e-01	0.00000e+00
86.40	1.05178e+00	9.98027e-01	4.00321e-01	0.00000e+00
88.20	1.05371e+00	9.99507e-01	4.62783e-01	0.00000e+00
90.00	1.05485e+00	1.00000e+00	5.21458e-01	5.00000e-01
91.80	1.05467e+00	9.99507e-01	5.82742e-01	9.99507e-01
93.60	1.05288e+00	9.98027e-01	6.38998e-01	9.98027e-01
95.40	1.04991e+00	9.95562e-01	6.96840e-01	9.95562e-01
97.20	1.04646e+00	9.92115e-01	7.49858e-01	9.92115e-01
99.00	1.04075e+00	9.87688e-01	8.02824e-01	9.87688e-01
100.80	1.03456e+00	9.82287e-01	8.49940e-01	9.82287e-01
102.60	1.02694e+00	9.75917e-01	8.95333e-01	9.75917e-01
104.40	1.01797e+00	9.68583e-01	9.34425e-01	9.68583e-01
106.20	1.00777e+00	9.60294e-01	9.71503e-01	9.60294e-01
108.00	9.97084e-01	9.51057e-01	9.95200e-01	9.51057e-01
109.80	9.83719e-01	9.40881e-01	9.85987e-01	9.40881e-01
111.60	9.70935e-01	9.29776e-01	9.72956e-01	9.29776e-01
113.40	9.55672e-01	9.17755e-01	9.57851e-01	9.17755e-01
115.20	9.40599e-01	9.04827e-01	9.42535e-01	9.04827e-01
117.00	9.23666e-01	8.91007e-01	9.25684e-01	8.91007e-01
126.00	8.25640e-01	8.09017e-01	8.27955e-01	8.09017e-01
135.00	7.07113e-01	7.07107e-01	7.08791e-01	7.07107e-01
144.00	5.70577e-01	5.87785e-01	5.72823e-01	5.87785e-01
153.00	4.21961e-01	4.53991e-01	4.25553e-01	4.53991e-01
162.00	2.68411e-01	3.09017e-01	2.70131e-01	3.09017e-01
163.80	2.37157e-01	2.78991e-01	2.38872e-01	2.78991e-01
165.60	2.06831e-01	2.48690e-01	2.08493e-01	2.48690e-01
167.40	1.75739e-01	2.18143e-01	1.77573e-01	2.18143e-01
169.20	1.44008e-01	1.87381e-01	1.45689e-01	1.87381e-01
171.00	9.06270e-03	1.56434e-01	1.06531e-02	1.56434e-01
172.80	3.56930e-05	1.25333e-01	1.76429e-03	1.25333e-01
174.60	3.06500e-05	9.41083e-02	1.87239e-03	9.41083e-02
180.00	0.00000e+00	0.00000e+00	0.00000e+00	0.00000e+00